ORTA DOĞU TEKNİK ÜNİVERSİTESİ
FEN BİLİMLERİ ENSTİTÜSÜ MÜDÜRLÜĞÜ

TEZ ŞABLONU ONAY FORMU
THESIS TEMPLATE CONFIRMATION FORM

1. Şablonda verilen yerleşim ve boşluklar değiştirilmemelidir.
2. **Jüri tarihi** Başlık Sayfası, İmza Sayfası, Abstract ve Öz'de ilgili yerlere yazılmalıdır.
3. İmza sayfasında jüri üyelerinin unvanları doğru olarak yazılmalıdır. Tüm imzalar **mavi pilot kalemle** atılmalıdır.
4. **Disiplinlerarası** programlarda görevlendirilen öğretim üyeleri için jüri üyeleri kısmında tam zamanlı olarak çalıştıkları anabilim dalı başkanlığının ismi yazılmalıdır. Örneğin: bir öğretim üyesi Biyoteknoloji programında görev yapıyor ve biyoloji bölümünde tam zamanlı çalışıyorsa, İmza sayfasına biyoloji bölümü yazılmalıdır. İstisnai olarak, disiplinler arası program başkanı ve tez danışmanı için disiplinlerarası program adı yazılmalıdır.
5. Tezin **son sayfasının sayfa** numarası Abstract ve Öz'de ilgili yerlere yazılmalıdır.
6. Bütün chapterlar, referanslar, ekler ve CV sağ sayfada başlamalıdır. Bunun için **kesmeler** kullanılmıştır. **Kesmelerin kayması** fazladan boş sayfaların oluşmasına sebep olabilir. Bu gibi durumlarda paragraf (¶) işaretine tıklayarak kesmeleri görünür hale getirin ve yerlerini **kontrol edin**.
7. Figürler ve tablolar kenar boşluklarına taşmamalıdır.
8. Şablonda yorum olarak eklenen uyarılar dikkatle okunmalı ve uygulanmalıdır.
9. Tez yazdırılmadan önce PDF olarak kaydedilmelidir. Şablonda yorum olarak eklenen uyarılar PDF dokümanında yer almamalıdır.
10. **Bu form aracılığıyla oluşturulan PDF dosyası arkalı-önlü baskı alınarak tek bir spiralli cilt haline getirilmelidir.**
11. Spiralli hale getirilen tez taslağınızdaki ilgili alanları imzalandıktan sonra, Tez Juri Atama Formu ile birlikte bölüm sekreterliğine teslim edilmelidir.
12. Tez taslaklarının kontrol işlemleri tamamlandığında, bu durum öğrencilere METU uzantılı öğrenci e-posta adresleri aracılığıyla duyurulacaktır.
13. Tez yazım süreci ile ilgili herhangi bir sıkıntı yaşarsanız, **Sıkça Sorulan Sorular (SSS)** sayfamızı ziyaret ederek yaşadığınız sıkıntıyla ilgili bir çözüm bulabilirsiniz.

1. Do not change the spacing and placement in the template.
2. Write **defense date** to the related places given on Title page, Approval page, Abstract and Öz.
3. Write the titles of the examining committee members correctly on Approval Page. **Blue ink** must be used for all signatures.
4. For faculty members working in **interdisciplinary programs**, the name of the department that they work full-time should be written on the Approval page. For example, if a faculty member staffs in the biotechnology program and works full-time in the biology department, the department of biology should be written on the approval page. Exceptionally, for the interdisciplinary program chair and your thesis supervisor, the interdisciplinary program name should be written.
5. Write **the page number of the last page** in the related places given on Abstract and Öz pages.
6. All chapters, references, appendices and CV must be started on the right page. **Section Breaks** were used for this. **Change in the placement** of section breaks can result in extra blank pages. In such cases, make the section breaks visible by clicking paragraph (¶) mark and **check their position.**
7. All figures and tables must be given inside the page. Nothing must appear in the margins.
8. All the warnings given on the comments section through the thesis template must be read and applied.
9. Save your thesis as pdf and Disable all the comments before taking the printout.
10. **Print two-sided the PDF file that you have created through this form and make a single spiral bound.**
11. Once you have signed the relevant fields in your thesis draft that you spiraled, submit it to the department secretary together with your Thesis Jury Assignment Form.
12. This will be announced to the students via their METU students e-mail addresses when the control of the thesis drafts has been completed.
13. If you have any problems with the thesis writing process, you may visit our **Frequently Asked Questions (FAQ)** page and find a solution to your problem.

☒ **Yukarıda bulunan tüm maddeleri okudum, anladım ve kabul ediyorum. / I have read, understand and accept all of the items above.**

Name : **Ali Emre**
Surname : **Tanrısevdi**
E-Mail : **emre.tanrisevdi@metu.edu.tr**
Date :
Signature : _____

EFFECT OF HEAT TREATMENT PARAMETERS ON THE Q-FACTOR OF FE-NI SUPERALLOYS

A THESIS SUBMITTED TO
THE GRADUATE SCHOOL OF NATURAL AND APPLIED SCIENCES
OF
MIDDLE EAST TECHNICAL UNIVERSITY

BY

ALI EMRE TANRISEVDI

IN PARTIAL FULFILLMENT OF THE REQUIREMENTS
FOR
THE DEGREE OF MASTER OF SCIENCE
IN
METALLURGICAL AND MATERIALS ENGINEERING

FEBRUARY 2022

Approval of the thesis:

EFFECT OF HEAT TREATMENT PARAMETERS ON THE Q-FACTOR OF FE-NI SUPERALLOYS

submitted by **ALİ EMRE TANRISEVDİ** in partial fulfillment of the requirements for the degree of **Master of Science** i**n Metallurgical and Materials Engineering, Middle East Technical University** by,

Prof. Dr. Halil Kalıpçılar
Dean, Graduate School of **Natural and Applied Sciences** _____

Prof. Dr. C. Hakan Gür
Head of the Department, **Metallurgical and Materials Eng.** _____

Prof. Dr. Rıza Gürbüz
Supervisor, **Metallurgical and Materials Eng, METU** _____

Examining Committee Members:

Prof. Dr. Bilgehan Ögel
Metallurgical and Materials Eng, METU _____

Prof. Dr. Rıza Gürbüz
Metallurgical and Materials Eng, METU _____

Prof. Dr. Amdulla Mekhrabov
Metallurgical and Materials Eng, METU _____

Prof. Dr. Abbas Tamer Özdemir
Metallurgical and Materials Eng, Gazi University _____

Assoc. Prof. Caner Şimşir
Metallurgical and Materials Eng, METU _____

Date: 03.02.2022

I hereby declare that all information in this document has been obtained and presented in accordance with academic rules and ethical conduct. I also declare that, as required by these rules and conduct, I have fully cited and referenced all material and results that are not original to this work.

Name Last name: Ali Emre Tanrısevdi

Signature:

ABSTRACT

EFFECT OF HEAT TREATMENT PARAMETERS ON THE Q-FACTOR OF FE-NI SUPERALLOYS

Tanrısevdi, Ali Emre
Master of Science, Metallurgical and Materials Engineering
Supervisor: Prof. Dr. Rıza Gürbüz

February 2022, 117 pages

Q-factor or quality factor is a dimensionless parameter that indicates loses of energy in a mechanical structure. It is a phenomenon commonly used in coils, condensers, resonant circuits, resonant devices, transmission lines and gyroscopes. High Q-factor materials are used in space, defence and aviation industry. Low energy loss during oscillation of material connotes high Q-factor. Utilization of high Q-factor materials in commercial applications necessitate easily accessible metallic materials to be used rather than quartz because of economic reasons. In this study, Ni-Span C902, 42NiCrTiAl, 42NiCrTiAl, 36NiCrTiAl superalloys are studies in order to understand the effect of heat treatment process to their Q-factor values and the relationship between Q-factor and materials' properties. It is been seen that Q-factor of superalloys depend on not only mechanical properties but also microstructure. Grain size, annealing twins, grain boundary geometry and precipitates were observed to change the Q-factor of superalloys.

Keywords: Quality Factor, Iron-Nickel Steels, Superalloys, Gyroscopes, Heat Treatment, Microstructure

ÖZ

FE-NI SÜPERALAŞIMLARINDA ISIL İŞLEM PARAMETRELERİNİN KALİTE FAKTÖRÜNE ETKİSİ

Tanrısevdi, Ali Emre
Yüksek Lisans, Metalurji ve Malzeme Mühendisliği
Tez Yöneticisi: Prof. Dr. Rıza Gürbüz

Şubat 2022, 117 sayfa

Q-faktörü veya kalite faktörü, mekanik bir yapıdaki enerji kayıplarını gösteren boyutsuz bir parametredir. Bobinlerde, kondansatörlerde, rezonans devrelerinde, rezonans cihazlarında, enerji aktarım hatlarında ve jiroskoplarda yaygın olarak kullanılan bir fenomendir. Yüksek Q-faktörlü malzemeler, uzay,savunma ve hacılık endüstrilerinde kullanılmaktadır. Malzemenin salınımı sırasında düşük enerji kaybı, yüksek Q-faktörünü ifade eder. Yüksek Q-faktörlü malzemelerin ticari uygulamalarda kullanılması, ekonomik nedenlerden dolayı kuvars yerine kolay erişilebilir metalik malzemelerin kullanılmasını zorunlu kılmaktadır. Bu çalışmanın amacı, Ni-Span C902, 42NiCrTiAl, 42NiCrTiAl, 36NiCrTiAl süperalaşımlarında ısıl işlemin Q-faktör değerlerine etkisini ve Q-faktörü ile malzeme özellikleri arasındaki ilişkiyi anlamatır. Süperalaşımların Q-faktörü, sadece mekanik özelliklere değil aynı zamanda mikroyapıya da bağlı olduğu görülmüştür. Tane boyutu, tavlama ikizleri, tane sınırı geometrisi ve çökeltilerin süperalaşımların Q faktörünü değiştirdiği gözlemlenmiştir.

Anahtar Kelimeler: Kalite Faktörü, Demir-Nikel Çelikler, Süperalaşımlar, Jiroskoplar, Isıl İşlem, Mikroyapı

To My Family & Friends

ACKNOWLEDGMENTS

I wish to express my thanks to my advisor Prof. Dr. Rıza Gürbüz for his guidance and support during tough times of COVID-19 pandemic.

I am so grateful for my brother Berk Tanrısevdi, without his endless support and wisdom throughout the whole time on this study. There are touches of him all over this thesis study.

My special thanks to Aslıhan Yurdakul for believing in me all the time, encouraging me and finding me this thesis topic in the first place.

I wish to express my sincere thanks to Caner Gençoğlu for his great support, patience and always having creative solutions.

My friends Orkun, Cihan, Erdi, Eren are always appreciated for their support and believe in me.

Finally, I cannot thank enough to my family and wife for their understanding, help and empathy

TABLE OF CONTENTS

LIST OF TABLES

LIST OF FIGURES

LIST OF ABBREVIATIONS

CVG	Coriolis Vibratory Gyroscope
SDOF	Single Degree of Freedom
MDOF	Multiple Degree of Freedom
FRF	Frequency Response Function
MTR	Modal Test Robot
COV	Coefficient of Variances
ASTM	American Society for Testing and Materials
VIM	Vacuum Induction Melting
VAR	Vacuum Arc Remelting
ESR	Electroslag Remelting
HV10	Vickers Hardness with Test Load of 10 kgf
FCC	Face Centered Cubic
BCC	Body Centered Cubic
BCT	Body Centered Tetragonal
GCP	Geometrically Closed Packed
HCP	Hexagonal Closed Packed

CHAPTER 1

INTRODUCTION

Steels are widely used in all kinds of sectors since 2000 BC. Since then, steel industry is in constant grow. Different steel grades have been developed for aerospace, automobile and construction applications to be used in dynamic and static loading conditions. The competitiveness of those sectors increased the research and development of new processes, compositions and heat treatment operations in order to obtain superior mechanical properties and low cost. This is the reason why steel-based studies take over majority of metallurgy community. Thanks to this competitiveness, steels are used in numerous applications with required mechanical properties and manufacturing processes.

During the war, development of steels having alloying elements increased, especially the ones containing nickel and chromium. These alloying elements were commonly used and very important in the production of internal-combustion engines where operation conditions are very rigorous [1]. Different alloying elements, their compositions and heat treatments trigger different strengthening mechanisms. The kind of strengthening mechanism decides the operating/service conditions of alloys.

Superalloys are better known for their high mechanical properties at high temperature and remain under-researched for their mechanical vibration damping capacity [2]. Superalloys are complex alloys of Fe-Ni, Ni-, and Co-base compositions. Their microstructural analysis is also very complex due to diversification of phases that can arise in heat treatment or service exposure [3]. Fe-Ni steels are called superalloys and are generally used in materials where thermoelastic coefficient characteristics control and high temperature resistance are

essential. These types of alloys are good for precise springs in watches, weighing instruments. High oxidation resistance and constant modulus of elasticity is other important properties of Fe-Ni alloys. Commonly obtained strengthening mechanisms for Fe-Ni superalloys are grain boundary strengthening, deformation hardening and precipitation hardening.

Figure 1. Sample Hemispherical Resonator Gyroscope That Measures Motion by The Change In Vibration Of A Cup-Shaped Device. [4]

1.1 Motivation

Gyroscopes are used in various purposes like navigational, tactical, industrial and strategical and their sensitivity changes with its usage field. In the case of Coriolis gyroscopes, there is vibrating beam whose vibration results in Coriolis force (will be discussed in literature review section). The material of this vibrating beam is essential since the properties of it, which will be called sensitive part of gyroscope later, determine the sensitivity of gyroscope. Mechanical properties of sensitive part changes with composition and heat treatment.

Main motivation of this study is to understand the relationship between mechanical properties and Q-factor of sensitive part

1.2 Aim of the Work and Main Contribution

The aim of this research was to investigate the relation between Q-factor and mechanical properties of various Fe-Ni superalloys having different compositions and different strengthening mechanisms through different heat treatment operations. In this regard, to be used in gyroscopes, different heat treatment processes carried out in order to obtain the maximal value of Q-factor. Definition of Q-factor was discussed at the literature review section. Figure 2 shows sample design geometries of coriolis vibratory gyroscope

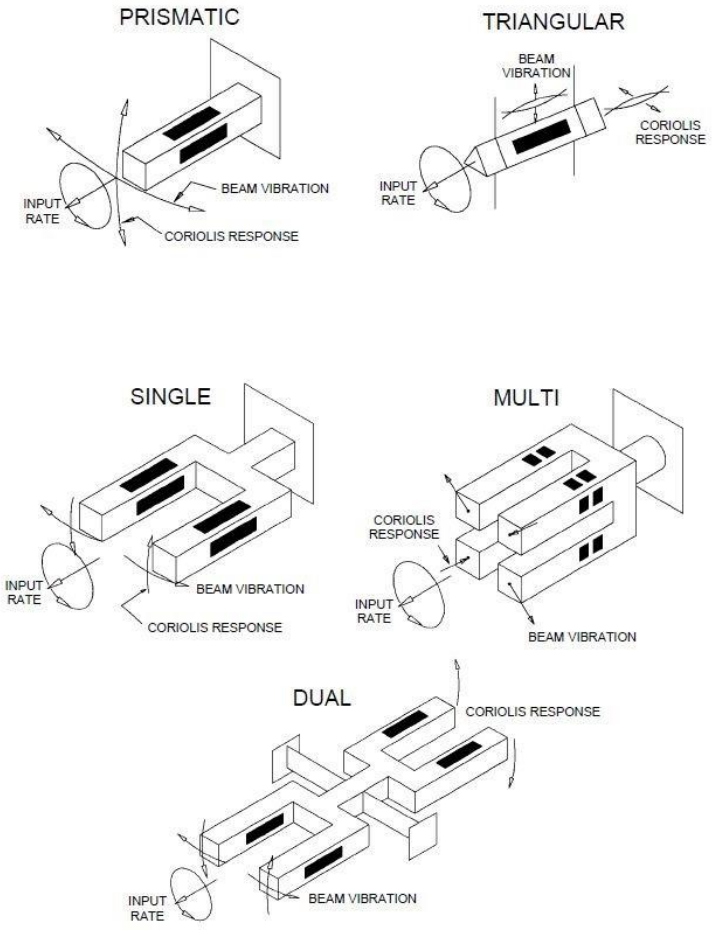

Figure 2. Sample Design Geometries of Coriolis Vibratory Gyroscopes [5]

Sensitive part of the gyroscopes is the basic part of the sensor exposed to primary and secondary movements. Material characteristics, design and production directly affect the sensitivity of the sensor. Quartz is generally used for gyroscope sensitive parts because of its very low damping capacity meaning high quality factor [6]. However, the cost of quartz materials is much higher than metals. By this study, approaching the Q-factor value as close as possible with relatively lower cost metallic materials was tried to be achieved by optimizing the heat treatment parameters. This thesis study served the design of sensitive part of the Coriolis Vibratory Gyroscope (CVG).

CHAPTER 2

LITERATURE REVIEW

2.1 Coriolis Effect

The "Coriolis" effect is an inertial force described by Gustace-Gaspard Coriolis. When a movement is made in a radial direction in a rotating system, a "Coriolis" force perpendicular to the direction of movement occurs on the object. Figure 3 shows that the object moving from x0 position to x1 position in a system rotating with "angular velocity" comes to the point x1 "due to the" Coriolis force". Coriolis force is determined according to the following equation. Equation 1 shows the relation of "Coriolis" force with angular motion.

Equation 1: $\vec{F}_C = -2 \cdot m \cdot \vec{\omega} \times \vec{v}$

$\vec{v}$: x0 − x1 $motion\ vector$

$\vec{\omega}$: $angular\ velocity$

m: $mass$

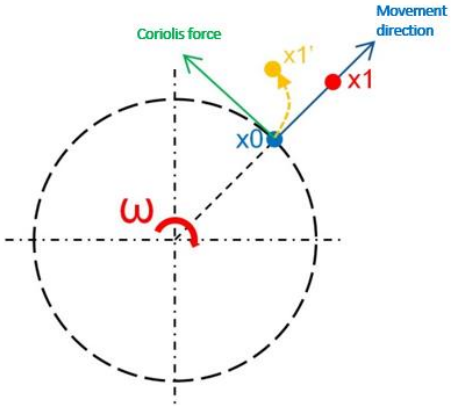

Figure 3. Coriolis Force

2.2 Coriolis Vibratory Gyroscopes (CVG)

Gyroscopes are inertial equipments to measure angular velocity. It is inferred from [7] that the Foucault Pendulum is the first ever built vibrating gyroscope (Figure 4) named for the French physicist Jean Foucalt who first used it in 1851 to show the rotation of earth. If a Foucault Pendulum is swinging in one direction, after several hours one will discern that pendulum is swinging in divergent direction because of the rotation of the earth

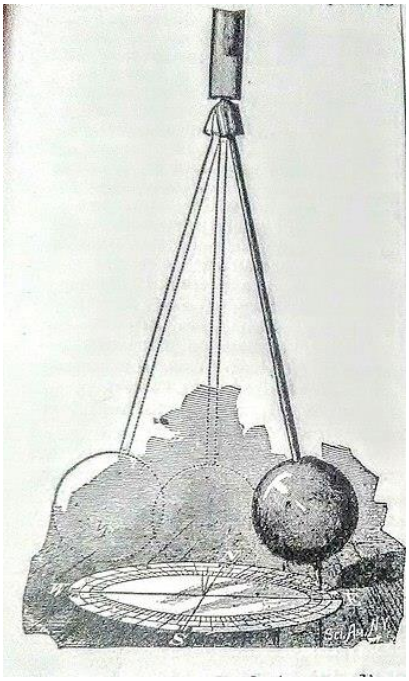

Figure 4. A Print of the Foucault Pendulum, 1895 [8]

The work presented in this thesis is motivated by the neccesity of better understanding of vibrating microstrutures and their internal friction mechanisms in sensitive part of CVG. This is the reason that this thesis is built around working principle of CVG.

The motion component created by the "Coriolis" force perpendicular to the direction of motion changes depending on the amount of rotation. Sensors that use this effect for rotation measurement are called "Coriolis" gyroscopes. "Coriolis" gyroscopes are modeled as a mass-spring system (Figure 5). For the sake of

explanation, this mass will be named as sensitive part. The primary motion shown in Figure 5 is the movement given to the system from the outside, and the secondary motion is the movement created by the system with the effect of coriolis. [9]

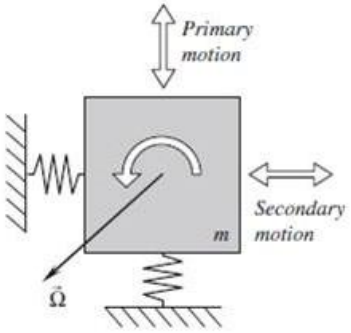

Figure 5. Principle of CVG operation [9]

As it can be understood from Figure 5, given to explain the Coriolis force, the sensitive part of the gyroscope "Coriolis" makes a two-dimensional pendulum movement, and this movement has an elliptical orbit around the center of gravity. In Figure 6, a and b show the long and short axes of the ellipse. θ is the elliptical rotation angle due to the first x_1 and the second x_2 motion.

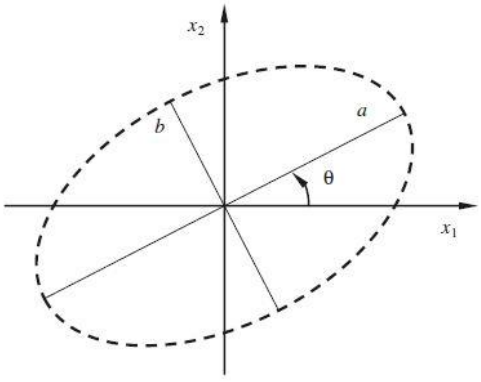

Figure 6. Sensitive Part Motion Trajectory

2.3 Coriolis Vibratory Gyroscopes' Parts

The parts of the "Coriolis" gyroscope vary according to the different designs of the companies. Basic sections are sensitive part, actuator (piezoelements and driver card) and an outer box. The sensitive part is the basic section that undergoes primary motion and creates secondary motion. Details regarding this design will be given in the next sections. The actuator parts are used to give the primary movement to the system. The outer box protects the system against environmental influences and at the same time increases the total quality factor of the system by providing a vacuum environment. The concept of quality factor has been defined in section 2.4.

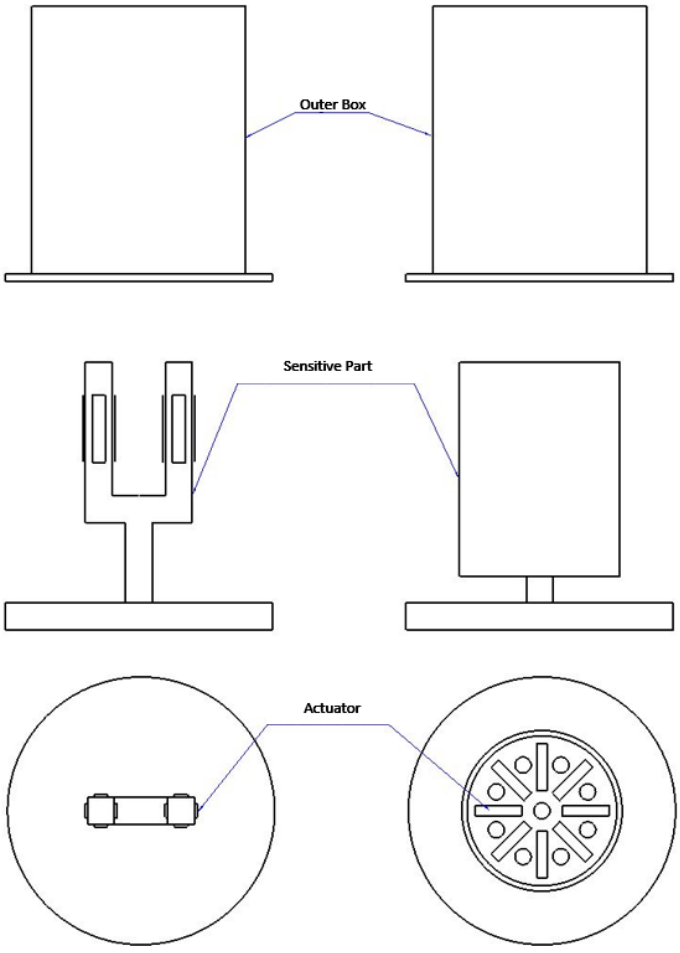

Figure 7. Parts of CVG

2.4 Definition of Q-Factor

Q-factor or quality factor is a dimensionless parameter that indicates loss of energy in a mechanical structure. It is a phenomenon commonly used in coils, condensers, resonant circuits, resonant devices, transmission lines and gyroscopes. High quality factor materials like quartz are used in space vehicles as HRG "Hemispherical Resonant Gyroscopes". Low energy loss during oscillation of material connotes high Q-factor. In addition, according to Lifshitz and Roukes [10]"The dissipation, or "internal friction," in the solid Q^{-1} is defined as the fraction of energy lost per radian of vibration". As it is mentioned in above explanations, Q-factor has different definition according to place of use. Simply, it is the loss of energy in the mechanical structure thought out object due to internal friction.

2.5 Parameters Affecting Q-Factor

As it can be seen in Figure 8, Q-factor is affected by material, geometry, surrounding atmosphere, and unbalance (defects, unwanted forces and torques at the vibration frequency).

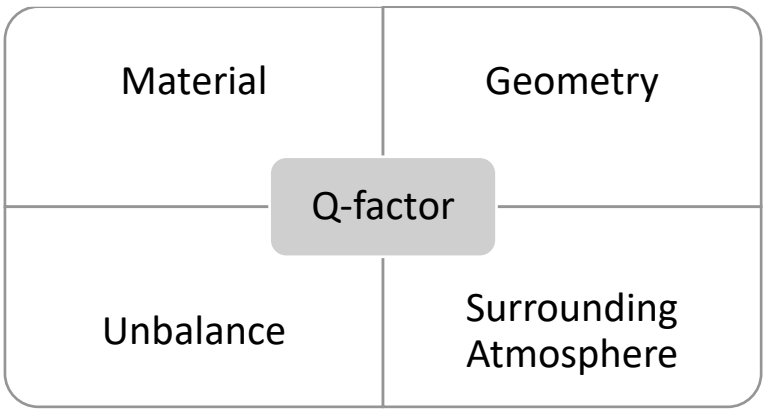

Figure 8. Parameters Affecting Q-factor

In this thesis, effect of material's inner properties to Q-factor is researched. In material's inner properties point of view, dislocation density and mean length of dislocations between the weak pinning points affect the Q-factor. These weak

pinning points consist of soluble atoms or vacancies surrounding dislocations. Dislocation movements are the major internal friction mechanism [11].

According to Hu et al. [11]:

Equation 2: $\boldsymbol{Q^{-1} \sim \rho l^4}$

ρ: dislocation density
l: mean length of dislocation

It can be inferred from above formula and as mentioned (Watanabe, Mukai, Sugioka and Ishikawa, 2004) "The elastic and damping properties depends on the microstructural factors such as specimen orientation (texture) and grain size." [12]

2.6 Modal Testing and Structural Dynamics

Calculation and better understanding of Q-factor needs fundamental knowledge of structural dynamics and modal testing. Basic understanding of structural dynamics is also necessary in order to get agile modal testing. Structural dynamics present critical design limitation for engineering materials and applications. Dynamic means time varying. [13] The responses of structures underloading is also time dependent or dynamic. According to Tedesco et al. [14], "In reality, no loads that are applied to a structure are truly static. Since all loads must be applied to a structure in some particular sequence, a time variation of the force is inherently involved. However, whether or not a load should be considered dynamic is a relative matter. The most significant parameter influencing the extent of the dynamic effect a load has upon a structure is the *natural period of vibration* of the structure." According to Ewins [15], there are two major vibration measurement objectives. Firstly, there are number of structures, from censors to bridges, where structural integrity and precise knowledge of dynamic characteristics is important. Secondly, there are structural applications where vibration is directly related to performance. These two major objectives mean two corresponding test types. The

first one is where vibration forces are measured during operation of structure, while the second is a test where the structure is vibrated with known excitation. This second type of test yields more accurate data under dynamics loading due to more strictly controlled test environment which gives critical information of material properties such as Q-factor, damping capacity, internal friction and fatigue. The type of testing is called ‘Modal Testing’. “Although the name is relatively new, the principles of modal testing were laid down many years ago. These have evolved through various phases when descriptions such as 'Resonance Testing' and 'Mechanical Impedance Methods' were used” [15].

When the relationship between structural dynamics and modal testing is established, it is time to comprehend the relationship between frequency response function and its modal parameters. Knowing this relationship and its variations will lead to successful measurements. Below Figure 9 illustrates the phases of modal test.

Modal test can be carried out using ASTM E1876 [16] and ASTM E756 [17]. ASTM E1876 is standard test method for measuring vibration-damping properties of materials and measures the vibration-damping porperties of materials: loss factor and Yung’s modulus or shear modulus. ASTM E756 is standard test method for dynamic Young’s modulus, shear modulus and Poisson’s ratio by impulse excitation of vibration and covers determination of the dynamic elastic properties of elastic materials at ambient temperetures. These standards help to compute damping factor, loss factor or quality factor by converting results using logarithmic decrement, step-response, hysterises loop, magnification factor or hal-power bathwidth method for isotropic materials. In this study, patented [18] modal test robot (MTR) was used. The touching points and types of impulser and transducers are different compared to MTR. MTR is designed for complex parts as it is explained in section 3.4 Q-Factor Tests.

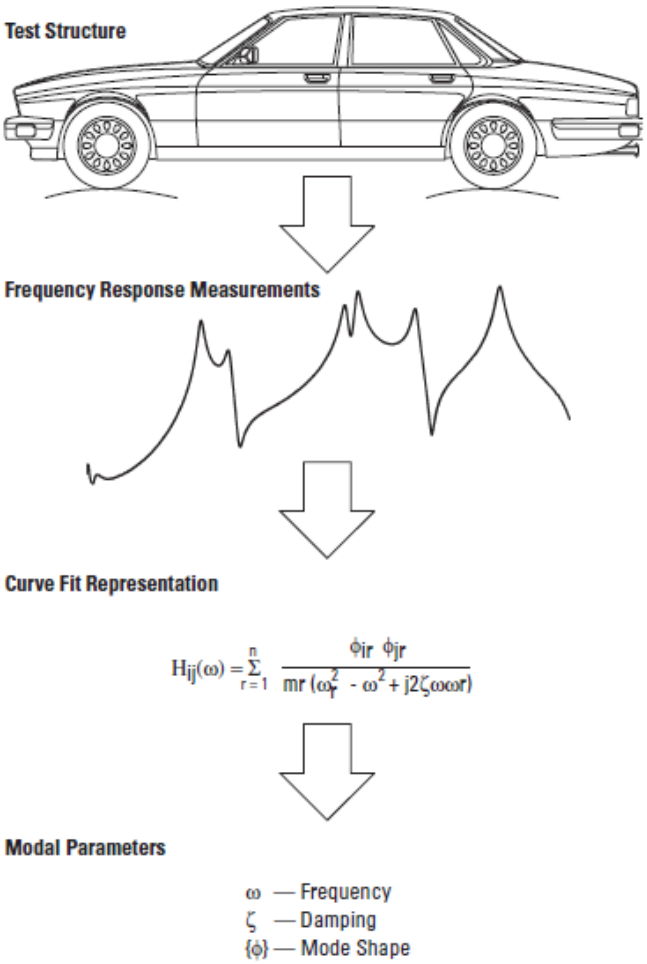

Figure 9. Phases of Modal Test [16]

Since the objective of this thesis study is to understand the effect of heat treatment parameters on the Q-factor and Q-factor is measured by a Modal Test Robot (MTR), only basic equations and their various adjectives will be presented to give perception on the relationship between the dynamic characteristics of the structures and its frequency response function measurements. Detailed results and raw data will be given in the section 4 RESULTS.

Practical systems or basically in real life applications multiple degree of freedom (MDOF) systems with nonlinearity are encountered. Their calculation, measurement and estimation methods are quite complex; therefore, they are generally superpositioned into single degree of freedom (SDOF) models.

In this part of section 2.6 Modal Testing and Structural Dynamics, three main concepts will be reviewed.

1. Basics of SDOF linear dynamic systems
2. Basics of frequency response function measurements
3. Extension into MDOF systems

2.6.1 Basics of a Single Degree of Freedom (SDOF) Systems

Most of the systems are continuous and nonlinear but their behavior can be represented by a separate parameter system as shown in Figure 10. According to Nasif et al. [20], this system is made for its physical and mathematical simplicity which eliminates any of the apparent paradoxes or mathematical difficulties. However, this idealized model happens on rare occasions in the real-life applications.

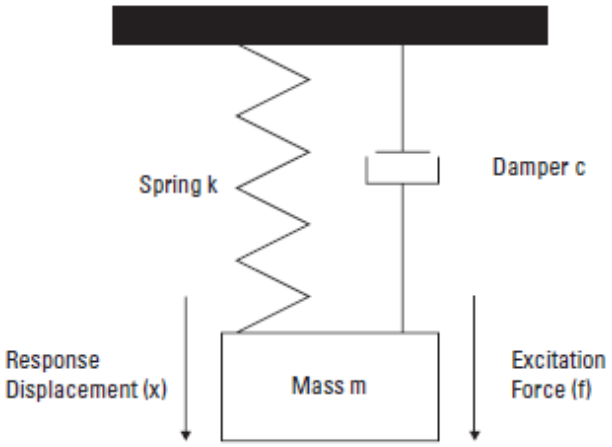

Figure 10. SDOF Model [16]

Below motion equations describe the physical system and explain the relationship between mass (m), stiffness (k) and damping (c). This relationship shows the way to the calculation of natural frequency (ω_n) and damping factor (ζ).

Equation 3: $m\ddot{x} + c\dot{x} + kx = F(t)$

Equation 4: $\omega_n = \sqrt{\frac{k}{m}}$

Equation 5: $\zeta = \frac{c}{\sqrt{2km}}$

The undamped natural frequency ω_n is radians per second (rad/s). However, most of the digital signal receivers display in Hertz (Hz). "Damping factor may be represented by various parameters such as Q-factor, specific damping capacity, loss factor and damping ratio)" [18]. According to Harris and Piersol [19], the value of damping factor is represented as percent of critical damping shown in Equation 6.

Equation 6: $\zeta = \frac{c}{C_c}$

When $c = c_c$, there is no oscillation, and this point is called critical damping. If the damping is less than critical, $\zeta < 1$. Although there are three damping ratio probabilities ($\zeta < 1$, $\zeta = 1$, $\zeta < 1$), only the underdamped ($\zeta < 1$) case is essential for structural systems. In this thesis study, 4 different types of structural superalloys are used. Therefore, from this point on literature will be investigated for underdamping mechanisms. When $\zeta < 1$, the Q-factor can be approximated as [20];

Equation 7: $Q \simeq \frac{1}{2\zeta}$

According to [16], when there is no excitation, the root of the equation has real and imaginary parts. Real part defines damping in the system and imaginary part defines damped natural frequency, ω_d. This response of vibration is shown in Figure 11.

Equation 8: $S_{1,2} = -\sigma + j\omega_d$

σ: $Damping\ rate$

ω_d: $Damped\ Natural\ Frequency$

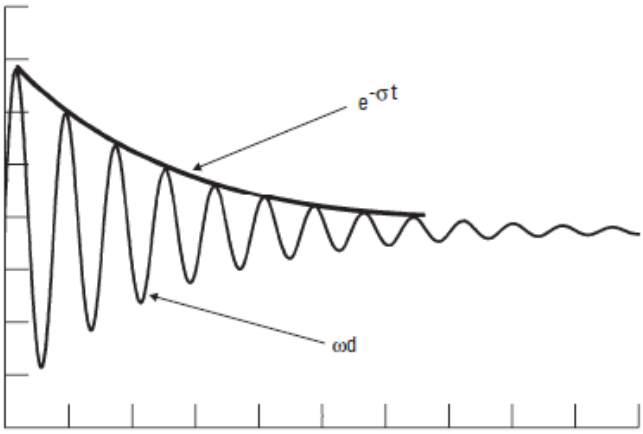

Figure 11. SDOF Free Vibration Response [19]

When an excitation or a force applied to the system, Equation 3, Equation 4 and Equation 5 result in the frequency response of the system. This response is in the form of Equation 8 meaning, it is complex and has real and imaginary parts [24].

2.6.2 Basics of Frequency Response Functions

According to [25] and [26], "frequency response function (FRF) is a transfer function which is defined as the dynamic response of a structure from its one point & direction to another point & direction in the frequency domain. FRF is defined between DOFs which means points and directions. By FRF, MDOF dynamic response of the structure is defined. The participation of each mode into the FRF depends on the input and output DOFs." Due to these reasons, FRF is useful tool in the dynamic analysis of vibratory systems.

Frequency response is complex and has real and imaginary parts. Therefore, its schematic view cannot be fully shown in single two-dimensional plot. However, there are several ways to present frequency responses. Each way displays different phenomenon. As it is shown in Figure 10. SDOF Model, displacement is not the

only response; it can also be velocity and acceleration. In this thesis study, acceleration is used for the method of measuring modal test results.

One method of displaying the data is to plot polar coordinates. In Figure 12, magnitude and phase versus frequency (ω) plots are presented. At the resonance point, where $\omega = \omega_n$, the magnitude is in its peak and only limited by the damping capacity of the system. The phase axis ranges from 0°-180° and its response delays 90° at resonance, where $\omega = \omega_n$.

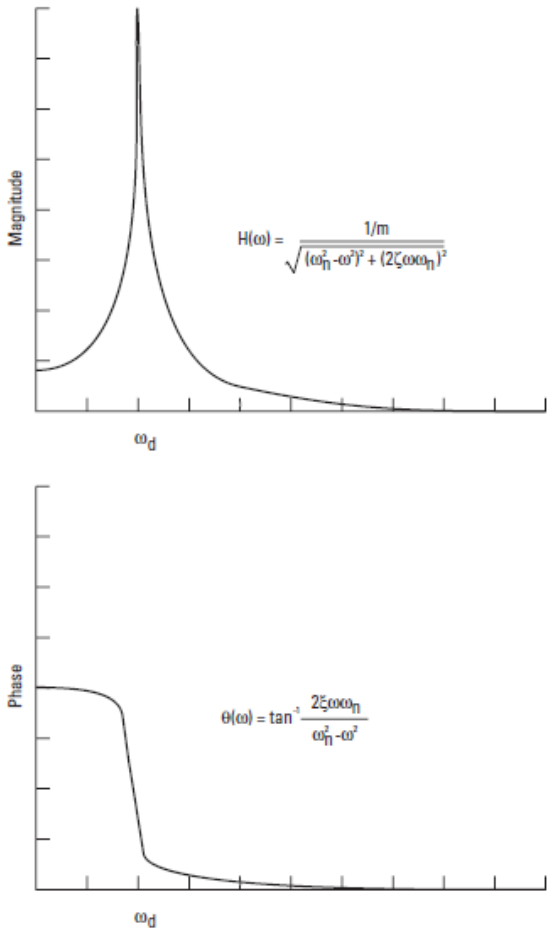

Figure 12. Frequency Response in Polar Coordinates [19]

Another way of displaying data is to plot complex coordinates, the real part and the imaginary part versus frequency. For a damped system, imaginary part is at its peak and real part is zero at resonance as shown in Figure 13.

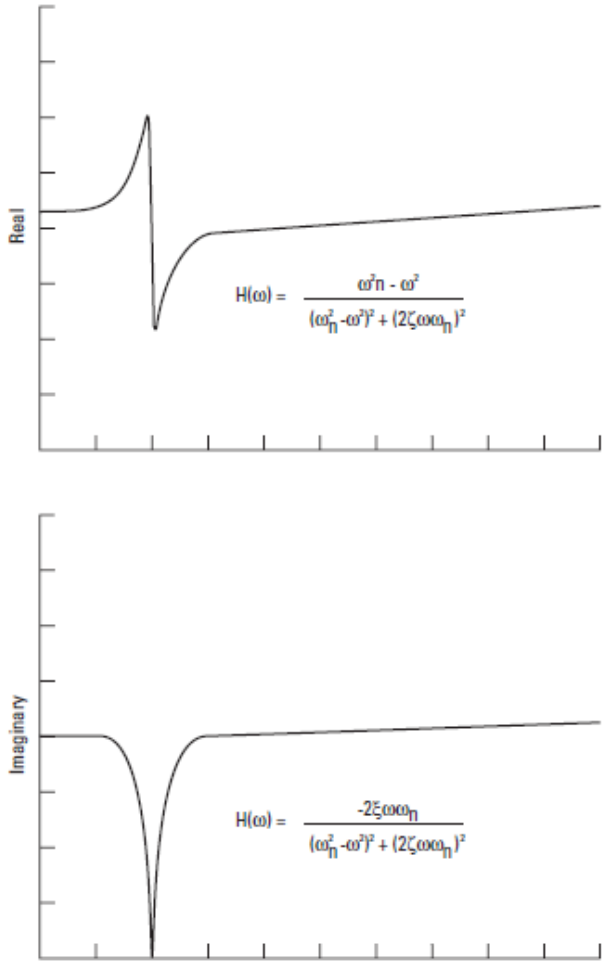

Figure 13. Frequency Response in Complex Coordinates [19]

Third way of displaying frequency response is to plot the imaginary part versus the real part. It is called a Nyquist plot shown in Figure 14. This plot emphasizes the area of frequency response at resonance.

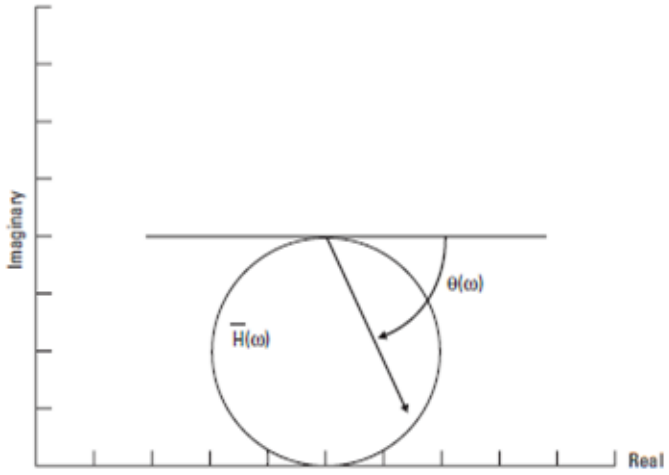

Figure 14. Frequency Response in Nyquist Plot [19]

By plotting the magnitude in decibels (dB) vs log of frequency, it is possible to cover wider ranges of frequency and amplitude. In Figure 15 , various useful plots are also displayed.

When $\omega \ll \omega_n$, the frequency response is almost equal to asymptote and this asymptote line has a slope of 0 for displacement, 1 for velocity and 2 for acceleration. This line is called the stiffness line. When $\omega \gg \omega_n$, the frequency response is almost equal to asymptote and this asymptote line has a slope of -2 for displacement, -1 for velocity and 0 for acceleration. This line is called the mass line.

In Table 1 , analogy between frequency response function based on type of response variable is represented and “depending on whether the response motion is measured as displacement, velocity, or acceleration, the FRF and its inverse can have a variety of names” [25]

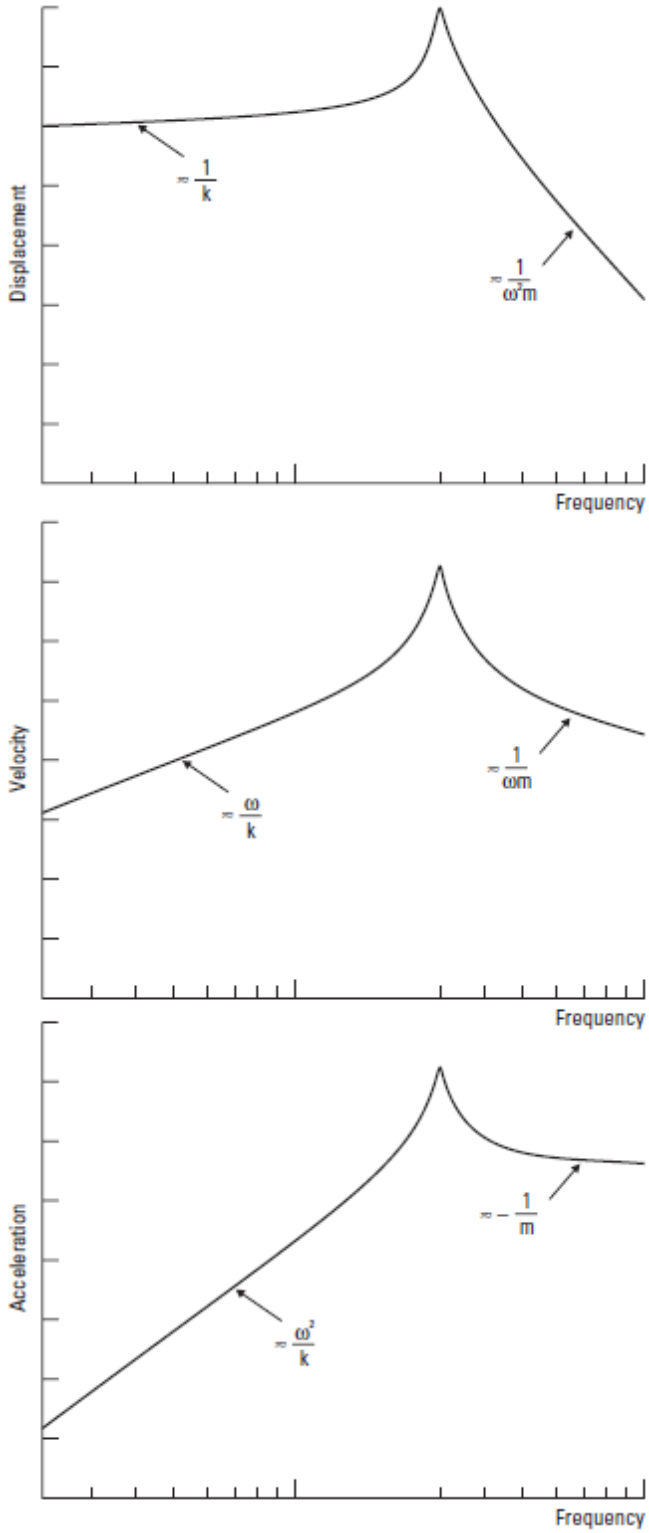

Figure 15. Different Forms of Frequency Response [19]

Table 1. Different Forms of Frequency Response [19] [25]

Definition	**Variable**
Compliance	$\frac{\text{Displacement}}{Force}$
Mobility	$\frac{\text{Velocity}}{Force}$
Accelerance (Inertance)	$\frac{\text{Acceleration}}{Force}$
Dynamic Stiffness	$\frac{1}{Complience}$
Impedance	$\frac{1}{Mobility}$
Dynamic Mass	$\frac{1}{Accelerance}$

There is a FRF graph that is used in this thesis study in Figure 16, first part of FRF graph is the plot of amplitude versus frequency. Sharp peaks display resonant frequencies. If the damping is low, the resonant peaks of FRF graph will be higher and narrower. The second part of graph is the plot of phase-lag versus frequency. Phase-lag will be 90 degrees at the natural frequencies.

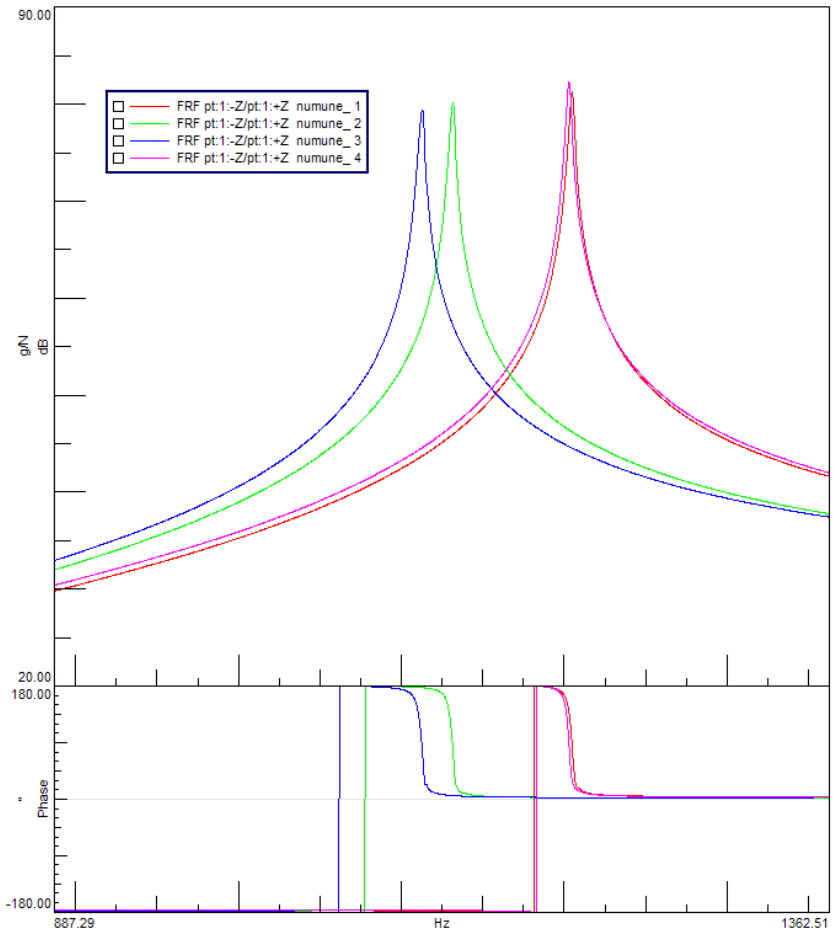

Figure 16. An Example of The Frequency Response Function (FRF) Of 4 Different Superalloys

2.6.3 Extension to MDOF Systems

The extension of single degree of freedom systems (SDOF) to real-life systems meaning multiple degree of freedom systems (MDOF) with *n* degrees of freedom is an explicit approach. Every MDOF systems are interconnected with idealized SDOF models similar to physical systems as illustrated in Figure 17.

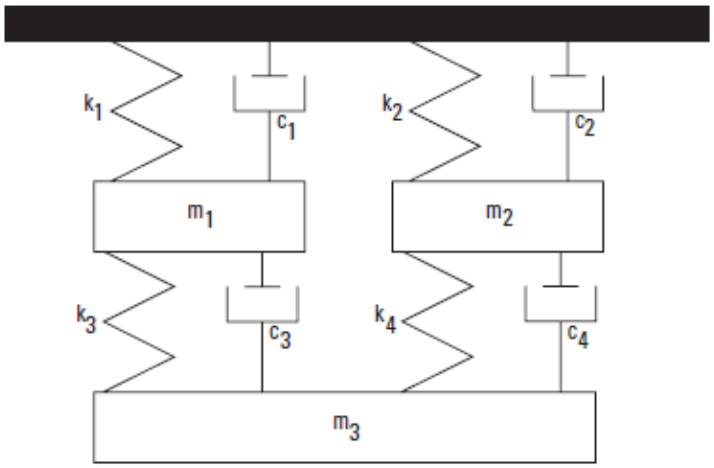

Figure 17. Example of MDOF System [19]

For MDOF, every distinct frequency and damping has different displacement and free vibration response, shown in Figure 18. In order to understand the difference between SDOF and MDOF free vibration response, one can compare the Figure 11 and Figure 18.

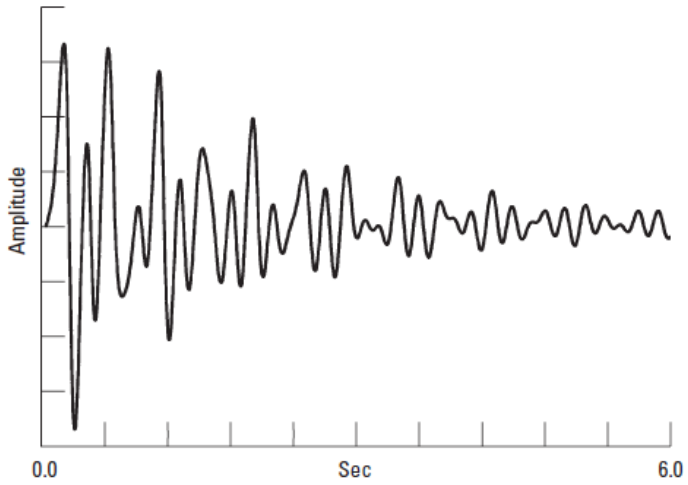

Figure 18. MDOF Free Vibration Response [19]

The equations of motion lead to frequency response of the system and these responses are calculated by weighted summation of SDOF systems. Weighted

summation is called modal participation factor in modal analysis. Excitation and shape coefficients are functions of this summation.

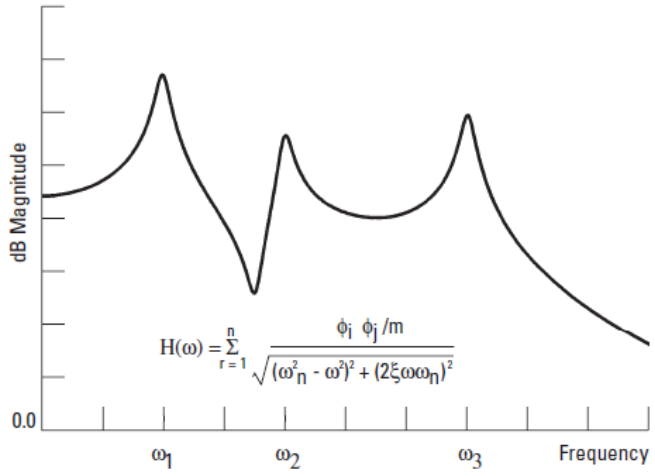

Figure 19. Example of MDOF Frequency Response [19]

The weighted summation or participation factor helps to calculate the amount of each mode contribution to the total frequency response. Figure 19 shows an example of MDOF frequency response and Figure 20 shows the contribution of each mode into this example of MDOF frequency response. In this example, there are 3 degrees of freedom as illustrated in Figure 20. The frequency response of an MDOF system can be divided into SDOF case.

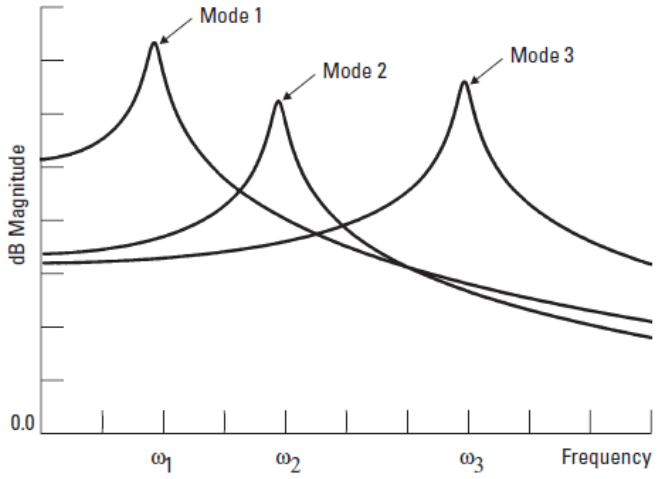

Figure 20. Example of SDOF Modal Contributions [19]

2.7 Calculation of Q-Factor

According to Silva [21], Q-factor may be represented by various parameters such as specific damping capacity, loss factor, damping and damping ratio. Attempting to measure damping, it is necessary to decide on the method that will best suit the nature of mechanical energy dissipation.

"It is extremely difficult to develop a realistic yet tractable model for damping in a complex piece of equipment operating under various conditions of mechanical interaction. Even if a satisfactory damping modal is developed, experimental determination of its parameters could be tedious. A major difficulty arises because it usually is not possible to isolate various types of damping (for example, material, structural, and fluid) from an overall measurement. " [21]

There are two ways to calculate Q-factor: using time domain response and frequency domain response of the system and five different methods to use. These five methods are summarized in below headings.

2.7.1 Logarithmic Decrement Method

This is the most popular time domain response method that is used to measure Q-factor. When a SDOF system is exited, its response takes the form of time decay.

Equation 9: $y(t) = y_0 \exp(-\zeta\omega_n t)\, sin\omega_n t$

Where damped natural frequency is given by

Equation 10: $\omega_d = \sqrt{1 - \zeta^2\omega_n}$

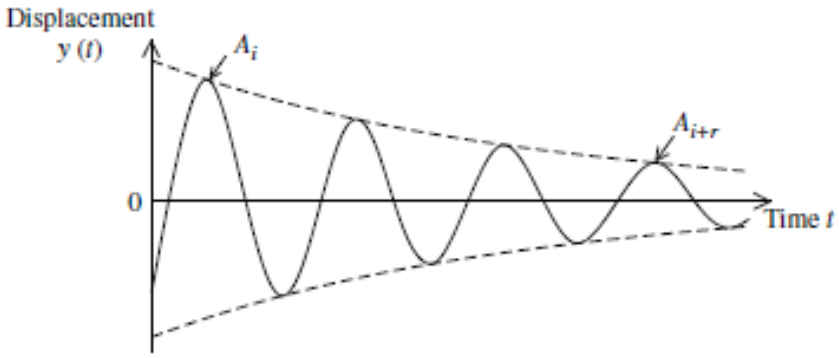

Figure 21. Impulse Response of a SDOF System [21]

A_i is the first significant amplitude and A_{i+r} is the amplitude after r cycles. According to [21], "Even though the above equation holds for any pair of points that are r periods apart in the time history, the peak points seem to be the appropriate choice for measurement in the present procedure, as these values would be more prominent than any arbitrary points in a response – time history. Then;

Equation 11: $\text{Logarithmic decrement, } \delta = \frac{1}{r} ln \frac{A_i}{A_{i+r}}$ (per cycle)

Equation 12: $\frac{\delta}{2\pi} = \frac{\zeta}{\sqrt{1-\zeta^2}}$ (per radian)

And for low damping ($\zeta < 0.1$),

Equation 13: $\zeta = \frac{\delta}{2\pi}$

Above equations can be used in SDOF systems. For MDOF systems, the damping ratio,ζ for each mode can be determined using above equations.

2.7.2 Step-Response Method

This method is also a time-response. When an excitation is applied in a unit-step to the SDOF system, its time-response is Equation 14.

Equation 14: $y(t) = 1 - \frac{1}{\sqrt{1-\zeta^2}} \exp(-\zeta\omega_n t) \sin(\omega_d t + \phi)$

Where $\phi = cos\zeta$.

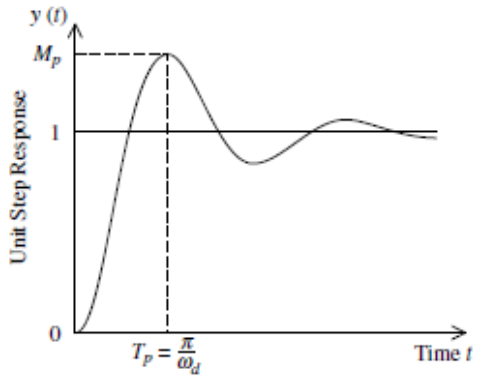

Figure 22. Step-Response of a SDOF System [21]

T_p is the peak time and M_p is the response at the peak time.

Equation 15: $T_p = \frac{\pi}{\omega_d} = \frac{\pi}{\sqrt{1-\zeta^2}}$

Equation 16: $M_p = 1 + \exp\left(-\zeta\omega_n T_p\right) = 1 + \exp\left(\frac{-\pi\zeta}{\sqrt{1-\zeta^2}}\right)$

According to [21], results of above equations are only valid for SDOF systems and modal excitations in MDOF systems. Moreover, while using above formulas, the response curve should be normalized to unit steady-state value.

2.7.3 Hysteresis Loop Method

The force vs. displacement cycle creates a hysteresis loop for damped systems. Depending on the inertial, elastic and gravitational forces this loop will change. However, the work done by these forces will be zero. The work done only due to damping will be equal to energy dissipation of the system. The area of the force and displacement loop will yield the damping capacity, ΔU.

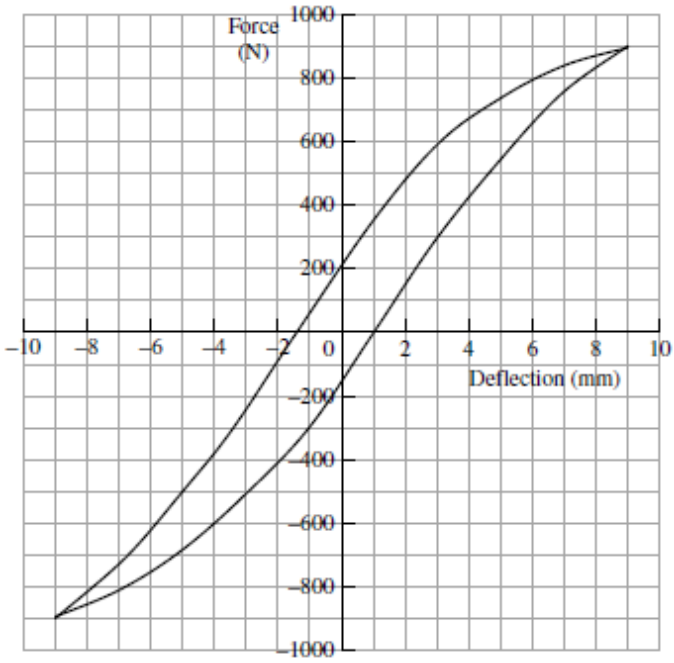

Figure 23. Sample Hysteresis Loop of A Damping Systems [21]

Hysteretic damping constant is calculated using Equation 17.

Equation 17: $h = \frac{\Delta U}{\pi x_0^2}$

where $x_0 = maximum\ displacement\ of\ hysteresis\ loop.$

Equivalent damping ratio is calculated using Equation 18.

Equation 18: $\zeta = \frac{h}{2k}$

where $k = average\ slope\ of\ the\ hysteresis\ loop.$

2.7.4 Magnification Factor Method

Since this thesis study is about low damping condition, only the low damping case is mentioned in this section of literature review. Magnification factor method is a frequency-response method.

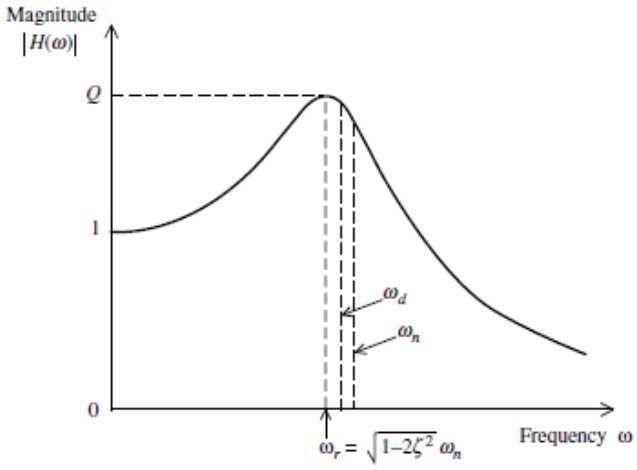

Figure 24. The Magnification Factor Method of Damping Measurement Applied to a SDOF System [21]

For low damping ($\zeta < 0{,}1$), the values of ω_n, ω_d and ω_r are nearly equal [21]. Q-factor is the magnitude of frequency-response function at resonant frequency.

Equation 19: $Q = \frac{1}{2\zeta\sqrt{1-\zeta^2}}$

For low damping ($\zeta < 0{,}1$),

Equation 20: $Q = \frac{1}{2\zeta}$

The damping ratio can be estimated by using Equation 20. In this method, curve must be normalized in order to obtain magnitude as unity at zero frequency as shown in Figure 24. Normalization of the magnitude value is carried out by taking the base ten logarithm and multiplying by a factor of 20, which gives decibels (dB).

2.7.5 Half-Power Bandwidth Method

Half-power bandwidth method is also a frequency-response method. The approach of this method is based on magnification factor method. $\frac{1}{\sqrt{2}}$ times the peak value Q gives the boundaries of bandwidth method. In this thesis study, half-power bandwidth method is implemented because this method is generally used for low

damping systems. According to Lalanne *et al*. [27], "the energy dissipated at the frequencies ω_1 and ω_2 are then equal to one-half of the energy dissipated at resonance." This is the why; the bandwidth is called half-power.

Similar to the magnification factor method, in this method curve must also be normalized in order to obtain magnitude as unity at zero frequency as shown in Figure 25. Normalization of the magnitude value is carried out by taking the base ten logarithm and multiplying by a factor of 20 which gives decibels (dB). [27]

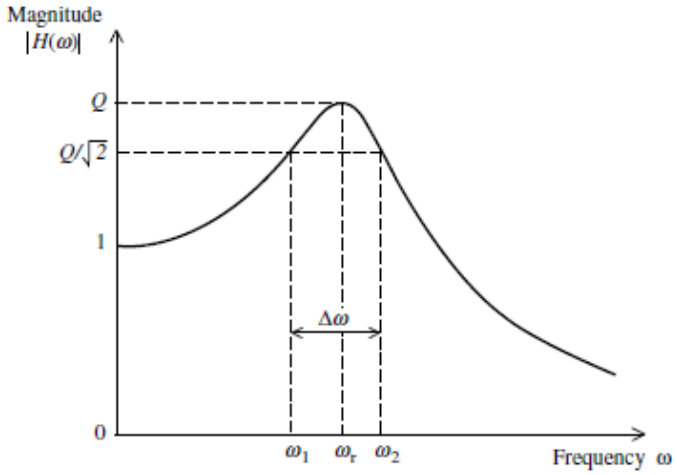

Figure 25. Bandwidth Method of Damping Measurement in SDOF System [21]

Equation 21: $Q = \frac{\omega_r}{\omega_2 - \omega_1}$

Equation 22: $20log_{10}\frac{\omega_{1,2}}{\omega_r} = 20log_{10}\frac{1}{\sqrt{2}} \simeq -3$

According to [28] Equation 22 justifies the frequently practical used technique of determining the half-power bandwidth by locating the frequencies on either side of resonance peak for which the response has decreased by three decibels.

2.8 Understanding Fe-Ni Superalloys

As the name implies, superalloys have certain characteristics that make them distinct from other materials. New generation superalloys may have 20 elements that makes superalloys difficult to understand the physics behind. Krasnykh et al.

[29] stated that in the Russian literature, Fe-Ni superalloys is also called precision alloys and their elasticity is specified in the form of separate group in the classification. In the non-Russian catalogs and standards, there is no separate classification of these alloys. The properties of these superalloys are determined after heat treatment operations. These heat treatment operations define the resistance to plastic deformation at normal and elevated temperatures after quenching and aging that are critical for Q-factor of materials.

“Superalloys are classified according to the main alloying elements in the composition, with the three base metals being nickel, cobalt, and iron. The entire superalloy family shares a common basic microstructure, which is a face-centered cubic (fcc) matrix with number of dispersed secondary strengthening phases. In elemental form, nickel is the only superalloy base metal with an fcc structure at room temperature. Cobalt is hexagonally close-packed (hcp) at room temperature but undergoes a transformation to fcc at 417 °C (783 °F). Iron has a body-centered cubic (bcc) structure at room temperature but undergoes a phase transformation to fcc austenite at 912 °C (1674 °F). In superalloys, both iron and cobalt are stabilized by the addition of nickel to retain an fcc crystal structure.” [30]

“Fe-Ni based superalloys evolved from austenitic stainless steels and are based on the principle of combining a closed packed FCC matrix with both solid solution hardening and precipitate-forming elements. The austenitic matrix is based on nickel and iron, with at least 25%Ni needed to stabilize the FCC phase. Other alloying elements, such as, chromium, partition primarily to the austenite for solid solution hardening” [31]

Since this type of superalloys have austenitic matrix with FCC structure, they have exceptional toughness. On the other hand, machinability of these superalloys is lower than other steels.

Fe-Ni superalloys are produced by three different production methods listed below.

1. Casting,

2. Powder Metallurgy Processing,
3. Wrought Processing

Regardless of the production process, due to reactivity of elements present in this type of superalloys, vacuum melting is a necessity. Cobalt and iron-based alloys are possible to melt in air by several methods; however, most of the nickel and iron-nickel superalloys vacuum induction melting (VIM) is necessary. The use of VIM decreases O_2 and N_2 concentration and enables to precise elemental control of Al and Ti. The precise control of interstitial gases and alloying elements increase mechanical properties and allows obtaining more reliable thermomechanical process selection. However, if materials with higher strength that should be hot worked for the place of use, a secondary melting process should be required which is vacuum arc remelting (VAR) and electroslag remelting (ESR). Powder metallurgy techniques should be processed in order to obtain more precise elemental control and higher strength.

Most of the iron-nickel superalloys are casted and deformed as bar, billet, plate, sheet, strip, or wire. Cold deformation and re-annealing lead to better mechanical properties due to the uniform and fine-grained microstructure.

2.9 Thermal and Mechanical Processing of Fe-Ni Superalloys

2.9.1 Annealing

In Iron-Nickel superalloys, annealing means full recrystallization and maximum softness. Annealing is used mainly to decrease hardness and increase ductility in order to ease forming, machining, or welding. Other usage area of annealing is to soften age-hardened structures by dissolving second phases. Precise control of annealing temperature is critical to final microstructure and mechanical properties. This precise control provides degrees of recrystallization and control of grain growth.

2.9.2 Solution Treating

“Solution treating is the first step of heat-treating superalloys. Temperature of solution treatment depends on the properties desired. High solution treating temperature is generally used for optimum creep-rupture properties by increasing grain growth and dissolving of carbides. The main objective is to put hardening phases into solution and dissolve some carbides. After aging, the resulting microstructure of the superalloys consists of large grains that contain heavy concentration of carbides in the grain boundaries. The lower solution treating temperature dissolves the principal aging phases without growth or significant carbide solution.” [31]

2.9.3 Quenching

“The purpose of quenching after solution treating is to maintain at room temperature the supersaturated solid solution obtained during solution treating. “ [31]. Quenching allows a finer precipitation size. Cooling can be done by oil and water quenching together with air or inert gas cooling. The interesting point of quenching age-hardenable alloys is internal stress coming from quenching may cause overaging.

2.9.4 Deformation

Iron, Cobalt and Nickel based superalloys are manufactured as bar, plate, sheet, wire and forgings by rolling, forging, or extrusion methods. Each method has its own process details. For instance, in rolling operation, many reheats, frequent conditioning and encasing of the alloy in a can is necessary. In forgings operations, rapid handling is essential to prevent edge cracking. Die closure rates and isothermal forging is key points in superalloys production.

2.9.5 Aging

Aging processes increases the strength of age-hardenable alloys by precipitation of one or more phases from super-saturated matrix. There are some factors affecting aging process selection. According to Davis, 1999 [31] there factors are:

- Type and number of precipitating phases available
- Service temperature
- Precipitate size
- The combination of strength and ductility desired and heat treatment of similar alloys

2.9.6 Microstructure and Phases of Fe-Ni Superalloys

Fe-Ni superalloys have austenitic fcc matrix phase gamma (γ) and various secondary phases changing with heat treatment procedure and composition of superalloys. Secondary phases which control the properties are carbides such as MC, $M_{23}C_6$ and M_6C in almost all superalloys; gamma prime (γ′) fcc $Ni_3(Al,Ti)$; gamma double prime (γ″) bct Ni_3Nb; eta (η) hexagonal ordered Ni_3Ti; delta (δ) orthorhombic Ni_3Nb intermetallic compounds in Ni- and Fe-Ni superalloys [32].

The gamma prime (γ′), gamma double prime (γ″), and eta (η) phases are known as geometrically close-packed (gcp) phases. The manufacture and control of the various phases, in addition to grain size and morphology, are what give superalloys their distinct features. Solid-solution hardeners and precipitated phases are primarily mechanisms for strengthening the superalloys. In Fe-Ni and Ni-superalloys, the principal strengthening precipitate phases are γ′ and γ″.

γ′ as principal strengthening phase in Fe-Ni and Ni- superalloys has crystal lattice varying in size from that of austenite matrix, shapes varying from spherical to cubic. They are varying with heat treatment parameters. Older Ni-based superalloys had spherical γ′ precipitate such as Waspaloy and Nimonic; however,

recently developed Fe-Ni base superalloys generally have cuboidal ones. Variations in molybdenum concentration and the aluminum/titanium ratio have been proven to alter morphology of γ′ in experiments [33]. According to [32], "with increasing γ/γ′ mismatch, the shape changes in the following order: spherical, globular, blocky, and cuboidal. When the γ/γ′ lattice mismatch is high, extended exposure above 700 °C (1290 °F) causes undesirable η (Ni_3Ti) or δ (Ni_3Nb) phases to form."

Summary of microstructure and phases of Fe-Ni Superalloys [32]:

- γ matrix is a fcc nickel-base nonmagnetic continuous phase with a large fraction of solid-solution elements like cobalt, iron, chromium, molybdenum, and tungsten. This phase serves as the matrix in all Fe-Ni and Ni-base alloys.
- Aluminum and titanium react with nickel to generate γ′, which is a phase that is coherent with the austenitic γ matrix. Other elements, like as niobium, tantalum, and chromium, are also present in this high temperature strengthening phase. When properly produced, it appears as spheres or cuboids.
- Metal carbides are formed when carbon in the range of 0.02 to 0.2-wt% reacts with reactive elements such as titanium, tantalum, hafnium, and niobium to create carbides. Several carbide phases exist. MC carbides tend to breakdown and create additional carbides, such as $M_{23}C_6$ and/or M_6C, along grain boundaries during heat treatment and service. Carbides can occur in nominal solid-solution alloys after long periods of service.
- Sigma phase (σ) has a tetragonal lattice and is considered to be the most common minor phase in Fe-Ni superalloys. It has been observed as a continuous and massive grain boundary angular constituent and large widmanstatten platelets. It may exist in metastable phase. Generally, it is considered very detrimental to properties but a block morphology within fine grains.

- Eta phase (η) found in Fe-Ni superalloys with high titanium/aluminum ratios may form intergranularly in a cellular from or intergranularly as acicular platelets in a widmanstatten pattern. This phase may exist in a matestable form as a titanium-rich γ′ before transforming to η.
- Precipitates help to strengthen an alloy by preventing it from deforming under strain. The following are some of the main hardening precipitate features that act to prevent deformation:
  - Degree of mismatch between precipitate and matrix
  - Precipitate order
  - Precipitate size

2.10 Anelastic Relaxation Mechanisms in Fe-Ni Superalloys

Since Q-factor is loss of energy in a mechanical structure as defined in section 2.4, it is directly related to the internal friction of materials and as defined in [34], anelastic relaxation is the main source of internal friction. There are four main relaxation mechanisms dominating internal friction in Fe-Ni superalloys [34].

- Point defect relaxation
- Dislocation relaxation
- Grain boundary relaxation
- Twin boundary relaxation

2.10.1 Point Defect Relaxation

Diffusion under stress ("point defect relaxation") is an anelastic relaxation generated by a diffusive redistribution of point defects under the action of an applied stress. This necessitates an elastic interaction between the applied stress and the point defects' distortions of a crystal lattice (or possibly a non-crystalline matrix), such that the internal equilibrium distribution of the defects is changed and

a driving force for directed diffusion is produced under the action of the external stress.

The classical Snoek relaxation is an anelastic relaxation generated by "heavy" interstitial atoms (IA) in body-centered cubic (bcc) metals, initially defined by Snoek (1941) [35] to explain the damping due to C in α-Fe.

It's found in O, N, and C interstitial solid solutions in metals from the VB of periodic table (V, Nb, Ta) and VIB (Cr, Mo, W) groups, as well as in α-Fe. Many bcc dilute and concentrated substitutional alloys exhibit Snoek-type relaxation, i.e., the same process applied to alloys, where the interaction between interstitial and substitutional atoms effects the relaxation parameters.

Mechanical relaxation requires a deformation of the lattice around a defect with a lower symmetry than the crystal lattice; consequently, single vacancies or single substitutional atoms in a cubic lattice will not create any relaxation effect on loading. However, as Zener (1943, 1947) [36] [37] demonstrated for a α-brass alloy (Cu–Zn), the presence of solute next neighbor pairs or clusters causes a relaxation maximum, referred to as the "Zener Peak", at a temperature range where the solute atoms are mobile, and the applied stress allows for reorientation of the solute atom pair in the lattice. This is true not only for fcc, but for all crystal kinds (bcc, hcp).

2.10.2 Dislocation Relaxation

Dislocations are crystal line defects that are distinguished by their complex distortion or stress field (e.g., Hull and Bacon 1984 [38], Hirth and Lothe 1968 [39]) and can exhibit a wider range of relaxation effects than point defects. These effects can be seen in plastically deformed metals and alloys with a high dislocation density.

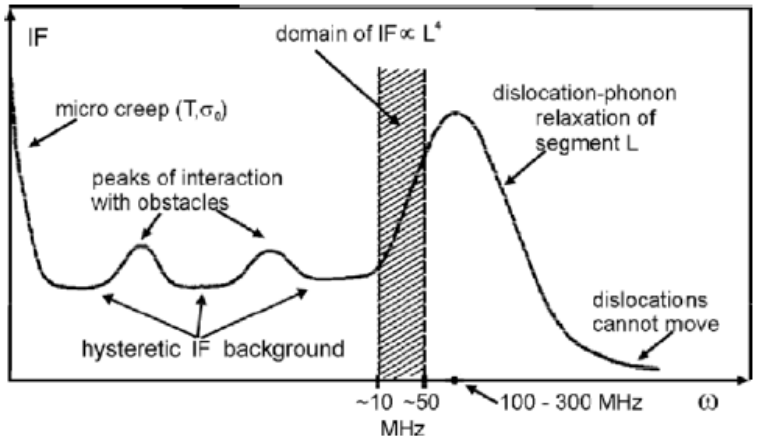

Figure 26. Internal friction due to dislocations on the frequency scale [40]

Figure 26 depicts distinct dislocation damping contributions over a wide range of applied vibration frequencies. Because dislocation motion is usually associated with elongation of the dislocation line (e.g., bowing out between anchoring points and nucleation of kinks), the dislocation line energy ("line tension") generates a restoring force, which in theory would infer a dislocation resonance phenomenon. However, because phonon relaxation effects greatly overdamped dislocation movement (Alshits and Indenbom 1986 [41], Granato and Lucke 1956 [42]), we may ignore the restoring force and focus on relaxation effects in the following. In damping studies, the dislocation motion generated by the applied alternating shear stress frequently suggests an amplitude dependency on internal friction. The relaxation peaks can be split into the following categories [34]:

1. Those induced by dislocation movement as a result of thermal or geometrical kink nucleation and propagation (Bordoni, Niblett– Wilks)
2. Those generated by dislocations and suitable lattice point defects (vacancies, self-interstitials: Hasiguti maxima typically below room temperature)
3. At higher temperatures, those induced by dissolved foreign interstitial atoms and dislocations (Snoek–Koster relaxation, dislocation-enhanced Snoek effect)

4. Those induced by dislocation climbing or other diffusion-controlled processes at even higher temperatures

2.10.3 Grain Boundary Relaxation

C. Zener (1941) [36] was one of the first to explore grain boundary relaxation as a cause of damping in polycrystals at sufficiently high temperatures (Barnes and Zener 1940 [43]). He talked about the anelastic strain caused by grain boundary sliding caused by shear force and slide along the border between two neighboring crystals. The back tension that builds up at the triple junctions where the boundary terminates causes the restoring force.

In materials with extremely fine grains, where the grain boundary regions make up a significant portion of the overall sample volume, grain-boundary relaxation may become dominant. These nanocrystalline materials (formed, for example, by severe plastic deformation) have grain boundary structures that are largely out of balance and have unique mechanical characteristics.

2.10.4 Twin Boundary Relaxation

A twin boundary is a form of grain boundary that separates two "twin" crystallites that are mirror copies of one other in terms of their lattice (which is possible only at a well-defined misorientation angle). A coherent twin boundary is one where the twin boundary is the same as the mirror plane, which is generally a low-indexed, close-packed crystallographic plane. Because the twin crystals can be turned into each other by a shear transformation parallel to the mirror plane, the creation of twins, which can occur under high stress or during recrystallization (in metals and alloys with low stacking-fault energy), is an additional deformation process. A shear deformation is also caused by a perpendicular shift of a twin boundary (growth of one twin at the cost of the other).

Stress-induced movement of twin borders must be sufficiently movable for anelastic relaxation and internal friction peaks to occur. The relaxation process cannot include interfacial sliding since crystallographic coherency occurs across the twin surfaces (Nowick and Berry 1972 [44]). However, partial dislocation movement can shift specific types of twin borders (Hirth and Lothe 1968 [39]); the appropriate dislocation processes will therefore be implicated in twin boundary relaxation.

CHAPTER 3

EXPERIMENTAL PROCEDURES

3.1 Materials Used for the Experiments

Four different materials were used produced by Auremo Evek GmbH in St. Petersburg, Russia. The company declare in the certificate that these 4 different materials are produced according to Russian standard GOST 14119-85 as round bar. These four materials are Ni-SPAN C902, 42NiCrTiAl, 44NiCrTiAl and 36NiCrTiAl. There is no equivalent AISI designation of these alloys. They are called Fe-Ni Superalloys. As it is mentioned in literature review section, these alloys are used in precision applications and due to their heat resistance property, they are used in heat resistant applications.

Table 2. Sample Designation vs. Materials Matrix

Sample Designation	Materials
1	Ni-Span C902
2	42NiCrTiAl
3	44NiCrTiAl
4	36NiCrTiAl

3.2 Material Characterization

3.2.1 Spectroscopy

Spectroscopic analysis of these alloys is carried out in the Spectromaxx LMX07 Arc/Spark Optical Emission Spectroscopy Analyzer machine (Figure 27) produced by the company SPECTRO. Spectroscopic analysis is made using Ni-01-F method

and calibrated in this method. There measurements were done to each sample and coefficient of variances (CoV) are calculated in order to show the reliability of the machine and uniformity of chemical composition of each sample. Otherwise, inconsistent results may lead to wrong evaluation and expensive rework. Coefficient of variances (CoV) are evaluated with the help of ASTM Committee's Symposium on Spectroscopic Excitation proceedings.

Figure 27. Spectromaxx LMX07 Arc/Spark Optical Emission Spectroscopy Analyzer [45]

3.2.2 Metallography

4 different materials were subjected to metallographic examination and after every heat treatment, metallographic examinations are repeated. These examinations are carried out after cutting, grinding, polishing, and etching. After that, microstructures are characterized by Huvitz HDS 5800 shown in Figure 28.

Figure 28. Huvitz HDS 5800 Digital Microscope [46]

Etching solution selection is quite intricate to figure out due to limited utilization of selected 4 different Fe-Ni superalloys each one has different Ni, Cr, Ti, Al content. ASM Handbook Volume 9: Metallography and Microstructure Handbook [47] helps to find out correct etchant. Only waterless Kalling's etchant closes to perfect microstructure in order to measure correct grain size. Waterless Kalling's solution or Kaaling's No.2 reagent is consisting of 5 g of $CuCl_2$, 100 mL HCl and 100 mL ethanol. This etchant did not yield proper solutions for each of the materials. So, it is necessary to optimize the etchant. Best solution for the materials used in this thesis study is 5 g of $CuCl_2$, 20 mL HNO_3, 80 mL HCl, 80 mL ethanol. For this optimization process, Guide to Etching Specialty Alloys [48] shows the way of optimization for etchant for superalloys.

Grain size measurement were done using ASTM E112-13 Standard test method for determining average grain size [49] by Huvitz HDS 5800 digital microscope [46].

3.2.3 Hardness Testing

Hardness values were measured by EMCO DuraScan G5 hardness testing machine (Figure 29). Measurements were taken in Vickers. 10 kgf force is applied, indenter length 5 mm, diameter 6 mm and calibrated according to EN ISO 6507-2 [50]. Hardness data is represented in HV10 scale. At least seven hardness measurements were taken for every heat treatment.

Figure 29. EMCO DuraScan G5 Hardness Testing Machine [51]

3.2.4 Tensile Testing

Tensile tests were carried out in Instron Tensile Test Machine 4507 with Instron 2663-821 model video extensometer in z-direction shown in Figure 30. Instron 2518-111 model class 0,5 100kN load-cell was used. Modulus measurements are important for finite element analysis during Q-factor testing. Tensile tests are carried out with respect to ASTM E8 [52]. The crosshead speed is 0,5mm/min. Tensile test specimens are prepared using Figure 8 Standard 12.5-mm [0.500-in.] Round Tension Test Specimen and Examples of Small-Size Specimens

Proportional to the Standard Specimen in ASTM E8 [52]. At least three tensile tests were carried out for each heat treatment process selected.

Figure 30. Instron Tensile Testing Machine [53]

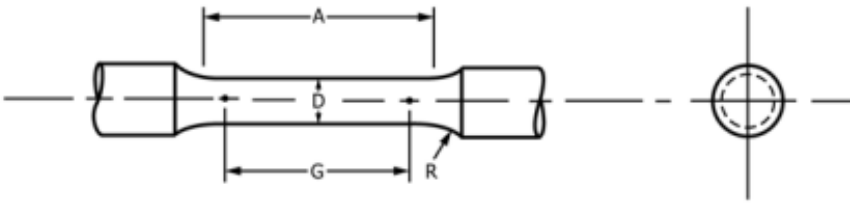

Dimensions, mm [in.]	
G—Gauge length	30.0 ± 0.1 [1.250 ± 0.005]
D—Diameter (Note 1)	6.0 ± 0.1 [0.250 ± 0.005]
R—Radius of fillet, min	6 [0.188]
A—Length of reduced parallel section, min (Note 2)	36 [1.4]

Figure 31. Tensile Test Specimen Dimensions [52]

3.3 Heat Treatment Process Selection

Seven different heat treatment process is carried out in order to actuate different strengthening mechanisms. All four different materials Ni-SPAN C902, 42NiCrTiAl, 44NiCrTiAl and 36NiCrTiAl are subjected to the same heat treatment charge. Phase diagrams of these Fe-Ni superalloys were analyzed using Thermo-Calc software.

Table 3. Heat Treatment Process Details

Heat Treatment Number	Heat Designation	Recipe Details
1	Q	6 minutes at 917°C and water quenched
2	A	6 minutes at 917°C, water quenched, 2 hours at 645°C and air cooled
3	Q+	30 seconds at 970°C and water quenched
4	A+	30 seconds at 970°C, water quenched, 2 hours at 650°C and air cooled
5	M	5 hours at 482°C and air cooled
6	S	30 seconds at 910°C (heating rate of 10°C/min) and air cooled
7	M+	5 hours at 730°C and air cooled

A+ and M+ heat charges are chosen to test Q-factor. Selection details are discussed in the discussions part of the study.

Heat treatment processes are carried out using Nabertherm muffle furnace (Figure 32).

Figure 32. Nabertherm Laboratory Scale Muffle Furnace [54]

3.4 Q-Factor Tests

Q-factor tests are carried out by No:"TR 2014 15767 Y" patented test machine [18]. This machine is called Modal Test Robot (MTR in Figure 33). MTR consists of granite table, support structure with hammer mechanism. The hammer can move in x-y-z directions and support structure can also tilt the hammer in two horizontal axes and can rotate the hammer around vertical axes. Thus, the hammer can touch any surface of the test parts. PCB model 086E80 modal test hammer shown in Figure 34 was used with flexible handle.

Figure 33. The MTR Test Setup [26]

Figure 34. Miniature Accelerometer and the Impact Hammer Used in The MTR Setup [26]

The elasticity of miniature modal test hammer handle provides the same impact energy every time so that reliable test results can be obtained. Response of the hammer was measured using PCB model 352C23 ICP accelerometers as shown in Figure 34.

Modal Test Robot (MTR) has data acquisition system integrated LMS SCADAS Mobile SCM01 with V8. LMS Test Lab 17A Impact Testing software was used in data acquisition during impact testing with MTR. This software can give frequency response function (FRF) data and using this data, it can also estimate the natural frequencies and damping ratios of the samples.

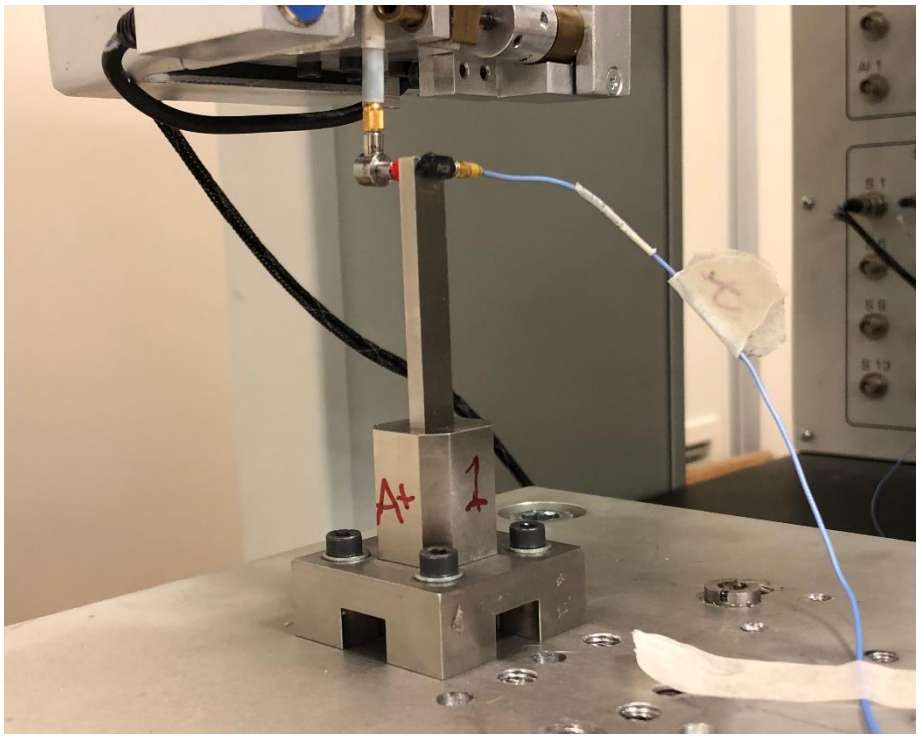

Figure 35. Tests for the Q-factor on MTR

Q-factor test sample geometry is shown in Figure 36. Tolerances are given in terms of ISO 2768-mK [55]. This geometry is chosen in order to obtain the closest natural frequency of tests and analysis, and better Q-factor measurements. Since MTR is a patented machine, comparing the Q-factor test results with literature is not correct. It is only for comparison purposes.

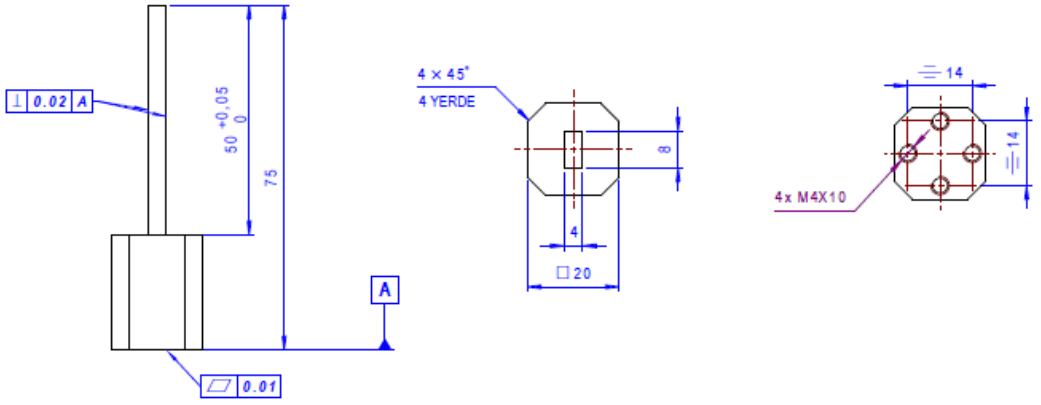

Figure 36. Q-Factor Sample Geometry

3.5 Flowchart of Experimental Procedure

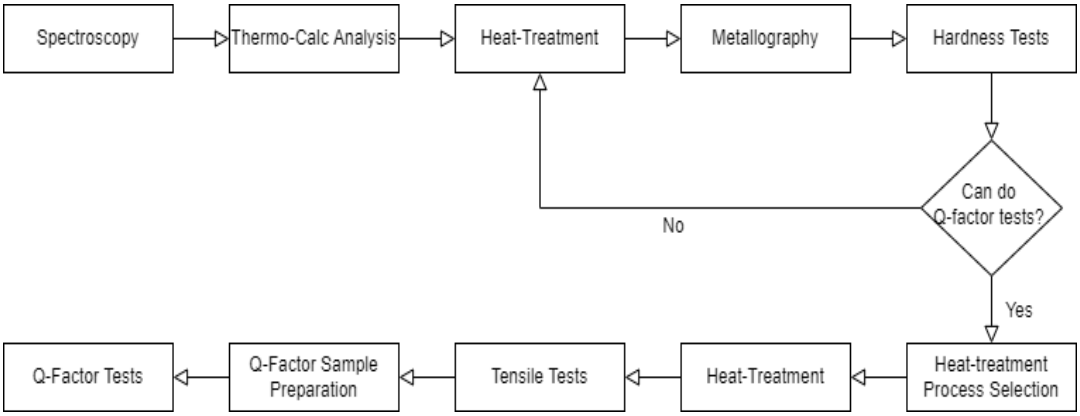

Figure 37. Flowchart Experimental Procedure

CHAPTER 4

RESULTS & DISCUSSION

4.1 Material Characterization of As Received Materials

4.1.1 Spectroscopy

Spectroscopy results of 4 different materials are shown below.

Table 4. Spectroscopy Results of As Received Materials

Materials	*C*	*Ni*	*Cr*	*Ti*	*Al*	*Mn*	*Balance Fe*
Ni-Span C902	0.0319	35.8110	11.6269	2.6104	0.9340	0.8052	46.8430
42NiCrTiAl	0.0277	43.1281	4.9364	1.8498	0.4535	0.5271	47.9771
44NiCrTiAl	0.0344	46.2244	4.8116	2.0619	0.5530	0.4483	44.8708
36NiCrTiAl	0.0529	35.1844	12.6269	2.6053	1.0249	1.1383	46.3178

Three measurements were done, and coefficient of variances (CoV) were calculated in Table 5.

Table 5. Coefficient of Variances (CoV) of The Spectroscopy Results

Materials	*C*	*Ni*	*Cr*	*Ti*	*Al*	*Mn*	*Balance Fe*
Ni-Span C902	0.6161	0.2043	0.0989	1.8758	0.0815	0.1618	0.0939
42NiCrTiAl	4.0163	0.2040	0.1631	1.3123	0.4708	0.3261	0.1416
44NiCrTiAl	0.1454	0.0530	0.1701	0.8395	0.0667	0.0726	0.0458
36NiCrTiAl	9.7822	0.2400	1.4667	1.0171	0.6489	0.5943	0.1189

It can be seen from Table 5 that highest variance comes from Carbon which is not as critical as other alloying elements and according to symposium by ASTM

Committee “If coefficients of variation of 1 or 2 percent are acceptable, determination of the major constituents of a sample by spectrographic techniques is often feasible.” [56]

4.1.2 Thermo-Calc Analysis

From Figure 38, Figure 39, Figure 40 and Figure 41 shows Thermo-Calc analysis of Ni-Span C902, 42NiCrTiAl, 44NiCrTiAl and 36NiCrTiAl using nickel-based superalloys databases of Thermo-Calc

Using this software stable phases at heat treatment temperatures are simulated in Table 6.

Table 6. Stable phases at heat treatment temperatures Thermo-Calc simulation

Heat Treatment Number	Heat Designation	Stable Phases of Ni-Span C902 and 36NiCrTiAl	Stable Phases of 42NiCrTiAl and 44NiCrTiAl
1	Q	FCC_A1#1	FCC_A1#1
2	A	FCC_A1#1 and Ni_3Ti	FCC_A1#1 and Ni_3Ti
3	Q+	FCC_A1#1	FCC_A1#1
4	A+	FCC_A1#1 and Ni_3Ti	FCC_A1#1 and Ni_3Ti
5	M	FCC_A1#1, Ni_3Ti and FeCr (sigma,σ)	FCC_A1#1 and Ni_3Ti
6	S	FCC_A1#1	FCC_A1#1
7	M+	FCC_A1#1 and Ni_3Ti	FCC_A1#1 and Ni_3Ti

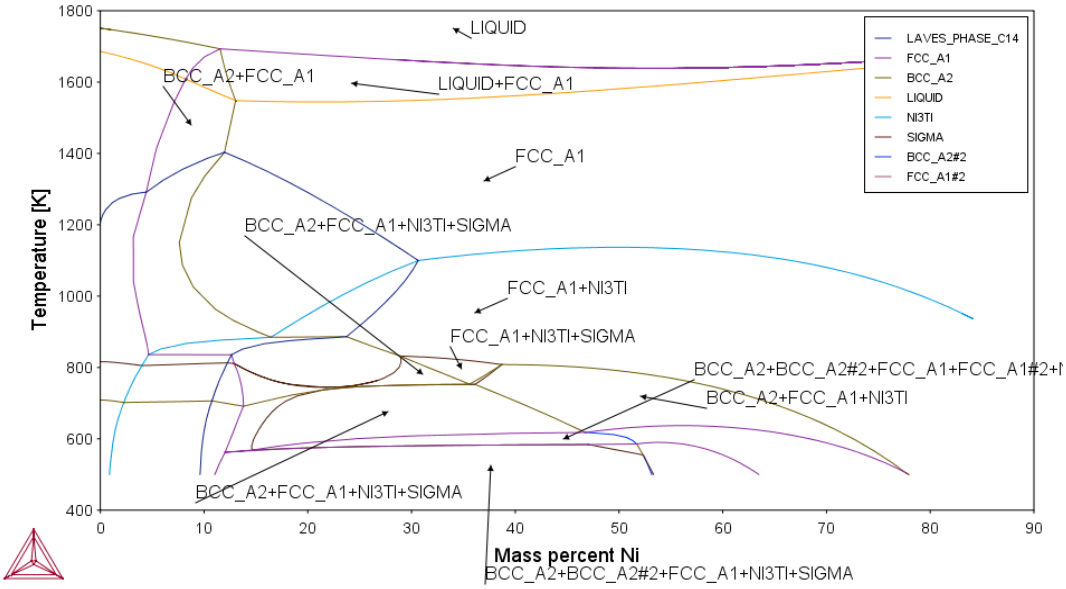

Figure 38. Thermo-Calc Analysis of Ni-Span C902

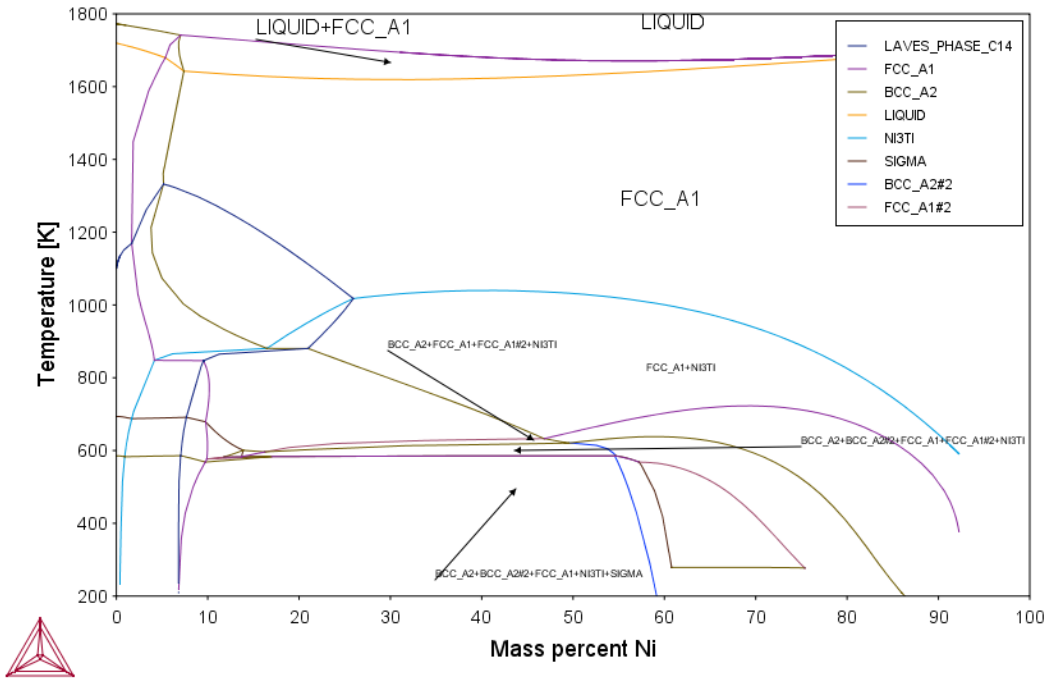

Figure 39. Thermo-Calc Analysis of 42NiCrTiAl

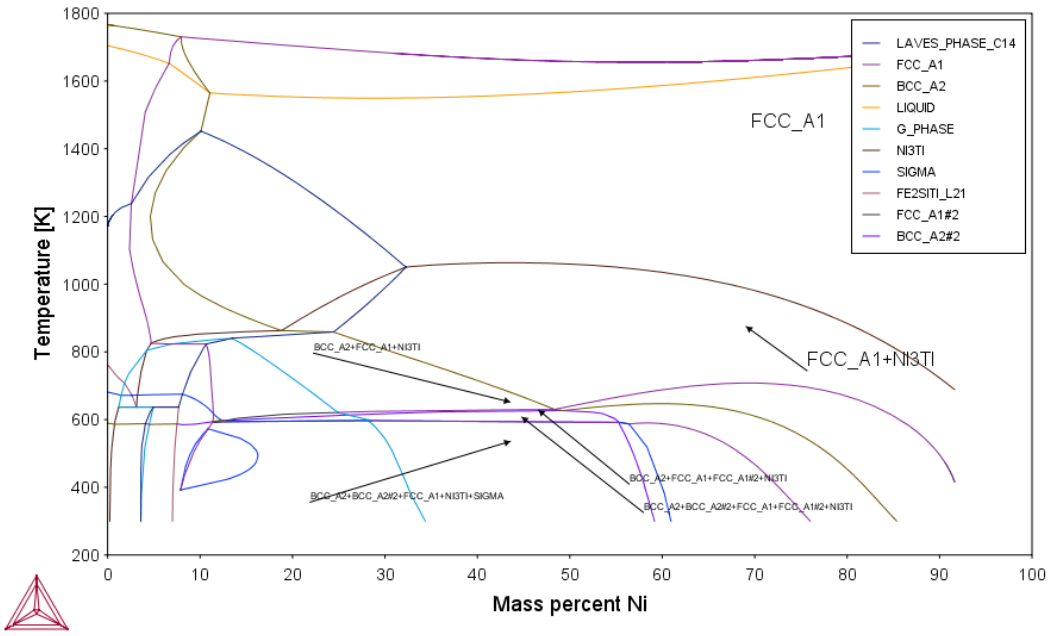

Figure 40. Thermo-Calc Analysis of 44NiCrTiAl

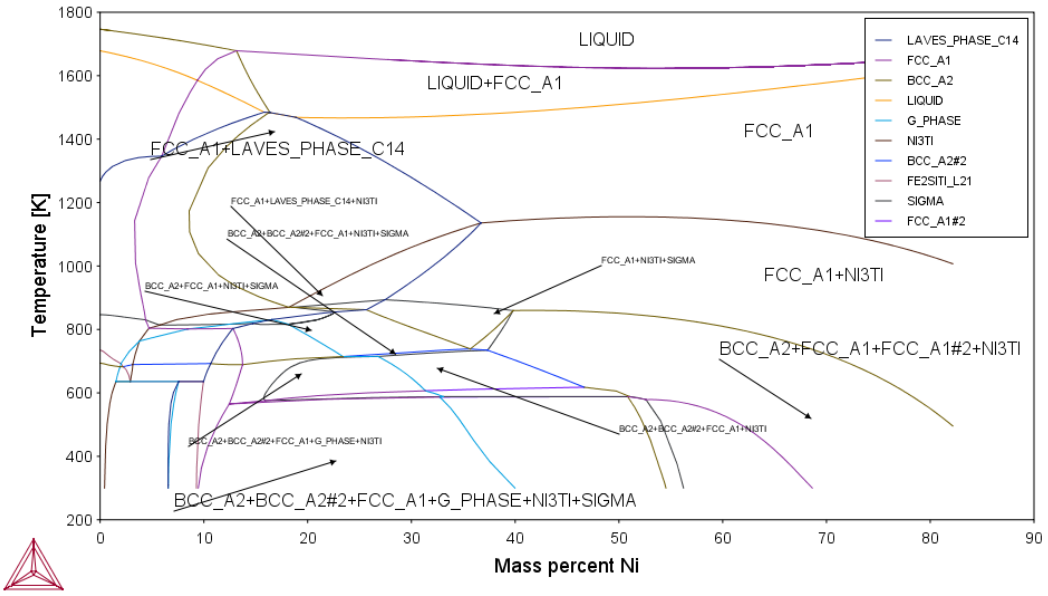

Figure 41. Thermo-Calc Analysis of 36NiCrTiAl

4.1.3 Tensile Testing

Tensile test results of as received four different materials are shown below. Tensile testing was carried out to as received condition, A+ and M+ heat treated materials.

Table 7. Mechanical Test Results of As Received Materials

Materials	*Maximum Load (kN)*	*Tensile Stress (MPa)*	*Yield Stress (Offset 0.2 %) (MPa)*	*Tensile Strain (%)*	*Modulus (E-modulus) (MPa)*
Ni-Span C902	40.305	1316.0	898.5	22.9	236329
42NiCrTiAl	34.675	1222.5	785.5	24.0	199743
44NiCrTiAl	35.265	1243.0	934.5	16.3	192877
36NiCrTiAl	36.585	1279.0	838.0	24.3	200978

4.1.4 Hardness Testing

Seven hardness measurements were taken for each of the materials' as received condition.

Table 8. Hardness Test Results of As Received Materials

Materials	*HV 10*	*CoV*
Ni-Span C902	365.7	3.4
42NiCrTiAl	377.2	1.9
44NiCrTiAl	326.2	5.6
36NiCrTiAl	326.7	5.1

4.1.5 Microstructural Analysis

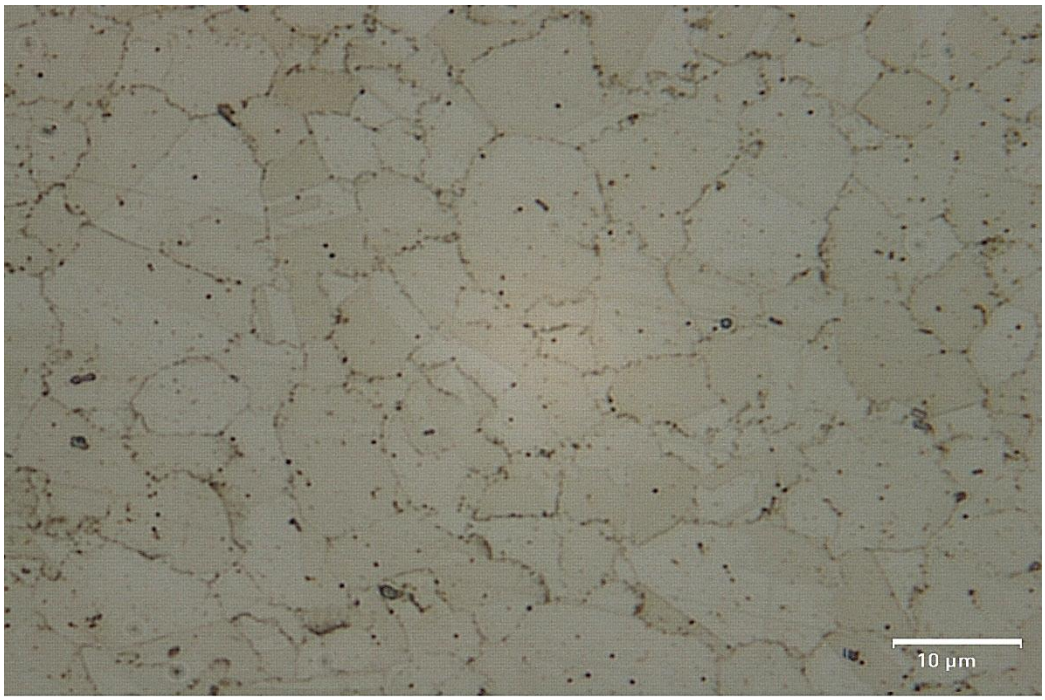

Figure 42.Microstructure of Ni-Span C902 as received condition

It can be inferred from Figure 42 that Ni-Span C902 as received condition has average grain size of 8.5 µm with Ni_3Ti as γ′ phase in the vicinity and boundaries of grains.

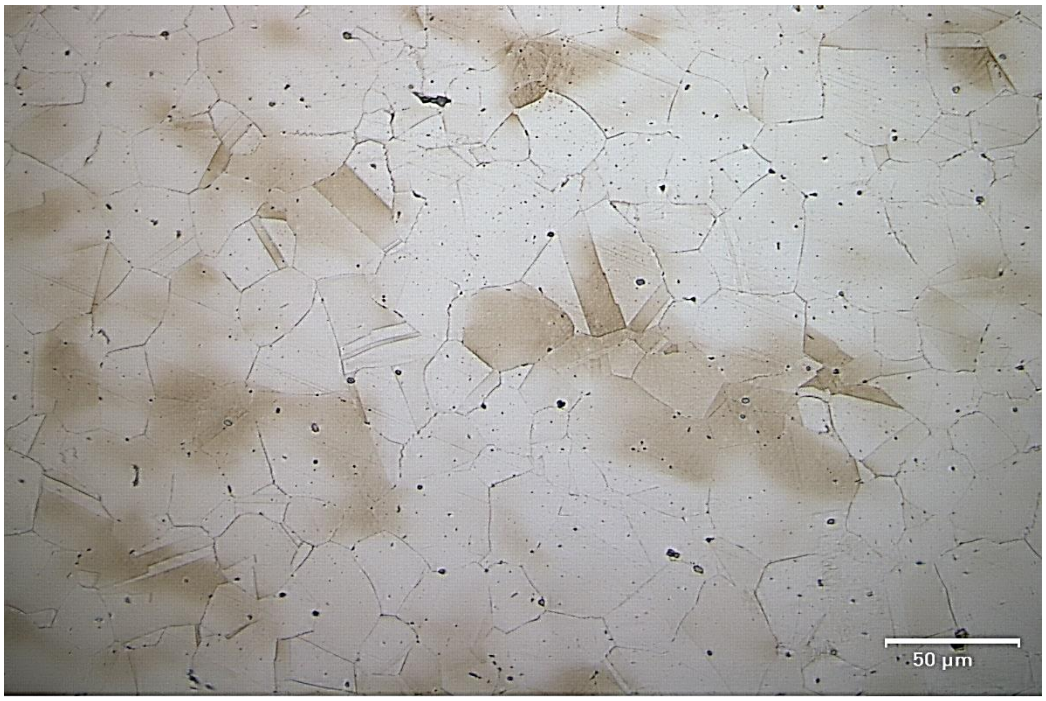

Figure 43. Microstructure of 42NiCrTiAl as received condition

From Figure 43, 42NiCrTiAl as received condition has average grain size of 35.1 µm with Ni_3Ti as γ′ phase mostly in the vicinity of grains. There are also some annealing twins.

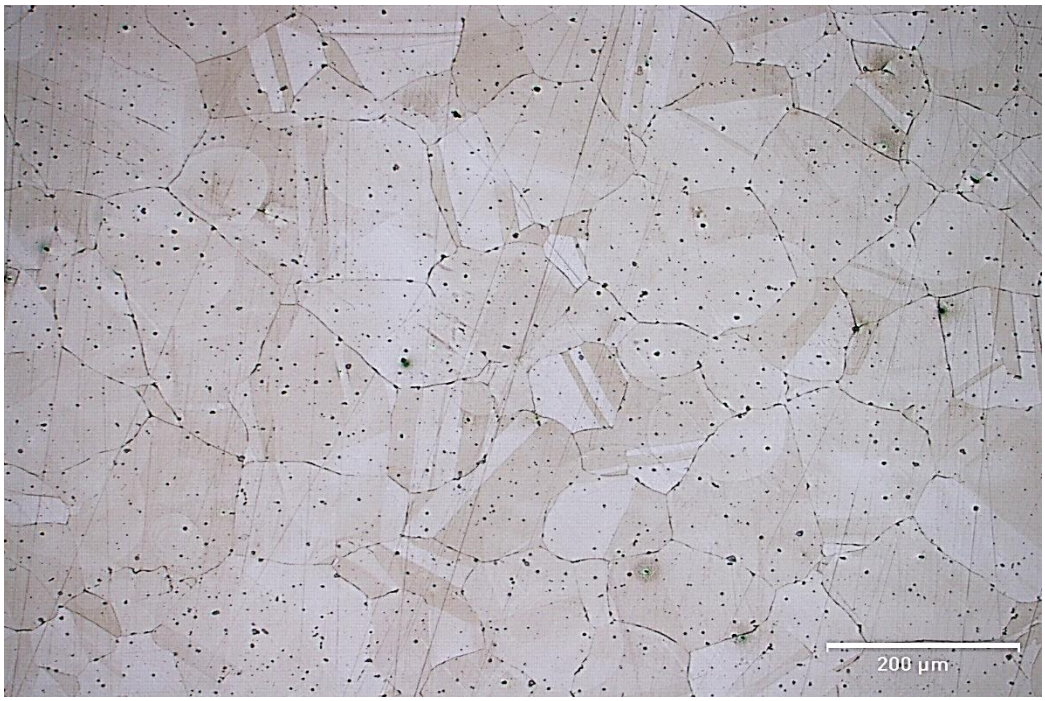

Figure 44. Microstructure of 44NiCrTiAl as received condition

From Figure 44, 44NiCrTiAl as received condition has average grain size of 137.7 µm with Ni_3Ti as γ′ phase evenly distributed in the vicinity of grains. There are also some annealing twins. Grain sizes are not uniform in size.

Figure 45. Microstructure of 36NiCrTiAl as received condition

It can be inferred from Figure 45 that 36NiCrTiAl as received condition has average grain size of 24.5 µm with Ni_3Ti as γ′ phase in the vicinity and boundaries of grains.

Table 9. Average Grain Size of As Received Materials

Materials	*Average Grain Size(µm)*	*StDev*
Ni-Span C902	8.5	2.8
42NiCrTiAl	35.1	4.3
44NiCrTiAl	137.7	38.6
36NiCrTiAl	24.5	3.9

4.2 Material Characterization of "Q" Heat Treatment Process

4.2.1 Hardness Testing

"Q" heat treatment recipe is 6 minutes at 917°C and water quenched. Seven hardness measurements were taken for each of the heat-treated materials.

Table 10. "Q" Heat Treatment Process Hardness Test Results

Materials	*HV 10*	*CoV*
Ni-Span C902	239.8	1.7
42NiCrTiAl	171.0	2.1
44NiCrTiAl	218.4	8.1
36NiCrTiAl	302.7	0.7

4.2.2 Microstructural Analysis

Figure 46. Microstructure of "Q" Heat Treated Ni-Span C902

It can be seen in Figure 46 that average grain size of “Q” heat treated Ni-Span C902 is 9.0 µm and has second phase Ni_3Ti as γ′ 3-5 µm in dimension.

Figure 47. Microstructure of “Q” Heat Treated 42NiCrTiAl

It can be seen in Figure 47 that average grain size of “Q” heat treated 42NiCrTiAl is 34.4 µm and has bigger second phase Ni_3Ti as γ′ than as received condition 42NiCrTiAl.

Figure 48. Microstructure of “Q” Heat Treated 44NiCrTiAl

From Figure 48, “Q” heat treated 44NiCrTiAl has average grain size of 134.4 µm with Ni_3Ti as γ′ phase evenly distributed in the vicinity of grains. There are also some annealing twins. Grain sizes are not uniform in size since standard deviation is 37.8.

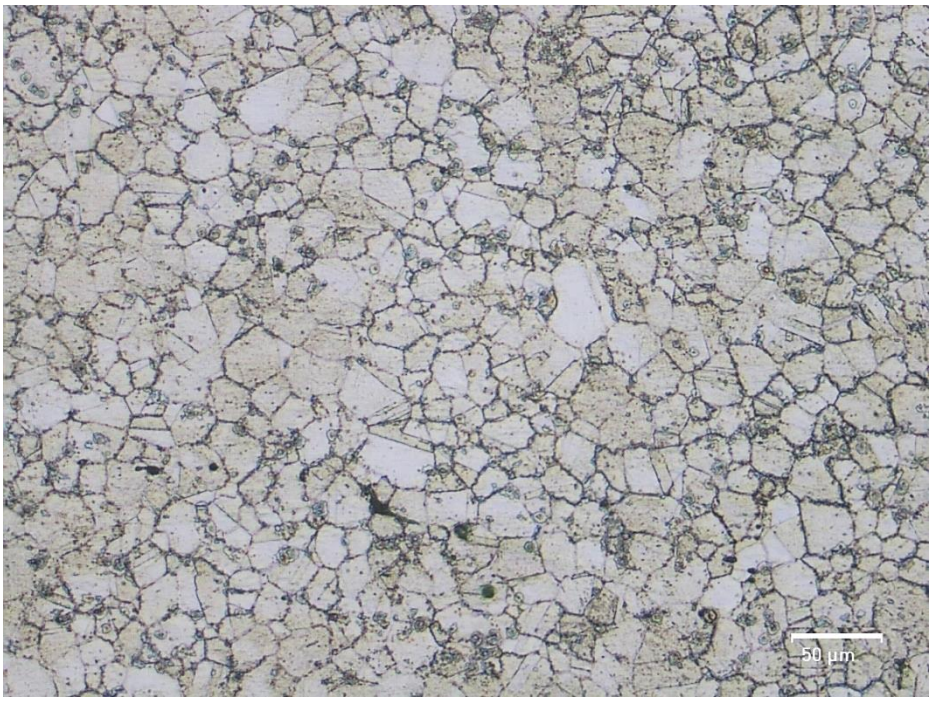

Figure 49. Microstructure of "Q" Heat Treated 36NiCrTiAl

It can be seen from Figure 45 that "Q" heat treated 36NiCrTiAl has average grain size of 24.4 µm with Ni_3Ti as γ′ phase in the vicinity and boundaries of grains.

Table 11. Average Grain Size of "Q" Heat Treated Materials

Materials	*Average Grain Size(µm)*	*StDev*
Ni-Span C902	9.0	2.9
42NiCrTiAl	34.4	8.6
44NiCrTiAl	132.2	37.8
36NiCrTiAl	24.4	4.0

4.3 Material Characterization of "A" Heat Treatment Process

4.3.1 Hardness Testing

"A" heat treatment recipe is 6 minutes at 917°C, water quenched, 2 hours at 645°C and air cooled. Seven hardness measurements were taken for each of the heat-treated materials.

Table 12. "A" Heat Treatment Process Hardness Test Results

Materials	*HV 10*	*CoV*
Ni-Span C902	378.0	1.2
42NiCrTiAl	319.8	4.7
44NiCrTiAl	329.0	2.1
36NiCrTiAl	390.4	4.2

4.3.2 Microstructural Analysis

Figure 50. Microstructure of "A" Heat Treated Ni-Span C902

It can be seen in Figure 50 that average grain size of "A" heat treated Ni-Span C902 is 9.0 µm and has second phase Ni_3Ti as γ′. There are also precipitations in the grain boundaries.

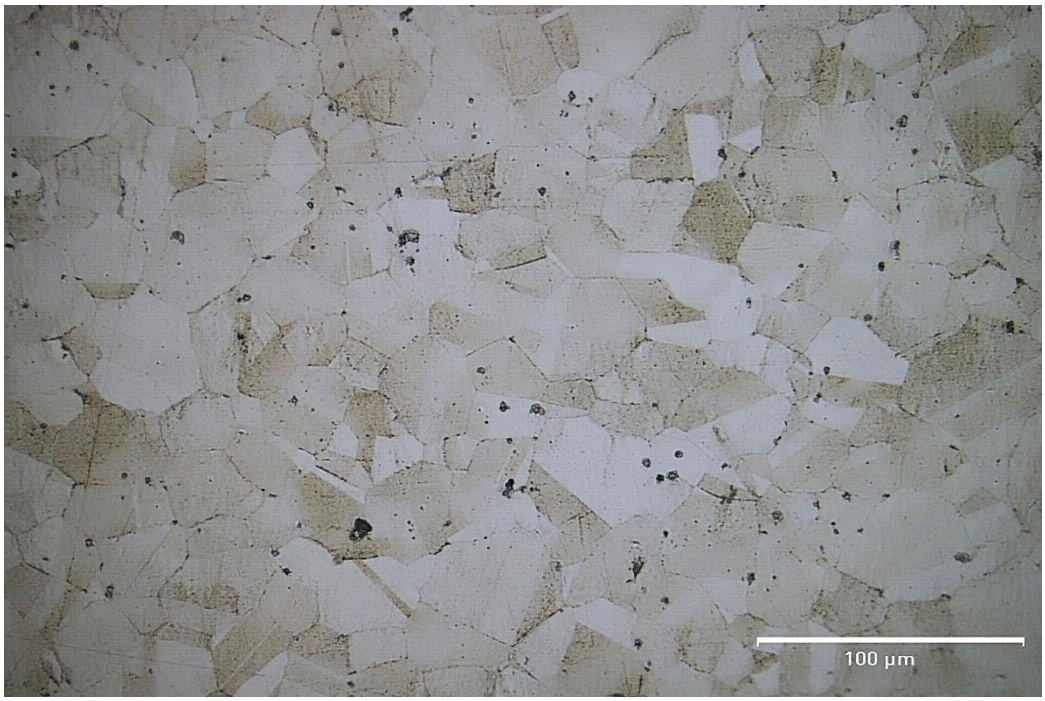

Figure 51. Microstructure of “A” Heat Treated 42NiCrTiAl

It can be seen in Figure 51 that average grain size of “A” heat treated 42NiCrTiAl is 26.3 µm and has bigger second phase Ni_3Ti as γ' than as received condition 42NiCrTiAl. Grain size is reduced by 25% from as received condition.

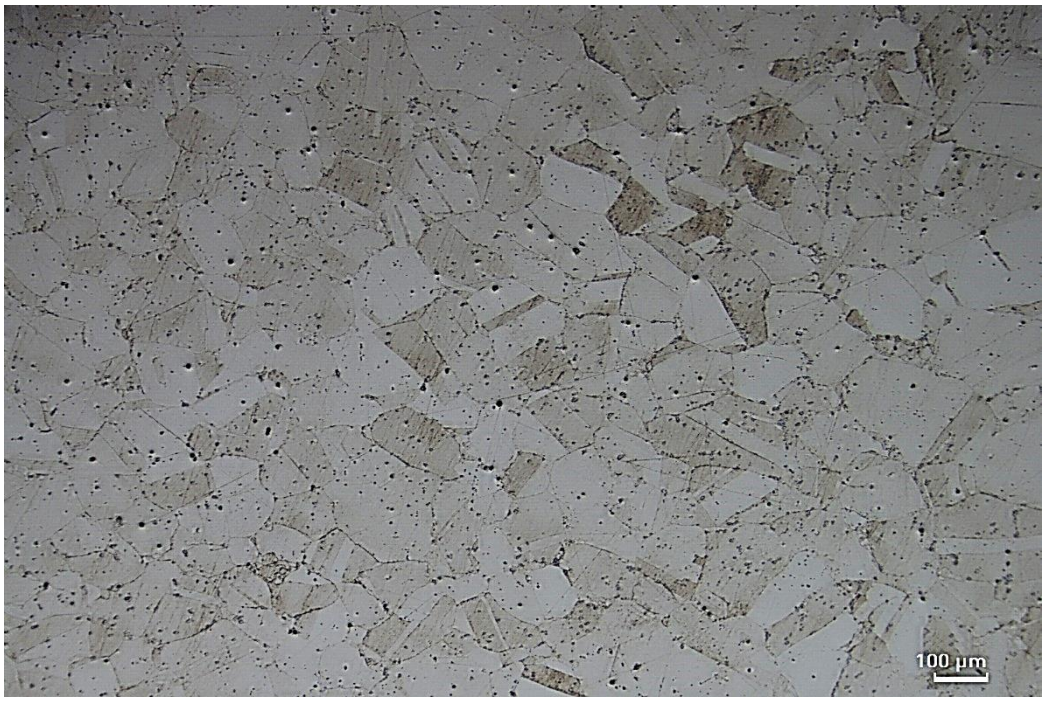

Figure 52. Microstructure of “A” Heat Treated 44NiCrTiAl

From Figure 52, “A” heat treated 44NiCrTiAl has average grain size of 135.3 µm with Ni_3Ti as γ′ phase evenly distributed in the vicinity of grains. There are also some annealing twins. Grain sizes are not uniform in size since standard deviation is 41.5.

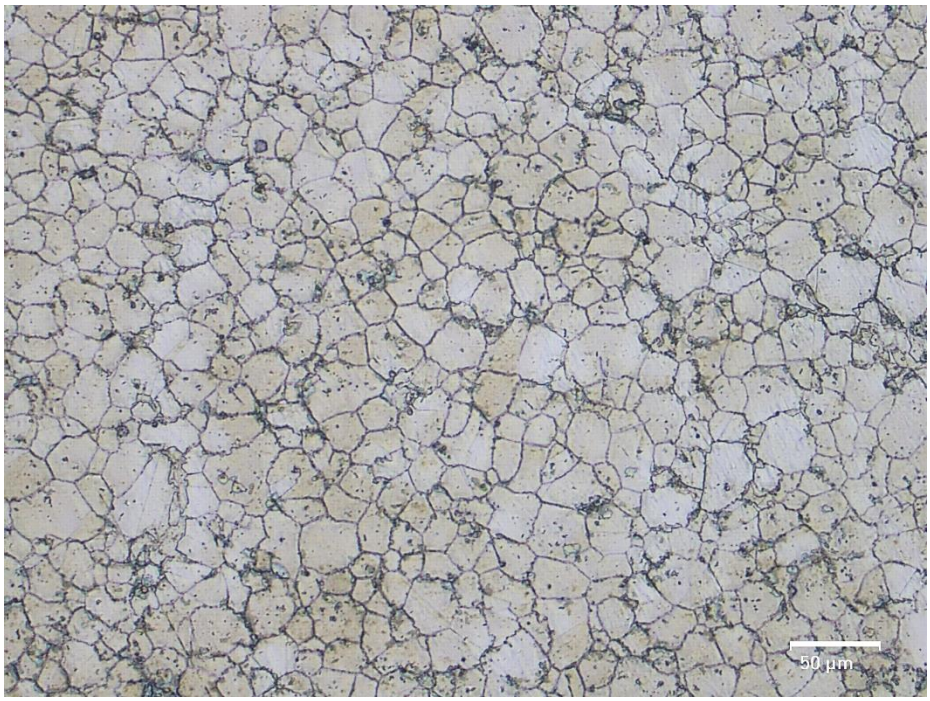

Figure 53. Microstructure of "A" Heat Treated 36NiCrTiAl

It can be inferred from Figure 53 that "A" heat treated 36NiCrTiAl has average grain size of 23.7 µm with Ni_3Ti as γ′ phase in the vicinity and boundaries of grains.

Table 13. Average Grain Size of "A" Heat Treated Materials

Materials	*Average Grain Size(µm)*	*StDev*
Ni-Span C902	9.0	3.0
42NiCrTiAl	26.3	8.1
44NiCrTiAl	135.3	41.5
36NiCrTiAl	23.7	5.5

4.4 Material Characterization of "Q+" Heat Treatment Process

4.4.1 Hardness Testing

"Q+" heat treatment recipe is 30 seconds at 970°C and water quenched. Seven hardness measurements were taken for each of the heat-treated materials.

Table 14. "Q+" Heat Treatment Process Hardness Test Results

Materials	*HV 10*	*CoV*
Ni-Span C902	385.0	1.4
42NiCrTiAl	330.0	5.5
44NiCrTiAl	381.8	1.8
36NiCrTiAl	341.0	3.7

4.4.2 Microstructural Analysis

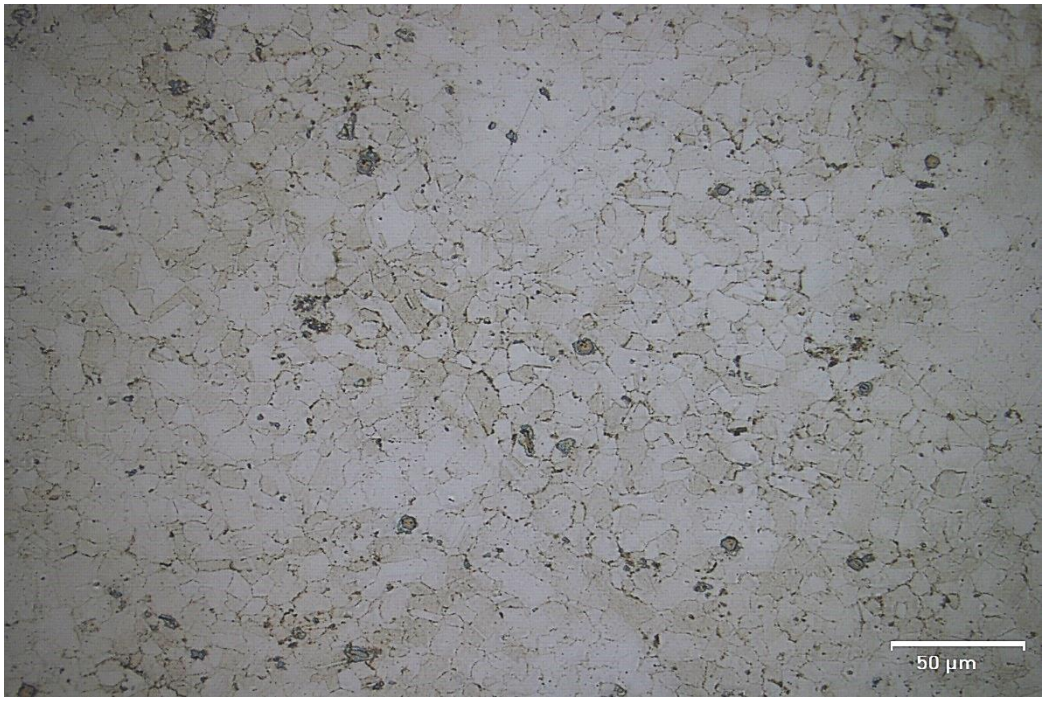

Figure 54. Microstructure of "Q+" Heat Treated Ni-Span C902

It can be inferred from Figure 54 that “Q+” heat treated Ni-Span C902 has average grain size of 9.4 µm with Ni_3Ti as γ′ phase.

Figure 55. Microstructure of “Q+” Heat Treated 42NiCrTiAl

From Figure 55, “Q+” heat treated 42NiCrTiAl has average grain size of 37.2 µm with Ni_3Ti as γ′ phase mostly in the vicinity and junctions of grains. There are also annealing twins.

Figure 56. Microstructure of “Q+” Heat Treated 44NiCrTiAl

From Figure 56, “Q+” heat treated 44NiCrTiAl has average grain size of 88.5 µm with Ni_3Ti as γ′ phase There are also some annealing twins. Although average grain is reduced significantly, grain sizes are not uniform in size. Grain nucleation and growth mechanism worked in the grain boundaries and smaller grains were formed.

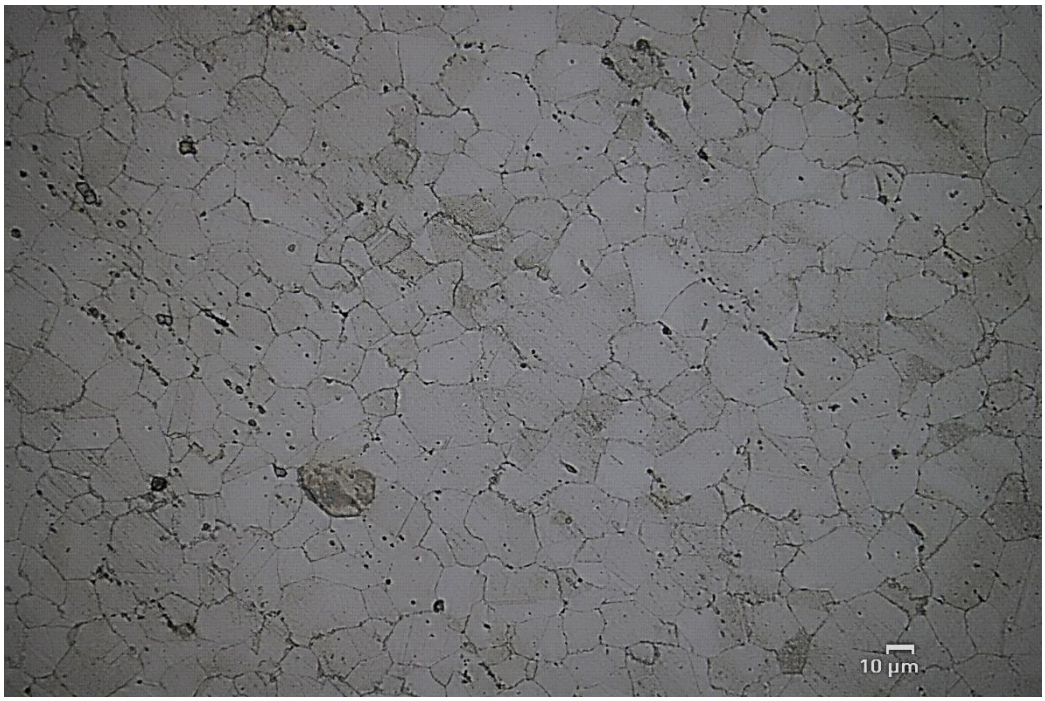

Figure 57. Microstructure of "Q+" Heat Treated 36NiCrTiAl

It can be inferred from Figure 57 that "Q+" heat treated 36NiCrTiAl has average grain size of 17.5 µm with Ni_3Ti as γ′ phase in the vicinity and boundaries of grains.

Table 15. Average Grain Size of "Q+" Heat Treated Materials

Materials	*Average Grain Size(µm)*	*StDev*
Ni-Span C902	9.4	2.2
42NiCrTiAl	37.2	9.5
44NiCrTiAl	88.5	27.0
36NiCrTiAl	17.5	3.8

4.5 Material Characterization of "A+" Heat Treatment Process

4.5.1 Hardness Testing

"A+" heat treatment recipe is 30 seconds at 970°C, water quenched, 2 hours at 650°C and air cooled. Seven hardness measurements were taken for each of the heat-treated materials.

Table 16. "A+" Heat Treatment Process Hardness Test Results

Materials	*HV 10*	*CoV*
Ni-Span C902	403.2	1.7
42NiCrTiAl	375.4	1.6
44NiCrTiAl	404.2	0.9
36NiCrTiAl	411.6	4.7

4.5.2 Microstructural Analysis

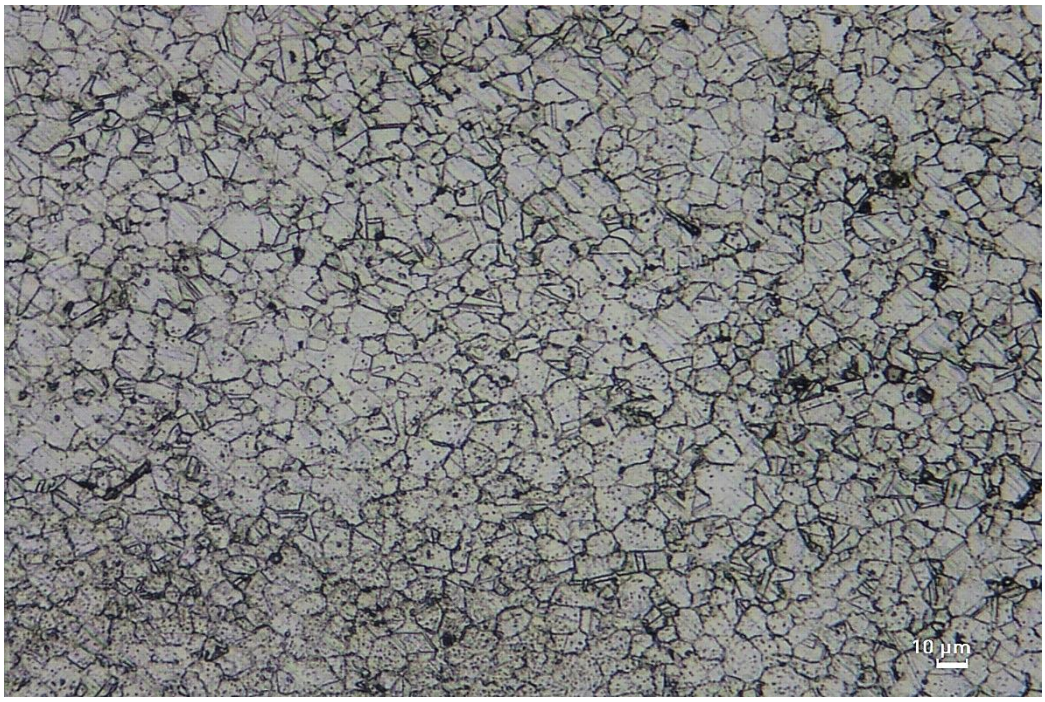

Figure 58. Microstructure of "A+" Heat Treated Ni-Span C902

It can be inferred from Figure 58 that "A+" heat treated Ni-Span C902 has average grain size of 9.3 µm with Ni_3Ti as γ′ phase in the vicinity and boundaries of grains. There are also annealing twins much more than as received condition.

Figure 59. Microstructure of “A+” Heat Treated 42NiCrTiAl

From Figure 59, “A+” heat treated 42NiCrTiAl has average grain size of 23.6 µm with Ni_3Ti as γ' phase mostly in the vicinity of grains. Grain size is reduced approximately 30% from as received condition. There are annealing twins.

Figure 60. Microstructure of “A+” Heat Treated 44NiCrTiAl

From Figure 60, “A+” heat treated 44NiCrTiAl has average grain size of 80.5 µm with Ni_3Ti as γ′ phase. There are also some annealing twins. Although average grain is reduced significantly, grain sizes are not uniform in size. Grain nucleation and growth mechanism worked in the grain boundaries and smaller grains were formed.

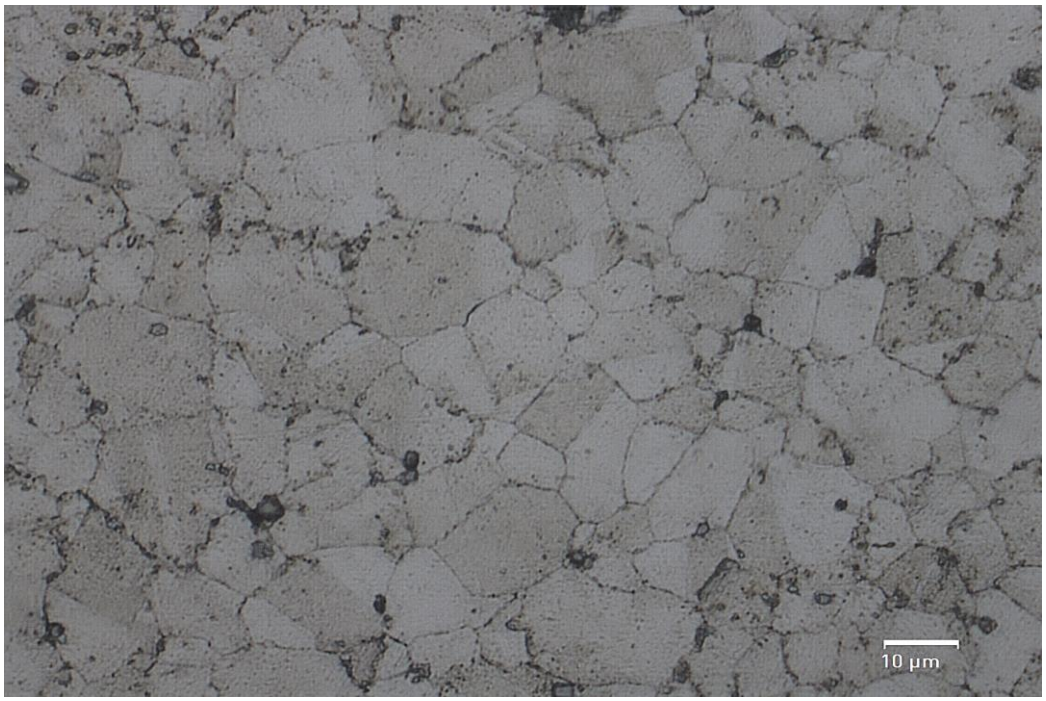

Figure 61. Microstructure of "A+" Heat Treated 36NiCrTiAl

It can be inferred from Figure 61 that "A+" heat treated 36NiCrTiAl has average grain size of 12.3 µm with Ni_3Ti as γ′ phase in the vicinity and boundaries of grains. Average grain size is reduced by 50% compared to as received condition.

Table 17. Average Grain Size of "A+" Heat Treated Materials

Materials	*Average Grain Size(µm)*	*StDev*
Ni-Span C902	9.3	2.9
42NiCrTiAl	23.6	5.5
44NiCrTiAl	80.5	58.0
36NiCrTiAl	12.3	3.7

4.6 Material Characterization of "M" Heat Treatment Process

4.6.1 Hardness Testing

"M" heat treatment recipe is 5 hours at 482°C and air cooled. Seven hardness measurements were taken for each of the heat-treated materials.

Table 18. "M" Heat Treatment Process Hardness Test Results

Materials	*HV 10*	*CoV*
Ni-Span C902	387.6	2.0
42NiCrTiAl	360.0	3.2
44NiCrTiAl	357.6	1.7
36NiCrTiAl	363.0	0.8

4.6.2 Microstructural Analysis

Figure 62. Microstructure of "M" Heat Treated Ni-Span C902

It can be inferred from Figure 62 that Ni-Span C902 as received condition has average grain size of 9.4 µm with Ni_3Ti as γ′ phase in the vicinity and boundaries of grains. Annealing twins can also be seen.

Figure 63. Microstructure of “M” Heat Treated 42NiCrTiAl

From Figure 63, “M” heat treated 42NiCrTiAl has average grain size of 25.2 µm with Ni_3Ti as γ′ phase mostly in the vicinity of grains. Grain size is reduced approximately 30% from as received condition. There are annealing twins.

Figure 64. Microstructure of “M” Heat Treated 44NiCrTiAl

From Figure 64, “M” heat treated 44NiCrTiAl has average grain size of 12.8 µm with Ni_3Ti as γ′ phase evenly distributed in the vicinity of grains. There are also some annealing twins. Grain sizes are more uniform than as received condition and other heat treatment procedures. Second phase particles look much more bigger than as received condition.

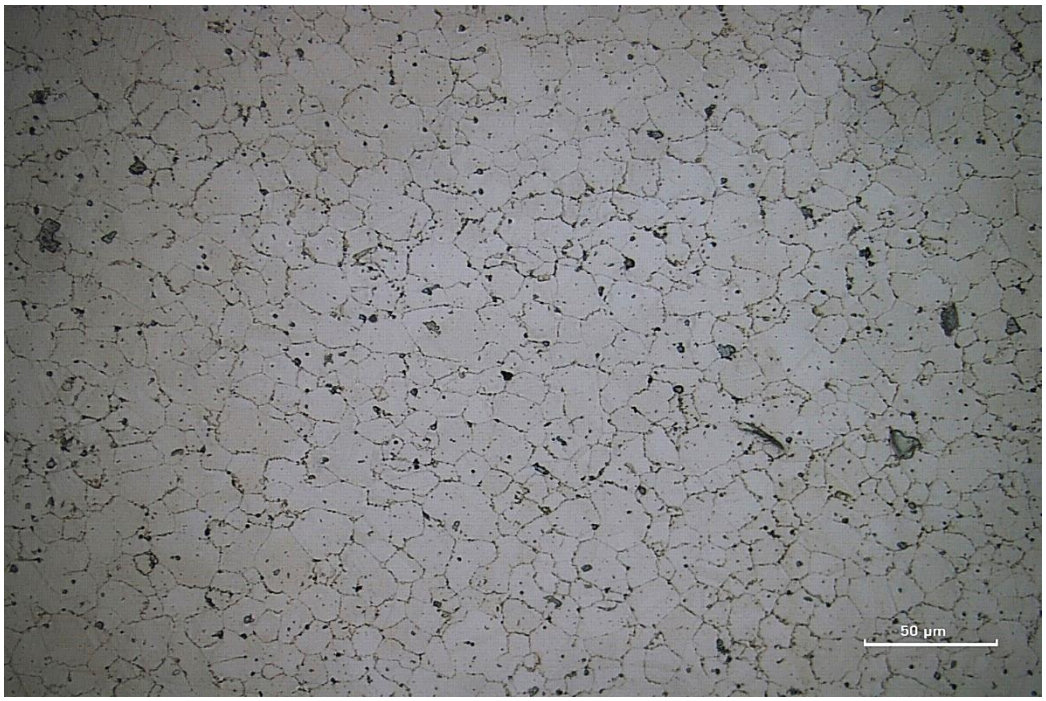

Figure 65. Microstructure of "M" Heat Treated 36NiCrTiAl

It can be inferred from Figure 65 that "M" heat treated 36NiCrTiAl has average grain size of 18.9 µm with Ni_3Ti as γ′ phase in the vicinity and boundaries of grains.

Table 19. Average Grain Size of "M" Heat Treated Materials

Materials	*Average Grain Size(µm)*	*StDev*
Ni-Span C902	9.4	2.5
42NiCrTiAl	25.2	5.8
44NiCrTiAl	12.9	3.4
36NiCrTiAl	18.9	5.1

4.7 Material Characterization of "S" Heat Treatment Process

4.7.1 Hardness Testing

"S" heat treatment recipe is 30 seconds at 910°C (heating rate of 10°C/min) and air cooled. Seven hardness measurements were taken for each of the heat-treated materials.

Table 20. "S" Heat Treatment Process Hardness Test Results

Materials	*HV 10*	*CoV*
Ni-Span C902	309.4	2.4
42NiCrTiAl	223.5	2.5
44NiCrTiAl	225.0	4.0
36NiCrTiAl	266.2	4.0

4.7.2 Microstructural Analysis

Figure 66. Microstructure of "S" Heat Treated Ni-Span C902

It can be inferred from Figure 66 that "S" heat treated Ni-Span C902 has average grain size of 9.4 µm with Ni_3Ti as γ′ phase in the vicinity and boundaries of grains. There are some annealing twin formations.

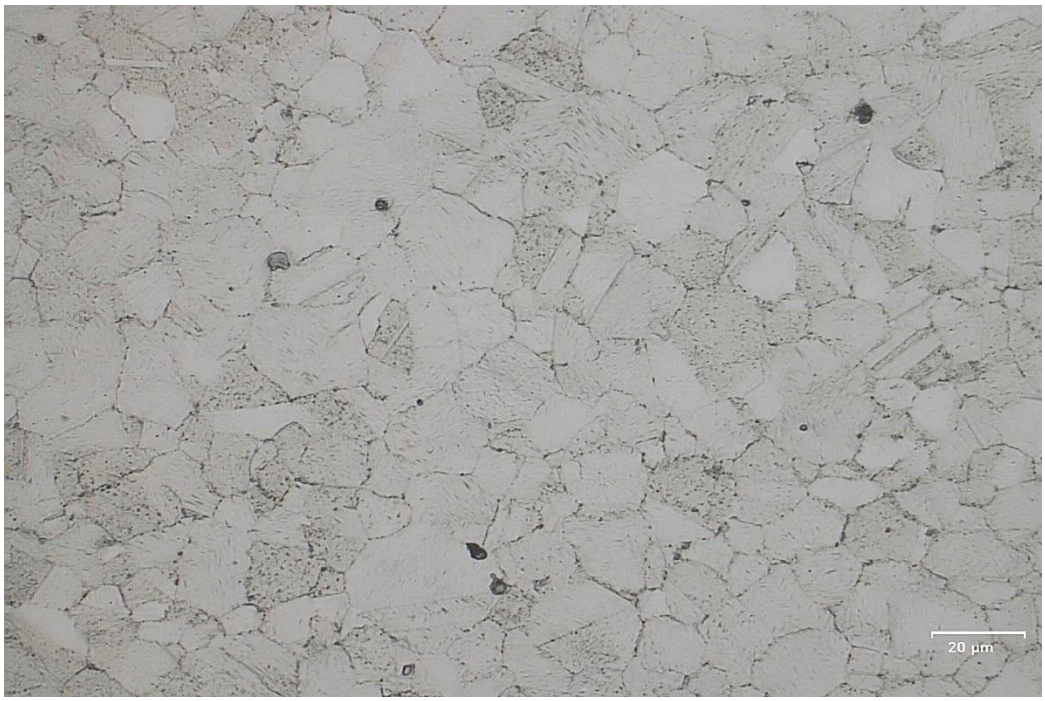

Figure 67. Microstructure of “S” Heat Treated 42NiCrTiAl

From Figure 67, “S” heat treated 42NiCrTiAl has average grain size of 16.0 µm with Ni_3Ti as γ′ phase mostly in the vicinity of grains. There are also some annealing twins. Grain size is reduced by more than 50% compared to as received condition. Orientation difference can also be seen between grains.

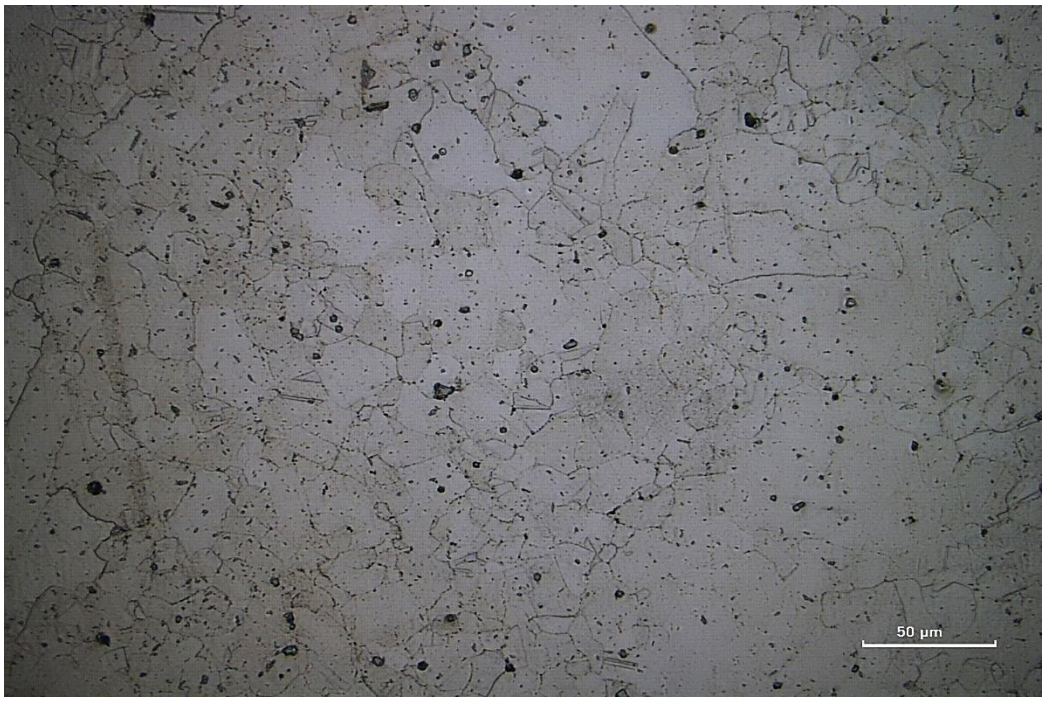

Figure 68. Microstructure of “S” Heat Treated 44NiCrTiAl

From Figure 68, “S” heat treated 44NiCrTiAl has average grain size of 17.8 µm with Ni_3Ti as γ′ phase evenly distributed in the vicinity of grains. There are also some annealing twins. Most of the second phase particles are bigger than as received condition. Average grain size value is decreased from 137.7 µm to 17.8 µm

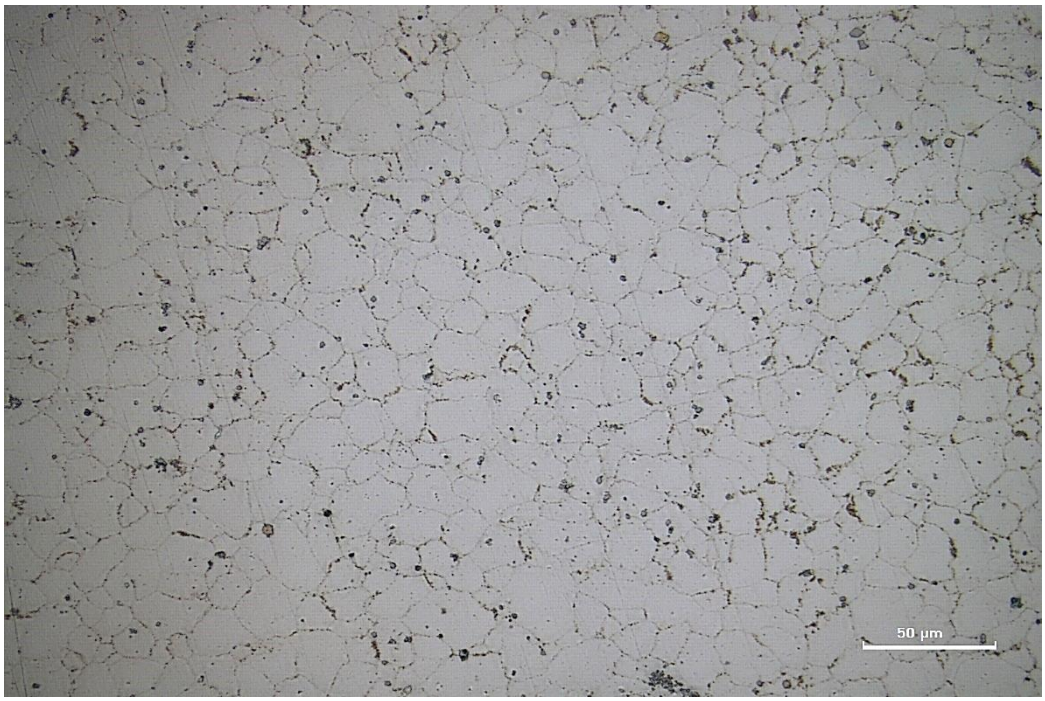

Figure 69. Microstructure of “S” Heat Treated 36NiCrTiAl

It can be inferred from Figure 69 that “S” heat treated 36NiCrTiAl has average grain size of 16.8 µm with Ni_3Ti as γ′ phase in the vicinity and mostly in boundaries of grains.

Table 21. Average Grain Size of “S” Heat Treated Materials

Materials	*Average Grain Size(µm)*	*StDev*
Ni-Span C902	9.2	2.9
42NiCrTiAl	16.0	3.5
44NiCrTiAl	17.8	7.5
36NiCrTiAl	16.8	4.5

4.8 Material Characterization of "M+" Heat Treatment Process

4.8.1 Hardness Testing

"M+" heat treatment recipe is 5 hours at 730°C and air cooled. Seven hardness measurements were taken for each of the heat-treated materials.

Table 22. "M+" Heat Treatment Process Hardness Test Results

Materials	*HV 10*	*CoV*
Ni-Span C902	406.1	1.7
42NiCrTiAl	381.7	1.2
44NiCrTiAl	389.4	1.3
36NiCrTiAl	386.6	1.3

4.8.2 Microstructural Analysis

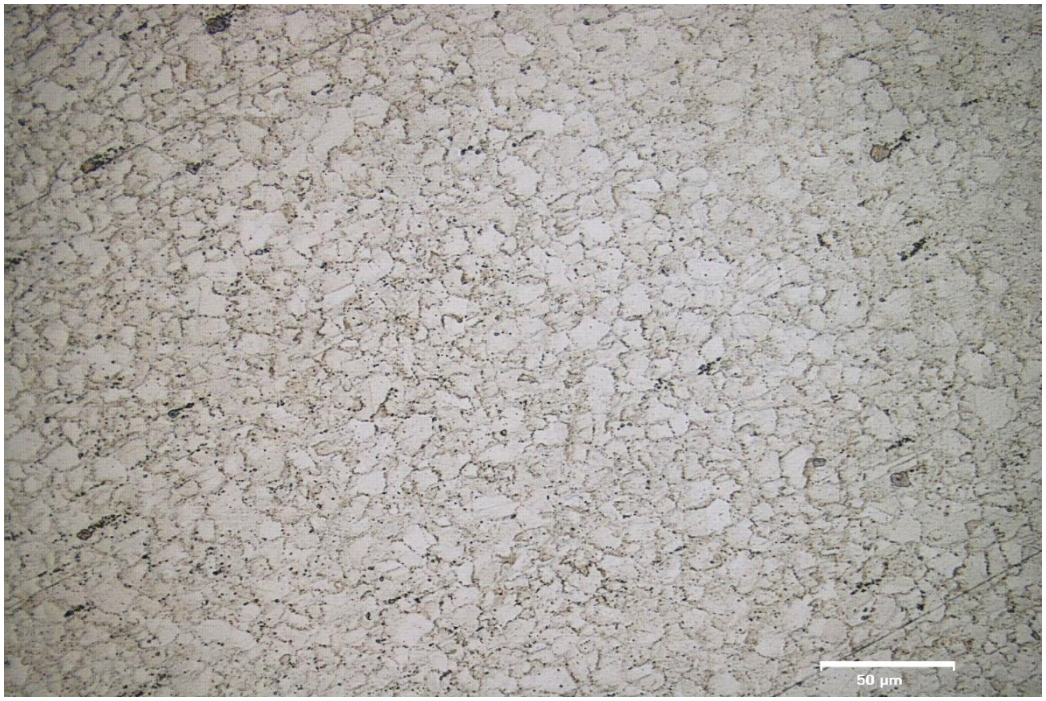

Figure 70. Microstructure of "M+" Heat Treated Ni-Span C902

It can be inferred from Figure 70 that “M+” heat treated Ni-Span C902 has average grain size of 9.7 µm with Ni_3Ti as γ′ phase in the vicinity and boundaries of grains.

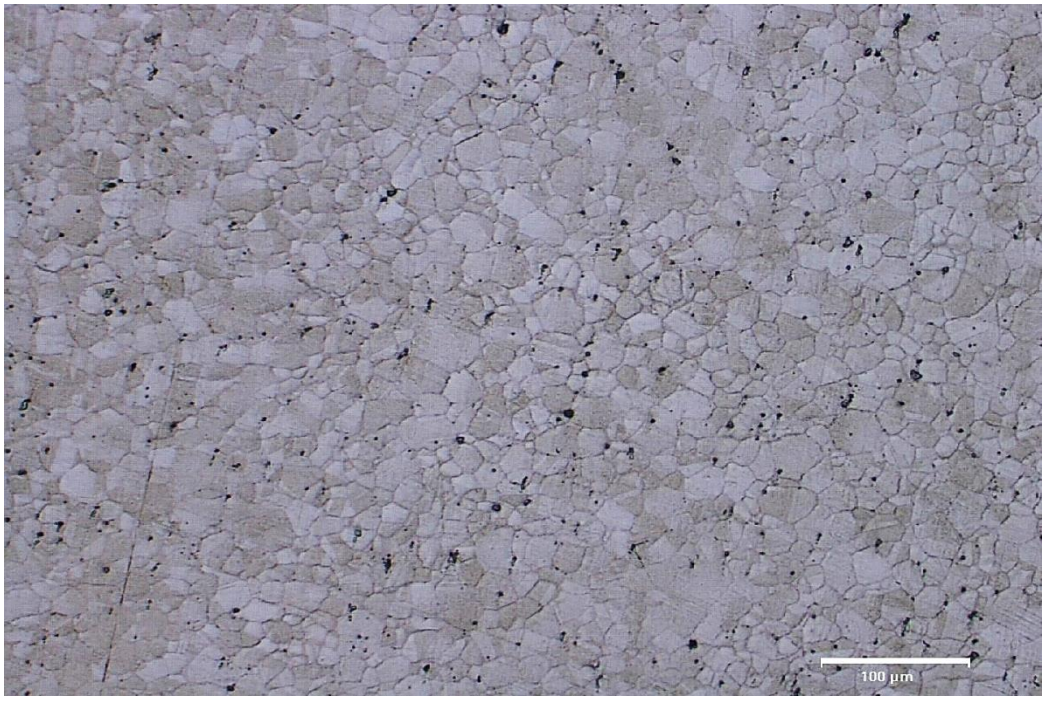

Figure 71. Microstructure of “M+” Heat Treated 42NiCrTiAl

From Figure 71, “M+” heat treated 42NiCrTiAl has average grain size of 16.0 µm with Ni_3Ti as γ′ phase mostly in the vicinity of grains. Second phase particles look bigger than as received condition. Average grain size is reduced by more than 50% compared to as received condition.

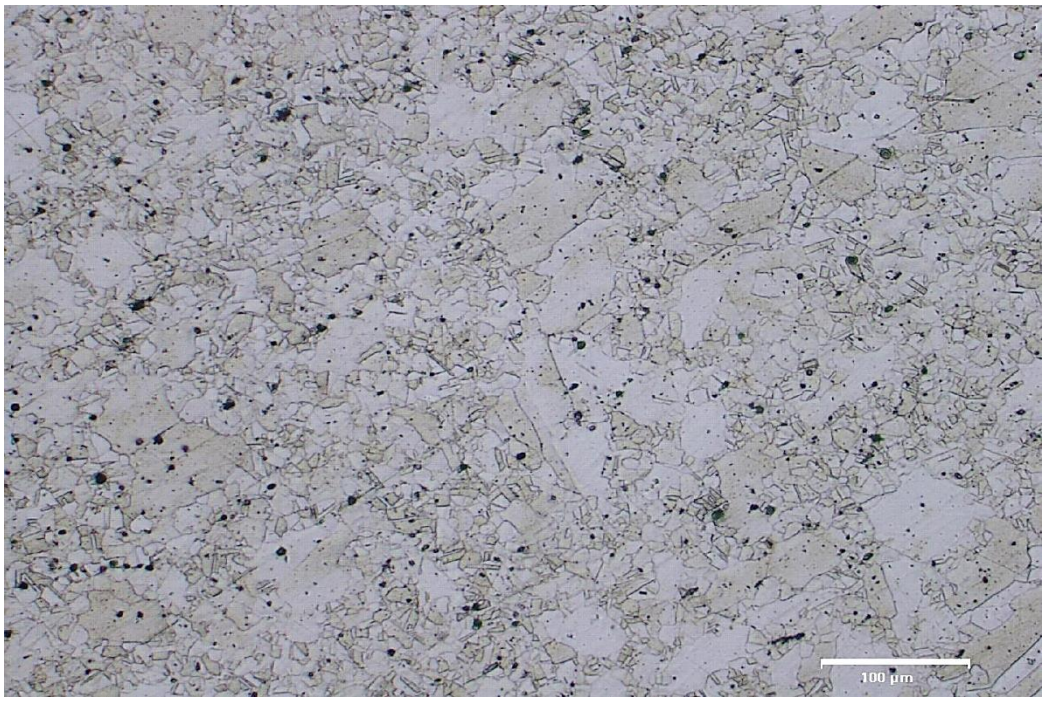

Figure 72. Microstructure of “M+” Heat Treated 44NiCrTiAl

From Figure 72, “M+” heat treated 44NiCrTiAl average grain size of 11.5 µm with Ni_3Ti as γ′ phase evenly distributed in the vicinity of grains. Second phase particles are much bigger than as received condition. There are also some annealing twins. Grain sizes are not uniform in size. Average grain size is the lowest amongst all heat treatment procedures.

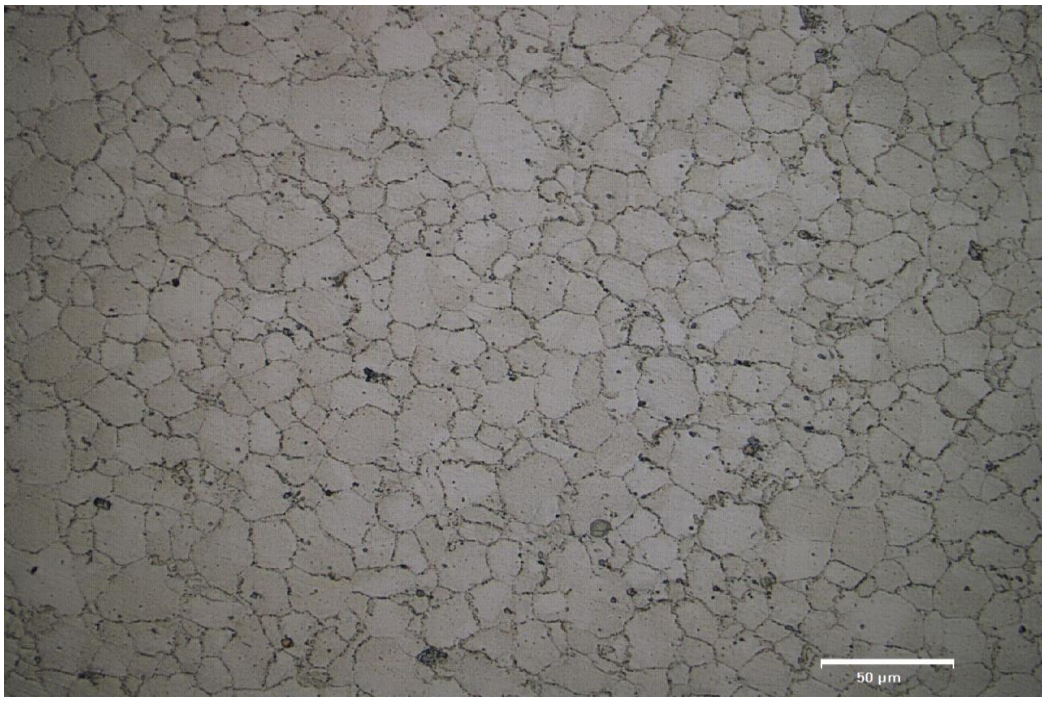

Figure 73. Microstructure of “M+” Heat Treated 36NiCrTiAl

It can be inferred from Figure 73 that “M+” heat treated 36NiCrTiAl has average grain size of 18.0 µm with Ni_3Ti as γ′ phase in the vicinity and mostly in boundaries of grains.

Table 23. Average Grain Size of “M+” Heat Treated Materials

Materials	*Average Grain Size(µm)*	*StDev*
Ni-Span C902	9.7	2.3
42NiCrTiAl	16.0	4.0
44NiCrTiAl	11.5	5.3
36NiCrTiAl	18.0	3.4

4.9 Heat Treatment Process Selection

4.9.1 Results Comparison

Table 24. Summary Table for Hardness Values

No.	Materials	*As Received*	*Q*	*A*	*Q+*	*A+*	*M*	*S*	*M+*
1	Ni-Span C902	365.7	239.8	378.0	385.0	403.2	387.6	309.4	406.1
2	42NiCrTiAl	377.2	171.0	319.8	330.0	375.4	360.0	223.5	381.7
3	44NiCrTiAl	326.2	218.4	329.0	381.8	404.2	357.6	225.0	389.4
4	36NiCrTiAl	326.7	302.7	390.4	341.0	411.6	363.0	266.2	386.6

Table 25. Summary Table for Grainsize (µm)

No.	Materials	*As Received*	*Q*	*A*	*Q+*	*A+*	*M*	*S*	*M+*
1	Ni-Span C902	8.5	9.0	9.0	9.4	9.3	9.4	9.2	9.7
2	42NiCrTiAl	35.1	34.4	26.3	37.2	23.6	25.2	16.0	16.0
3	44NiCrTiAl	137.7	132.2	135.3	88.5	80.5	12.9	17.8	11.5
4	36NiCrTiAl	24.5	24.4	23.7	17.5	12.3	18.9	16.8	18.0

4.9.2 Selection

It is seen in Table 24 and Table 25 that highest amount of change in both hardness and grain size is A+ and M+ heat treatment processes. All four of the materials respond these heat treatments and their responds are different in terms of microstructure as it can be seen in Figure 58, Figure 59, Figure 60, Figure 61, Figure 70, Figure 71, Figure 72 and Figure 73. Also, A+ heat treatment process is similar that of Sukhovarov et al.(1984) [57]. This literature data was the beginning point of heat treatment trials. M, S and M+ heat treatment process is carried out with the help of thermo-calc analysis shown in Figure 38, Figure 39, Figure 40 and

Figure 41. Hardness and grain size values were changed most in the M+ heat treatment process. In order to explain the vibration transition through samples in the most perceptible way A+ and M+ heat treatment processes were selected. After this selection, Figure 37Figure 37. Flowchart Experimental Procedure was followed.

4.10 Tensile Testing

Table 26. "A+" Heat Treatment Process Tensile Test Results

Materials	*Maximum Load (kN)*	*Tensile Stress (MPa)*	*Yield Stress (Offset 0.2 %) (MPa)*	*Tensile Strain (%)*	*Modulus (E-modulus) (MPa)*
Ni-Span C902	39.520	1397.5	1008.0	24.7	172000
42NiCrTiAl	36.990	1308.0	887.0	22.1	164500
44NiCrTiAl	37.625	1331.0	1011.0	14.4	162000
36NiCrTiAl	37.530	1327.5	887.0	24.5	180000

Table 27. "M+" Heat Treatment Process Tensile Test Results

Materials	*Maximum Load (kN)*	*Tensile Stress (MPa)*	*Yield Stress (Offset 0.2 %) (MPa)*	*Tensile Strain (%)*	*Modulus (E-modulus) (MPa)*
Ni-Span C902	39.035	1380.7	959.0	24.9	237225
42NiCrTiAl	36.690	1297.8	901.0	23.1	206853
44NiCrTiAl	37.430	1324.0	919.0	13.8	126067
36NiCrTiAl	37.260	1317.8	915.0	27.0	245514

4.11 Q-Factor Testing

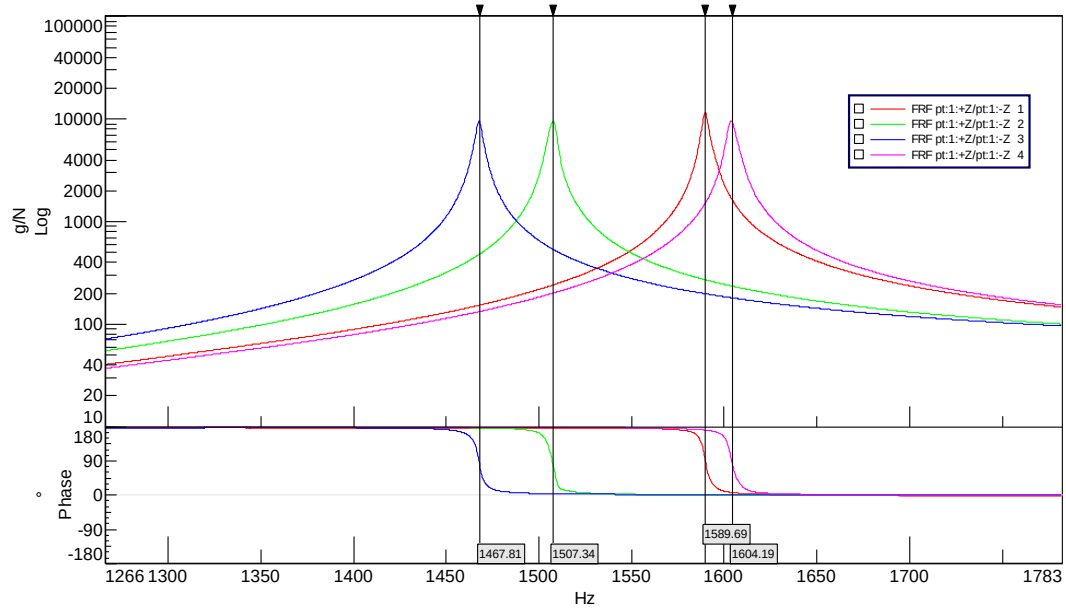

Figure 74. Q-factor Test Result of All Material as Received Condition

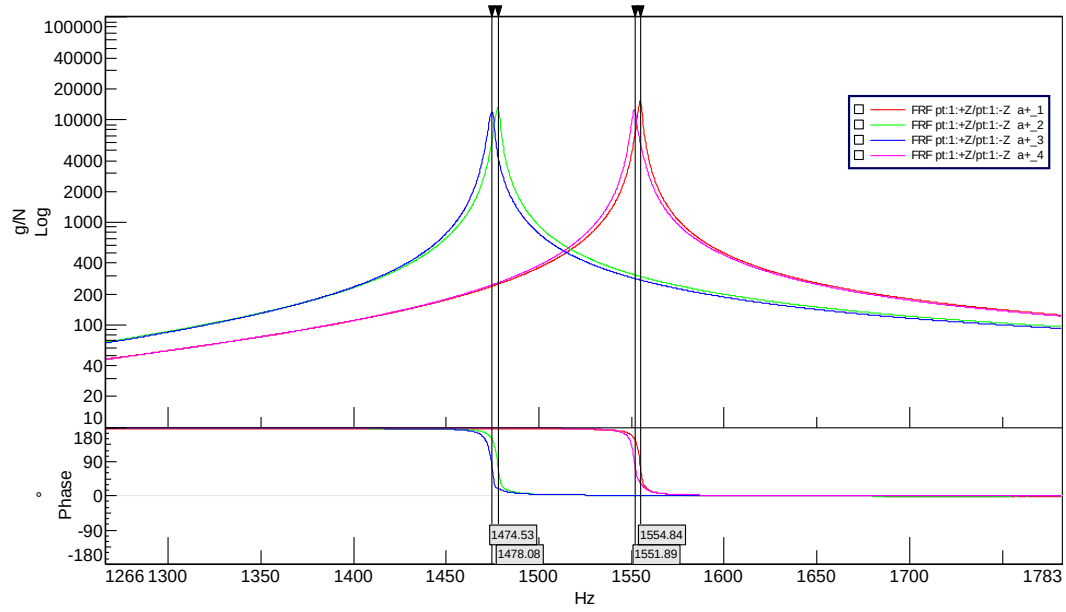

Figure 75. Q-factor Test Results of All Material A+ Heat Treated

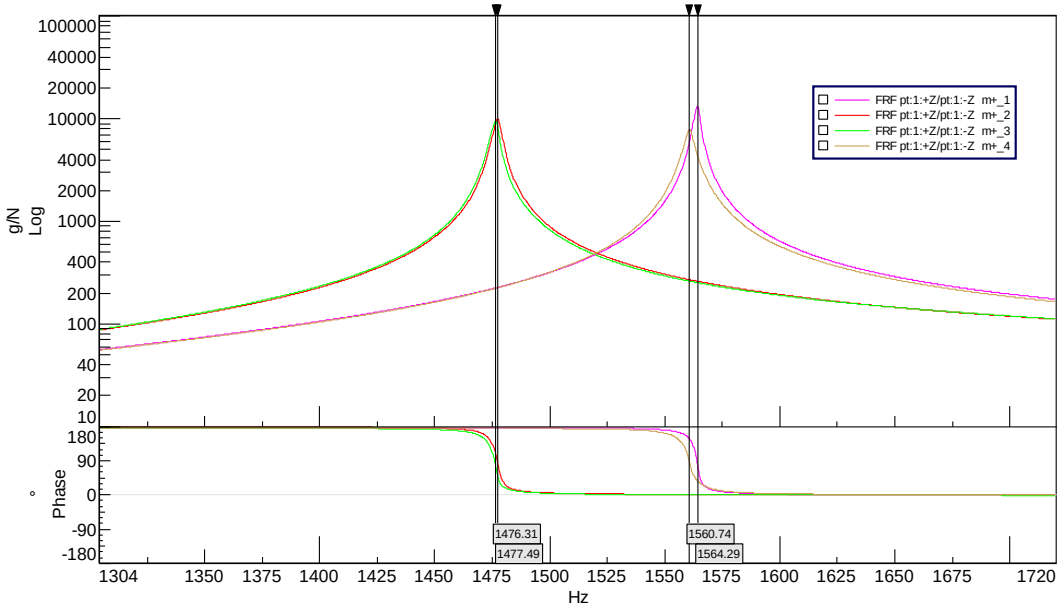

Figure 76. Q-factor Test Results of All Material M+ Heat Treated

Table 28. Q-factor Test Results

Materials	*Ni-Span C902*	*42NiCrTiAl*	*44NiCrTiAl*	*36NiCrTiAl*
As Received	437	321	310	332
A+	580	484	461	500
M+	529	363	328	372

The values in Table 28 are calculated from Figure 74, Figure 75 and Figure 76 using half-power bandwidth method explained in section 2.7.5.

4.12 Summary of Results and Discussion

As it can be seen from below Figure 77 that the highest amount of change in hardness is A+ and M+ heat treatments. According to [58], “During hardening, excess phases dissolve in austenite and during aging, strengthening dispersed phases precipitate from the solid solution” and according to [59], Q-factor strongly depends on the solid solution. The condition of it directly affects the Q-factor. This

is the reason that all four of the Q-factor samples are subjected to these two heat treatment procedures.

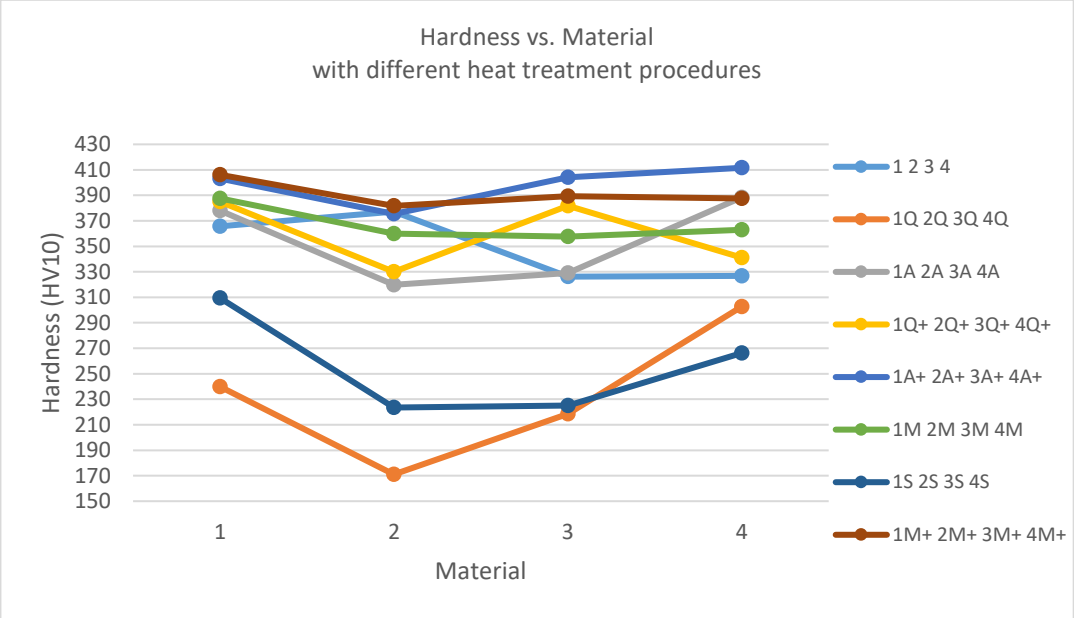

Figure 77. Hardness vs. Materials Graph with Different Heat Treatment Procedures

A+ heat treatment is holding 30 seconds at 970°C, quenching to 12°C water, 2 hours at 650°C and air cooled. A+ heat treatment procedure amongst M+ and as received condition is the only one includes quenching. According to [59], quenching may create vacancies in Fe-Ni superalloys and vacancies concentration increases with increasing cooling rate. As Granato-Lucke theory [42] explains that vacancies pin dislocations and reduce the average length of dislocations, and consequentially increase the Q-factor. It is also mentioned in section 2.5 that dislocation density and mean length of dislocations between the weak pinning points affect the Q-factor. These weak pinning points consist of soluble atoms or vacancies surrounding dislocations. Dislocation movements are the major internal friction mechanism [11].

According to Hu et al. [11]:

Equation 23: $\boldsymbol{Q^{-1} \sim \rho l^4}$

ρ: dislocation density

l: mean length of dislocation

Above mentioned literatures substantiate the results of this study. Vacancy creation due to quenching may reduce dislocation length and this reduction may increase the Q-factor A+ heat treated samples. Although, this mechanism may be the primary one increasing Q-factor. There should be an optimum value of vacancy concentration. Since, according to [60], impurity atoms, excess phases and other discontinuities increases the internal friction and increase in internal friction results in decrease in the Q-factor. In order to increase the Q-factor homogenous microstructure is desired.

Q-factor test results of M+ heat treated samples are lower in all materials Ni-Span C902, 42NiCrTiAl, 44NiCrTiAl and 36NiCrTiAl. Although, their production methods, nickel, chromium, titanium and aluminum compositions are different all of them displays the same almost similar fall. Because aging at elevated temperature "increasing the length of phase boundaries and disrupting the coherence between the precipitating phase and the matrix led to large inelastic deformation during vibrations" [59]. As a result of this effect, Q-factor of materials decreases.

Watanabe, Mukai, Sugioka and Ishikawa, 2004 [12] mentioned that Q-factor or damping or internal friction depend on the microstructural factor such as orientation and grain size and the effect of the factors has not been discoursed detailly. In this thesis study, we wanted to check if there is a relationship between grain size and Q-factor. In order to investigate on this relation, it is necessary to measure grain sizes of each heat treatment procedures. Below Figure 78, Figure 79, Figure 80 and Figure 82, grain size vs heat treatment procedure graphs of each material is displayed. Since Q-factor tests were carried out to A+ and M+ heat treated material, it is mainly focused of grain size measurements of these heat treatment procedures.

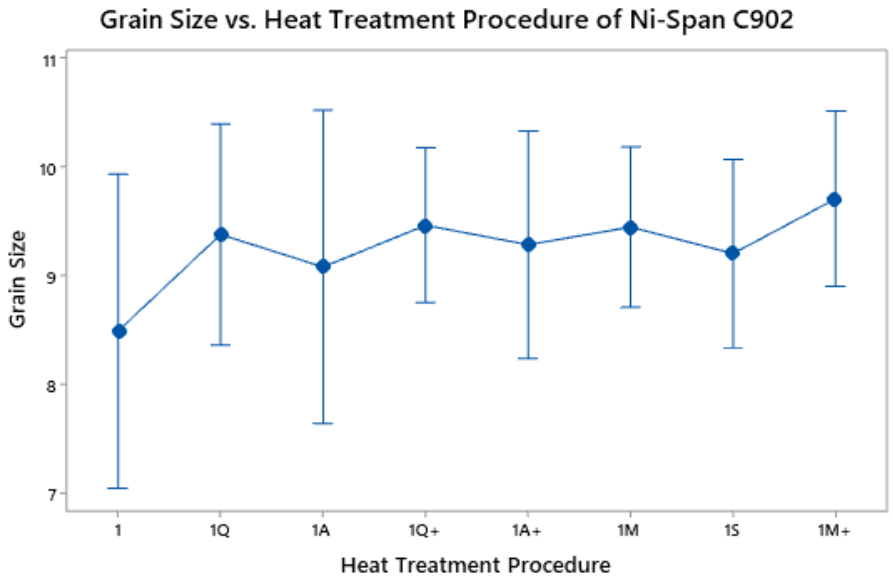

Figure 78. Grain size (µm) vs. Heat Treatment Procedure of Ni-Span C902

As it can be seen from Figure 78, Ni-Span C902 does not have statistically significant change in grain size with different heat treatment procedures. Since grain size is small, it is hard to understand the difference between heat treatment procedures.

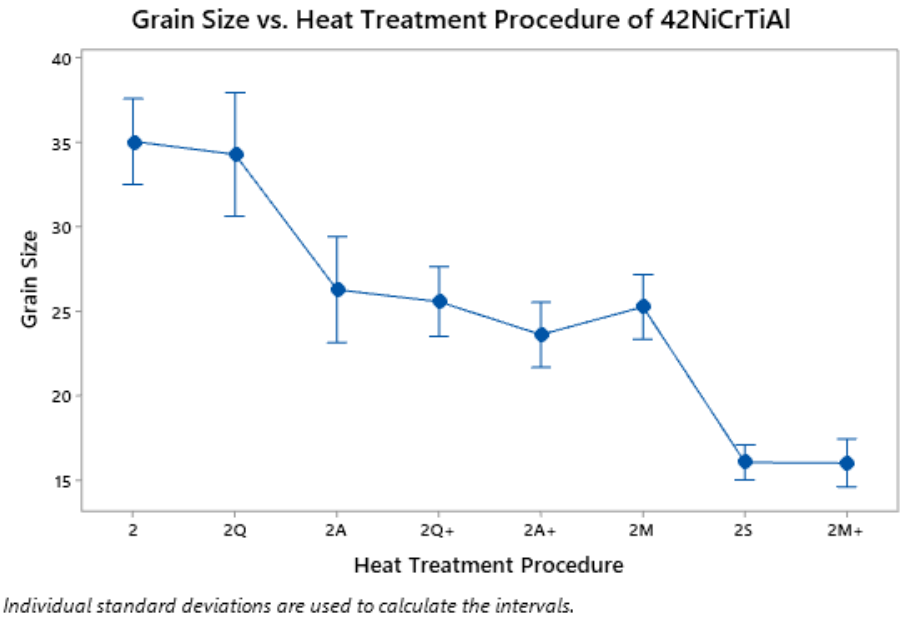

Figure 79. Grain size (µm) vs. Heat Treatment Procedure of 42NiCrTiAl

Figure 79 shows that 42NiCrTiAl alloys respond the A+ and M+ heat treatments differently. A+ heat treated sample has bigger grain size than M+ one. Solution treatment at 970 °C at 6 minutes resulted in grain growth and giving less amount time at γ′ region of phase diagram (shown in Figure 38, Figure 39, Figure 40 and Figure 41) reduces nucleation sites due to recovery during solution treatment. It is the same for the 44NiCrTiAl as shown in Figure 80. Although, grain sizes of 44NiCrTiAl superalloy are bigger than that of 42NiCrTiAl since 44NiCrTiAl is produced as cast, at M+ heat treatment procedure grain size of 44NiCrTiAl is below 20 µm.

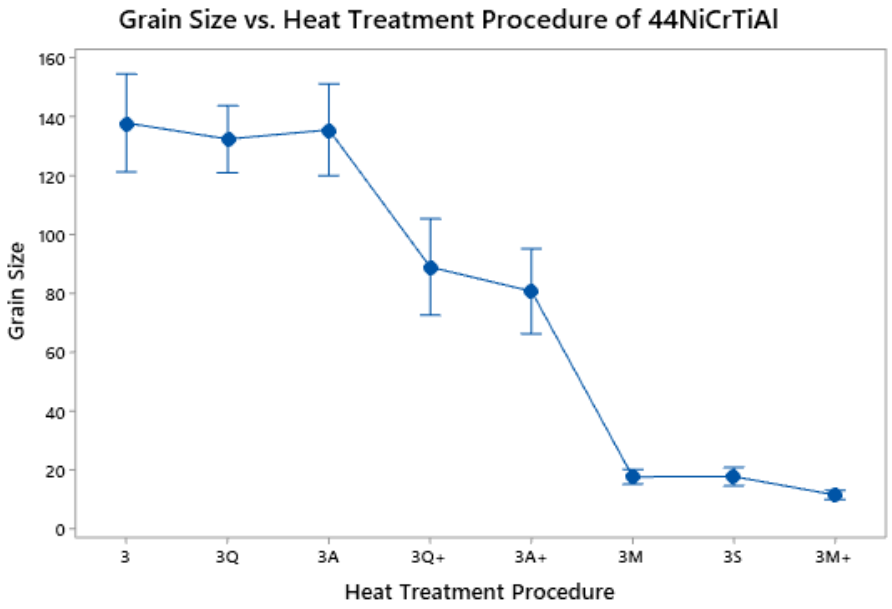

Figure 80. Grain size (µm) vs. Heat Treatment Procedure of 44NiCrTiAl

36NiCrTiAl superalloys respond opposite to those of 42NiCrTiAl and 44NiCrTiAl. A+ heat treated samples' grain size is the smallest of all the heat treatment procedures. As it is given at section 4.1.1, Cr content of 36NiCrTiAl is 12.6%; however, 42NiCrTiAl and 44NiCrTiAl have 4.9% and 4.8%. Cr. The solution treatment dissolves all phases except carbides such as $Cr_{23}C_6$. γ′ precipitates begin nucleation during cooling and those carbides tend to form at grain boundaries and act as nucleation sites. With increasing solution treatment temperature and time, grain size of 36NiCrTiAl will be getting smaller to a certain degree. Below Figure 81 shows a carbide particle and its EDS analysis of 36NiCrTiAl superalloy. In SEM image, it is also possible to investigate the coherency between grains and cuboidal γ′ precipitates which are Ni_3Ti phases. The geometry of γ′ changes with aluminium/titanium ratio. [33]

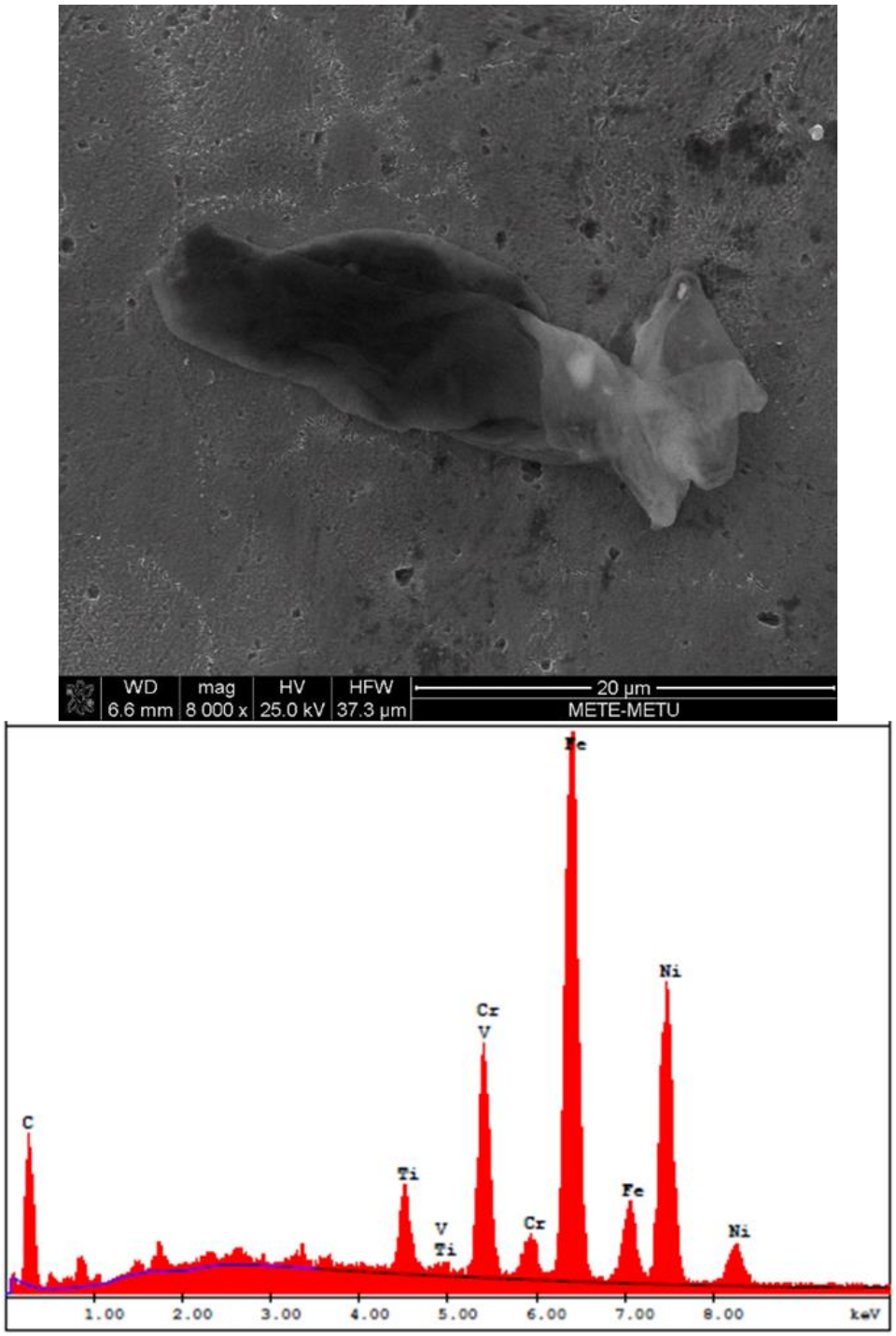

Figure 81. SEM Image and EDS Analysis of Carbide Particle

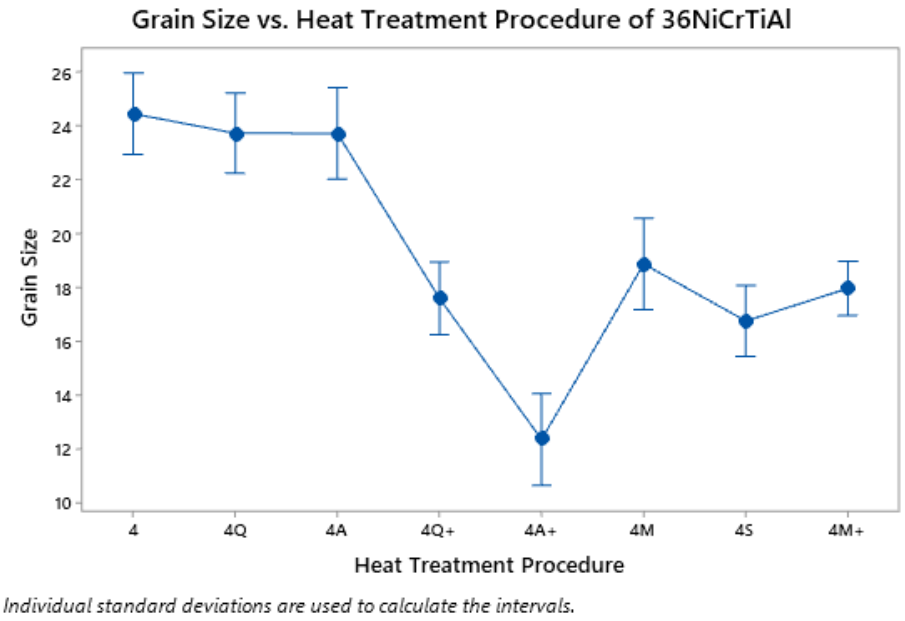

Figure 82. Grain size (µm) vs. Heat Treatment Procedure of 36NiCrTiAl

Q and S heat treatment processes show minimum hardness values for all materials because these heat treatment procedures have only solution treatment and have not been followed by subsequent precipitation or aging process. Solution treatment process dissolves nearly or all of second phases in fcc matrix and recrystallize.

M+ and A+ heat treatment processes show maximum hardness values for all materials because these heat treatment procedures have precipitation or aging process. M+ heat treatment has only aging process; however, A+ heat treatment process has solution treatment and then followed by subsequent precipitation or aging process. According to [32], "Precipitation treatments strengthen age-hardenable alloys by causing the precipitation of one or more phases (γ′ and γ″) from the supersaturated matrix that is developed by solution treating and retained by rapid cooling from the solution treating temperature."

Aging process temperature and time determines type, number and size of precipitates. By optimizing these parameters, desired strength and ductility values to the extent permitted by the limit of alloy.

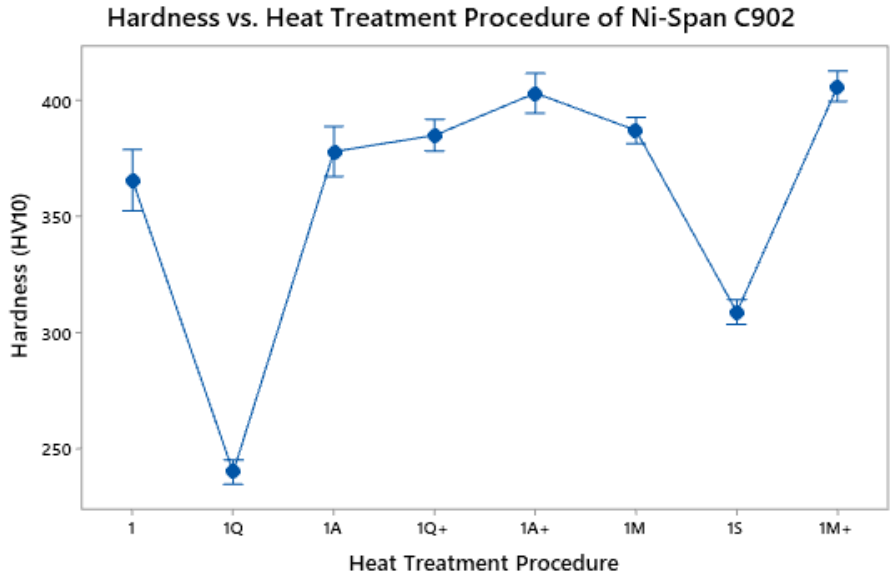

Figure 83. Hardness (HV10) vs. Heat Treatment Procedure of Ni-Span C902

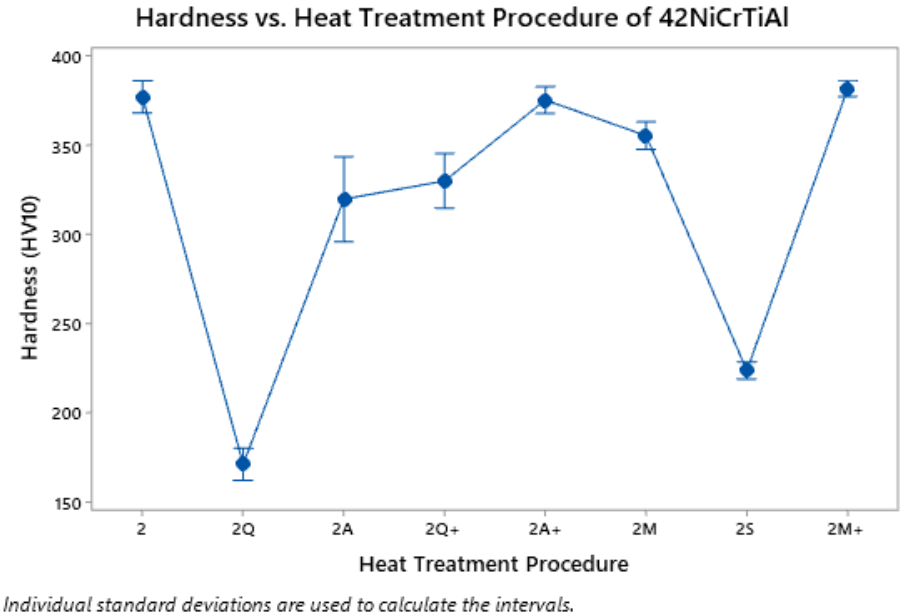

Figure 84. Hardness (HV10) vs. Heat Treatment Procedure of 42NiCrTiAl

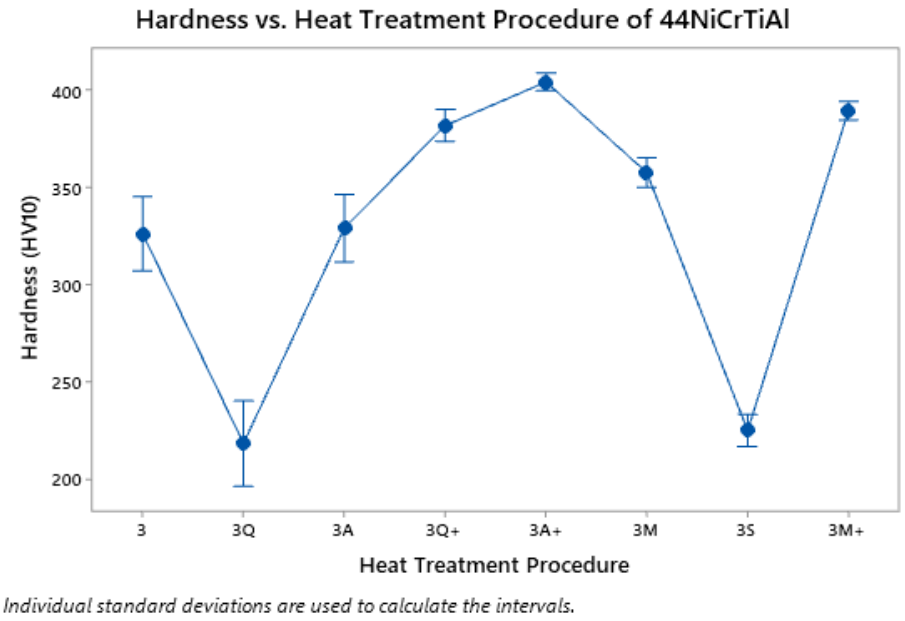

Figure 85. Hardness (HV10) vs. Heat Treatment Procedure of 44NiCrTiAl

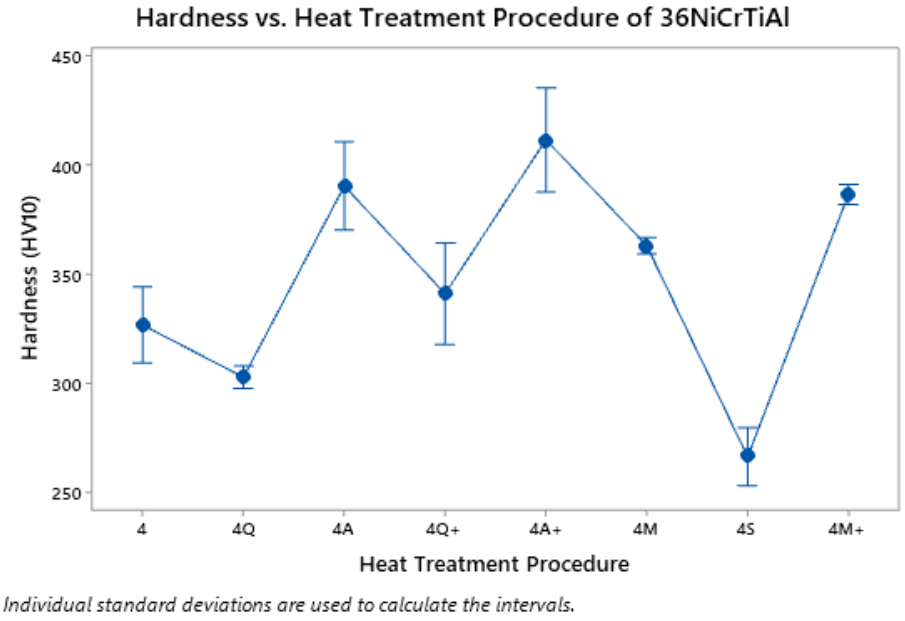

Figure 86. Hardness (HV10) vs. Heat Treatment Procedure of 36NiCrTiAl

When hardness and grain size values are compared, there is no direct relationship between them. Statistical analysis of this comparison was made by using Minitab software for each of the material and heat treatment procedure and statistically

there is no significant relationship between hardness and grain size values. Consequently therefore, different strengthening mechanisms acted rather than grain boundary strengthening mechanism.

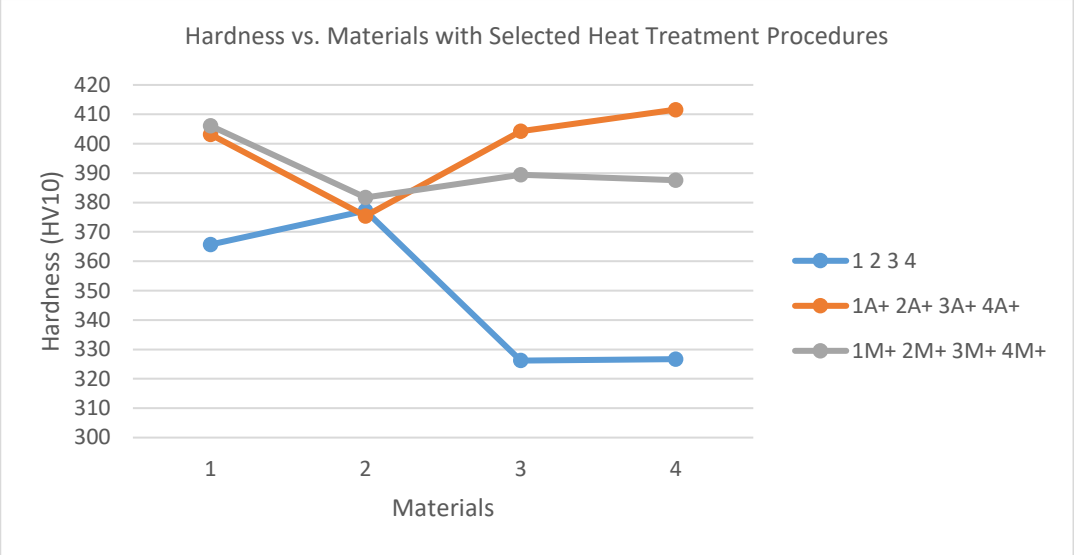

Figure 87. Hardness vs. Materials with Selected Heat Treatment Procedures

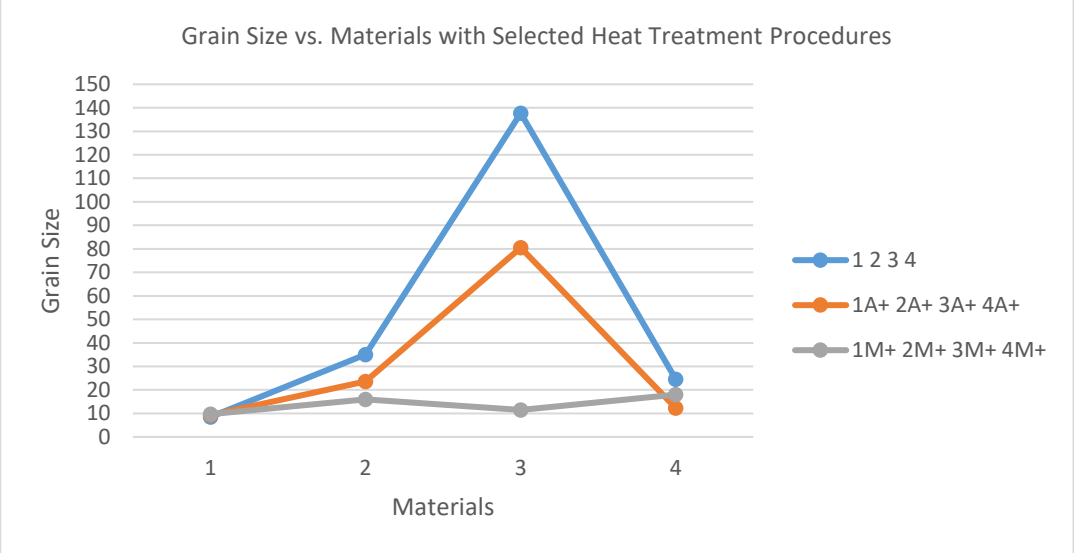

Figure 88. Grain Size (µm) vs. Materials with Selected Heat Treatment Procedures

From Figure 87 and Figure 88, every material responds differently to different heat treatment procedures. The primary reason for this difference is compositional difference and secondary reason is their production technique. This finding is similar to that observed by Shlyakhova *et al.*,2021 [58]. According to findings of Ridhwan *et al.* 2013 [61], "It can be seen that the grain coarsening characteristic did not reflect the unique increases in the hardness behavior, so the effect of carbide content of aged samples was analyzed." After this study, [61] found that at lower temperatures carbides were coarser and it did not increase hardness, but at elevated temperatures carbides were finer and distributed to matrix which increases the hardness. In this study carbides are present more in Ni-Span C902 and 36NiCrTiAl than 42NiCriTiAl and 44NiCriTiAl. As it can be seen from Figure 87, 1. and 4. materials' hardness values increased, and grain size values did not change as much as like 2. and 3. materials. This finding is quite similar to that of [61]. A+ and M+ heat treatments help carbides to form and distribute along the matrix. These carbides act as impedition to dislocation motions since dislocation can only continue its movement by shearing or climbing [62]. Therefore, hardness values of 1. and 4. materials were higher. The finding of Messe and Rae, 2016 [63] also support this inference.

A+ and M+ heat treated and as received condition materials are subjected to the Q-factor testing, results shown in Figure 89. A+ heat treated materials have the highest Q-factor among all Q-factor tests. For all the heat treatment procedures and as received condition of materials Q-factor test results are in the same order which is $Q_1 > Q_4 > Q_2 > Q_3$.

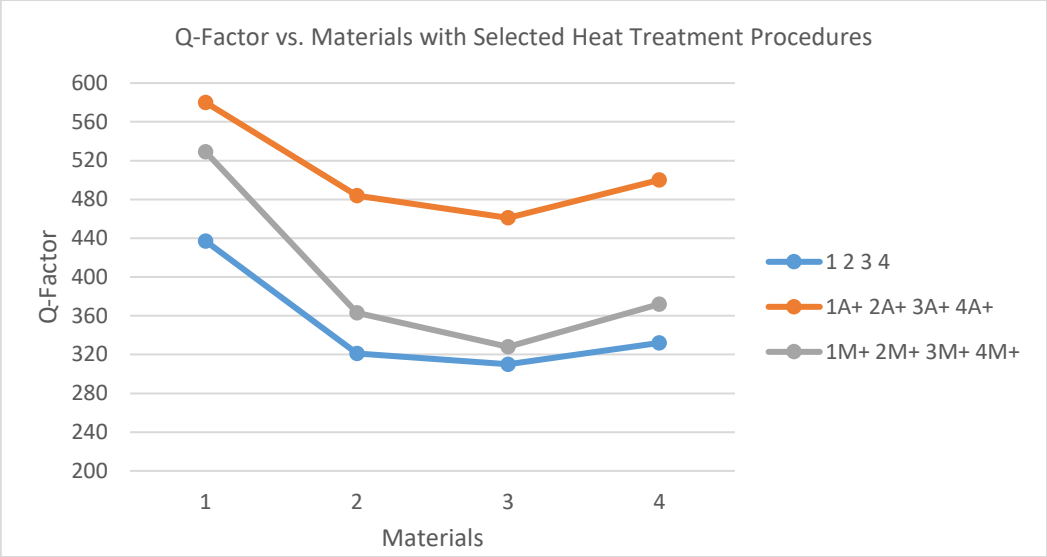

Figure 89. Q-Factor vs. Materials Graph with Selected Heat Treatment Procedures

Since according to Hu et al. [11]: $\boldsymbol{Q^{-1} \sim \rho l^4}$, it is necessary to statistically examine whether Q-factor depends on hardness, grain size, tensile strength and yield strength. Using Minitab software, multiple regression analysis was carried out and p-values, R-sq and correlation were calculated in below Table 29. P-values are below 0.05 for hardness and tensile strength which means there is a statistically significant correlation between Q factor and, hardness and tensile strength.

Table 29. Regression for Q-factor and Hardness, Grain size, Tensile Strength, Yield Strength, Elongation and Modulus

Property	*P-value*	*R-sq*	*Correlation*
Hardness	0.019	43.66	0.66
Grain size	0.242	13.42	-0.37
Tensile Strength	<0.001	69.36	0.83
Yield Strength	0.052	32.72	0.57
Elongation	0.349	8.81	0.30
Modulus	0.970	0.01	-0.01

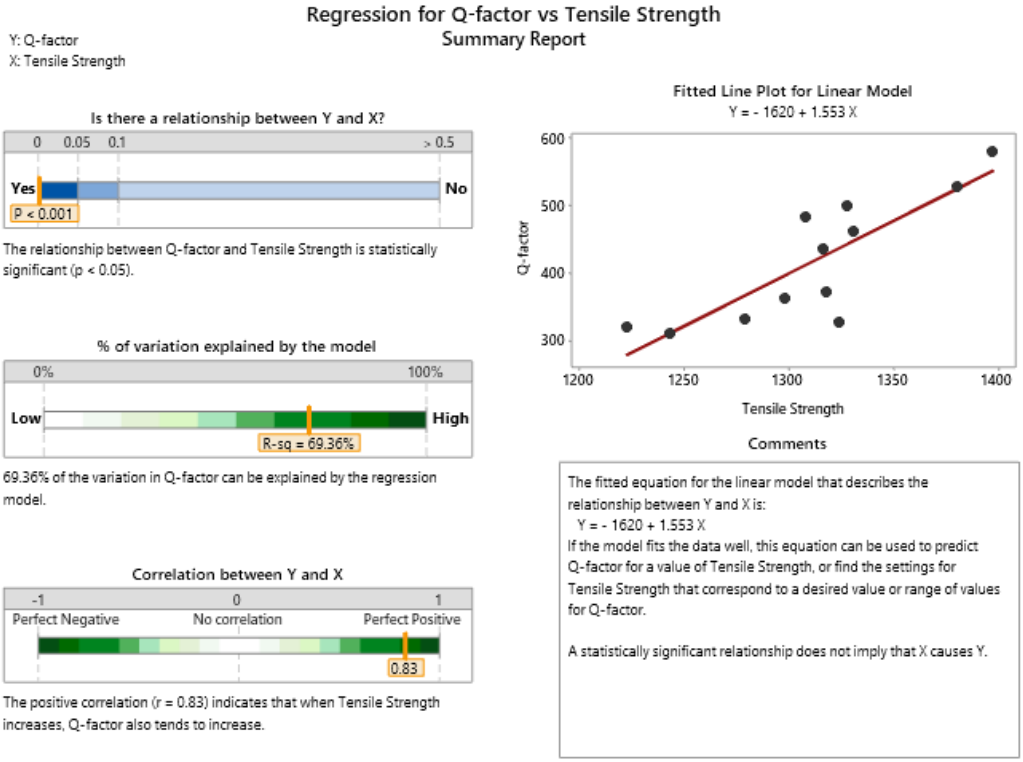

Figure 90. Minitab Output Table of Regression for Q-factor vs. Tensile Strength

Thanks to Table 29, it can be said that Q-factor values of each of the materials are interconnected to tensile strength and hardness values. From this point on, the reason behind $Q_1 > Q_4 > Q_2 > Q_3$ can be explained through precipitation strengthening mechanism. According to Blanter *et al*. 2007 [34], Fe-Ni superalloys have relaxation mechanisms and the more relaxation mechanisms there are, the higher the damping, internal friction and the lower the Q-factor. Relaxation mechanisms of Fe-Ni superalloys are the Snock type point defect, Zener type point defect, intrinsic dislocation, dislocation-impurity, grain boundary, impurity grain boundary, twin boundary and phase transformation relaxation. In this study, grain boundary, phase transformation and twin boundary relaxation mechanisms are major mechanisms for Ni-Span C902, 42NiCrTiAl, 44NiCrTiAl and 36NiCrTiAl. Ni-Span C902 and 36NiCrTiAl alloys have approximately 12% chromium, others

have approximately 5%. Higher chromium content tends to form more carbide particles and solution treatment process dissolves these phases and during cooling and subsequent aging treatment distributes finer carbide particles around γ matrix. These carbide particles block dislocation motion and decreases the mean length of dislocation. Ni-Span C902 has much smaller grains and annealing twins as it can be seen from microstructures in Figure 42, Figure 58 and Figure 70. Annealing twins shows coherency and vibration move with less damping. Small grain size blocks dislocations increase hardness. Although dislocation density may increase, mean length of dislocation was decreased which yield high Q-factor values. The production method for 44NiCrTiAl is casting. So, Snock or Zener type relaxation mechanisms are present in the matrix and there are some porosities around γ′ (Ni_3Ti) of 44NiCrTiAl as it can be seen from below Figure 91. These porosities act as dampers and decreases the Q-factor of 44NiCrTiAl.

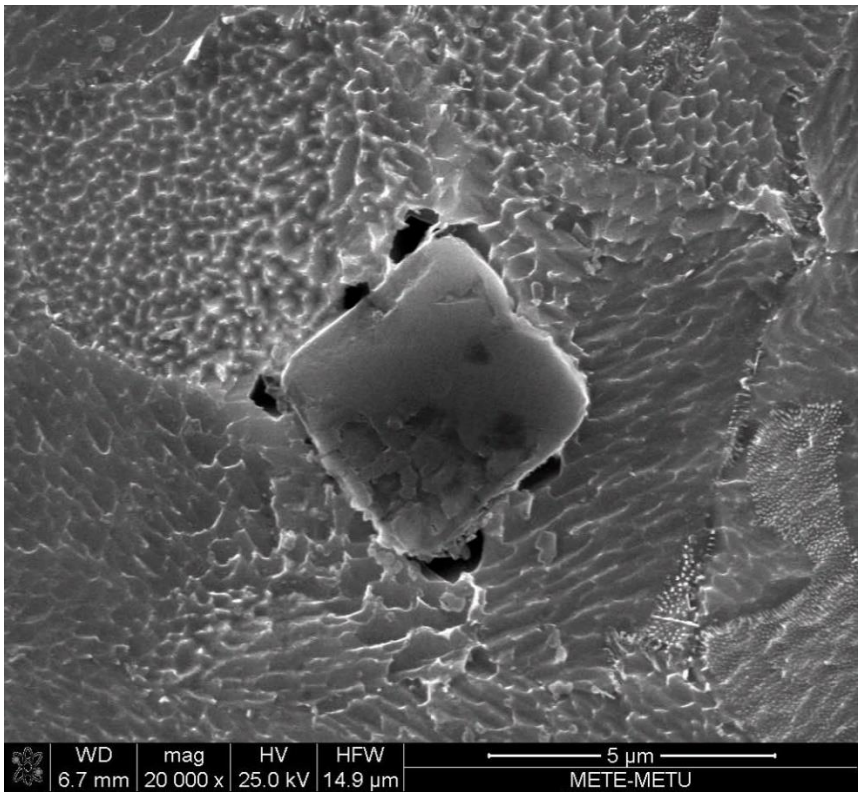

Figure 91. SEM Image Around γ′ Particle for 44NiCrTiAl

CHAPTER 5

CONCLUSIONS

In this thesis study, effect of heat treatment parameters on the Q-factor of Fe-Ni superalloys were investigated with regards to Ni-Span C902, 42NiCrTiAl, 44NiCrTiAl and 36NiCrTiAl. Following conclusions can be drawn from this study:

1. Seven different heat treatment procedures (A,A+,Q,Q+,M,M+ and S) were carried out to all four of the materials Ni-Span C902, 42NiCrTiAl, 44NiCrTiAl and 36NiCrTiAl and two of them (A+ and M+) having the highest hardness values were chosen for Q-factor tests along with as received condition materials.
2. Grain size and hardness values of 28 samples were examined (seven different heat treatment procedure and four different materials). Results showed that there is no exact relationship between grain size and hardness because primary strengthening mechanism was found to be precipitation strengthening with carbide particles.
3. A+ heat treatment procedure (30 seconds at 970°C, water quenched, 2 hours at 650°C and air cooled) yields the highest amount of Q-factor test results. When statistically analyzed, it was seen that tensile strength and hardness have statistically significant relationship between Q-factor. Ni-Span C902 and 36NiCrTiAl have more carbide particles than 42NiCrTiAl and 44NiCrTiAl. Carbide particles decreases the mean length of dislocation which resulted in the highest Q-factor of Ni-Span C902 and 36NiCrTiAl. Vacancies around secondary phases acts as relaxation mechanism and decreases the Q-factor.

REFERENCES

[1] C. C., "Nickel-Chromium Steel Forgings," *Nature,* vol. 104, no. 2619, pp. 480-481, 1920.

[2] W. Hermann and H. Sockel, in *ASTM Special Technical Publication*, 1997, p. 143.

[3] G. V. Voort, "Vac Aero International Inc.," 3 February 2011. [Online]. Available: https://vacaero.com/information-resources/metallography-with-george-vander-voort/880-metallography-of-superalloys.html. [Accessed 25 April 2021].

[4] "Hemispherical Resonator Gyroscope: Time and Navigation," [Online]. Available: https://timeandnavigation.si.edu/multimedia-asset/hemispherical-resonator-gyroscope. [Accessed 28 December 2019].

[5] R. A. Oboe, "MEMS Gyroscopes for Consumers and Industrial Applications," *Microsensors,* pp. 259-262, 2011.

[6] G. Remillieux and F. Delhaye, "Sagem Coriolis Vibrating Gyros: A vision realized," *2014 DGON Inertial Sensors and Systems (ISS),* 2014.

[7] "Foucault Pendulum," Smithsonian Institution, 2021. [Online]. Available: https://www.si.edu/spotlight/foucault-pendulum. [Accessed 28 07 2021].

[8] "Foucault pendulum | Wikiwand," Wikiwand, 2021. [Online]. Available: https://www.wikiwand.com/en/Foucault_pendulum. [Accessed 28 07 2021].

[9] V. Apostolyuk, Coriolis Vibratory Gyroscopes, Cham: Springer International Publishing, 2016.

[10] R. Lifshitz and M. L. Roukes, "Thermoelastic damping in micro- and

nanomechanical systems," *Physical Review B,* vol. 61, no. 8, pp. 5600-5609, 2000.

[11] X. Hu, K. Wu, M. Zheng, W. Gan and X. Wang, "Low frequency damping capacities and mechanical properties of Mg–Si alloys," *Materials Science and Engineering,* Vols. 452-453, no. A, pp. 374-379, 2007.

[12] H. M. T. S. M. a. I. K. Watanabe, "Elastic and damping properties from room temperature to 673 K in an AZ31 magnesium alloy," *Scripta Materialia,* vol. 51, no. 4, pp. pp.291-295, 2004.

[13] T. Sarpkaya and M. Isaacson, Mechanics of wave forces on structures, New York: Van Nostrand Reinhold, 1981.

[14] J. W. Tedesco, W. G. McDougal and C. Ross, Structural dynamics, Menlo Park: Addison-Wesley, 1999.

[15] D. J. Ewins, Modal testing, Baldock, Hertfordshire, England: Research Studies Press, 2000.

[16] ASTM International, Standard Test Method for Dynamic Young's Modulus, Shear Modulus, and Poisson's Ratio by Impulse Excitation of Vibration, West Conshohocken: ASTM International, 2002.

[17] ASTM International, Standard Test Method for Measuring Vibration-Damping Properties of Materials, West Conshohocken: ASTM International, 2017.

[18] C. Gençoğlu, B. Acar and E. C. Koç, "Serbest Sınır Koşullarında Modal Test Düzeneği". Turkey Patent TR 2014 15767 Y, 25 12 2014.

[19] The Fundamentals of Modal Testing Application Notice 243-3, Agilent Technologies, 2000.

[20] A. Nashif, D. Jones and J. Henderson, Vibration damping, New York, N.Y.:

Wiley, 1985.

[21] C. W. D. Silva, Vibration damping, control, and design, Boca Raton: Taylor & Francis, 2007.

[22] C. M. Harris and A. G. Piersol, Harris' shock and vibration handbook, New York: McGraw-Hill, 2002.

[23] M. Lalanne, Mechanical vibrations for engineers, Chichester [West Sussex]: J. Wiley, 1984.

[24] S. Garvey, "THE RELATIONSHIP BETWEEN THE REAL AND IMAGINARY PARTS OF COMPLEX MODES," *Journal of Sound and Vibration*, vol. 212, no. 1, pp. 75-83, 1998.

[25] B. J. Schwarz and M. H. Richardson, "Experimental Modal Analysis," in *in proceedings of CSI Reliability Week*, Florida, 1999.

[26] C. Gençoğlu, A. A. Gürel and E. C. Koç, "Utilization of Modal Test Techniques For Quality Control of Mass Manufactured Parts," in *ASME International Mechanical Engineering Congress and Exposition*, Phoenix, Arizona, USA, 2016.

[27] M. Lalanne, P. Berthier, J. D. Hagopian and F. C. Nelson, Mechanical vibrations for engineers, Chichester [West Sussex]: J. Wiley, 1984.

[28] B. Chouvion, "Vibration Transmission and Support Loss in MEMS Sensors," University of Nottingham, 2010. [Online]. Available: https://tel.archives-ouvertes.fr/tel-00938163/document. [Accessed 29 October 2021].

[29] V. Krasnykh, A. Zhdanova and T. Garanzha, "Precision alloys with specified elasticity," *Steel in Translation*, vol. 45, no. 7, pp. 526-533, 2015.

[30] B. H. L. a. X. H. Geddes, Superalloys: alloying and performance., Asm

International, 2010, pp. 9-14.

[31] J. R. Davis, ASM specialty handbook: heat-resistant materials, Asm International, 1997.

[32] M. J. Donachie and S. J. Donachie, Superalloys, Materials Park, OH: ASM Internat., 2002.

[33] W. Betteridge, "Iron, Nickel and Cobalt Based Superalloys and Heat Resistant Alloys," *Materials Science and Technology,* pp. 643-691, 2006.

[34] M. S. Blanter, I. S. Golovin, H. Neuhauser and H. -R. Sinning, Internal Friction in Metallic Materials, Heidelberg: Springer, 2007.

[35] J. L. Snoek, "Effect of small quantities of carbon and nitrogen on the elastic and plastic properties of Iron," *Physica,* vol. 8, no. 7, pp. 711-733, 1941.

[36] C. Zener, "Internal friction in solids," *Proceedings of the Physical Society,* vol. 52, no. 1, pp. 152-166, 1940.

[37] C. Zener, "Stress induced preferential orientation of pairs of solute atoms in metallic solid solution," *Physical Review,* vol. 71, no. 1, pp. 34-38, 1947.

[38] D. Hull and D. J. Bacon, Introduction to dislocations, Oxford: Pergamon Press, 1984.

[39] J. P. Hirth and J. Lothe, Theory of dislocations by John Price Hirth and Jens Lothe, New York: McGraw-Hill, 1967.

[40] G. Gremaud, "The hysteretic damping mechanisms related to dislocation motion," *Le Journal de Physique Colloques,* vol. 48, no. C8, 1987.

[41] V. I. Alshits and V. L. Indenbom, Dislocations in Solids, vol. 7, Amsterdam: North Holland, 1986, pp. 43-111.

[42] A. Granato and K. Lucke, "Theory of Mechanical Damping Due to Dislocations," *Journal of Applied Physics,* vol. 27, no. 6, pp. 583-593, 1956.

[43] A. H. Barnes and C. Zener, "Internal friction at high temperatures," *Physical Review,* vol. 58, no. 1, p. 87, 1940.

[44] A. S. Nowick and B. S. Berry, Anelastic relaxation in crystalline solids, New York: Academic Press, 1972.

[45] "SPECTROMAXx Metal Analyzer | SPECTRO Analytical," SPECTRO, [Online]. Available: https://www.spectro.com/products/optical-emission-spectroscopy/spectromaxx-metal-analyzer. [Accessed 28 11 2021].

[46] "Microscope.huvitz.com," Huvitz, [Online]. Available: http://microscope.huvitz.com/eng/digital/HDS-5800.html. [Accessed 2 12 2021].

[47] G. F. Vander Voort, "Metallography and Microstructures of Stainless Steels and Maraging Steels," in *ASM Handbook Volume 9: Metallography and microstructures*, Materials Park, OH, ASM International, 2004, pp. 670-700.

[48] K. B. Small, D. A. Englehart and T. A. Christman, "Guide to Etching Specialty Alloys," in *Advanced Materials & Processes*, Materials Park, OH, ASM International, 2008, pp. 32-37.

[49] "Test methods for determining average grain size," *ASTM E112-13,* vol. 03.01, p. 28, 2021.

[50] "EN ISO 6507-2:2018 Metallic Materials," *Vickers hardness test Verification and calibration of testing machines,* p. 26, 2018.

[51] "DuraScan G5," Emcotest, [Online]. Available: https://www.emcotest.com/en/products-services/hardness-testing-machines/durascan-g5/durascan-70-g5-1380/. [Accessed 2 12 2021].

[52] A. International, "ASTM E8-Standard Test Methods for Tension Testing of Metallic Materials," *ASTM,* vol. 13a, pp. 1-27, 2009.

[53] "Directindustry.com," [Online]. Available: https://www.directindustry.com/prod/instron/product-18463-1662493.html. [Accessed 30 11 2021].

[54] "Nabertherm Laboratory Furnaces," Nabertherm, [Online]. Available: https://nabertherm.com/sites/default/files/2021-01/laboratory_english_0.pdf. [Accessed 2 12 2021].

[55] "Tolerances for linear and angular dimensions without individual tolerance indications," *ISO 2768-1,* 1989.

[56] M. Margoshes, "Some Properties of New or Modified Excitation Sources," in *Symposium on Spectroscopic Excitation*, USA, 1959.

[57] Y. V. Svitich, V. F. Sukhovarov and Y. M. Kochetkov, "Heat treatment and properties of Elinvar alloys," *Metallovedenie i termičeskaâ obrabotka metallov,* vol. 30, pp. 58-60, 1984.

[58] G. V. Shlyakhova, A. V. Bochkareva and M. V. Nadezhkin, "Effect of Heat Treatememt on Microstructure and Mechanical Properties of the Precipitation Hardening Elinvar Alloy," *Russian Physics Journal,* vol. 64, no. 5, pp. 838-843, 2021.

[59] S. S. Gorelik, L. M. Letyuk, A. V. Seleznev and N. G. Chomova, "Effect of heat treatment on the properties of Elinvar alloys," *Metal Science and Heat Treatment,* vol. 16, no. 11, pp. 953-955, 1974.

[60] V. S. Postnikov, "Mechanisms of internal friction in metals," *Internal Friction in Metallic Materials,* pp. 7-25, 1970.

[61] J. Ridhwan, E. Hamzah, M. Selamat, Z. Zulfattah and M. Hafidzal, "Effect of

Aging Treatment on the Microstructures and Hardness of Fe-Ni-Cr Superalloy," *International Journal of Automotive and Mechanical Engineering,* vol. 8, pp. 1430-1441, 2013.

[62] A. B. Jacuinde, L. Arias and B. Hernandez, "Kinetics of secondary carbides precipitation in a high-chromium white iron," *Journal of Materials Engineering and Performance,* vol. 12, no. 4, pp. 371-382, 2003.

[63] O. Messe and C. Rae, "Dislocation Nucleation and Interaction with Grain Boundaries in a Polycrystalline Nickel Base Superalloy," in *Superalloys 2016: Proceedings of the 13th International Symposium on Superalloys,* USA, 2016.

[64] S. Rao, Mechanical vibrations, New Jersey: Prentice Hall, 2011.

[65] K. J. Ducki, "Analysis of the Precipitation and Growth Processes of the Intermetallic Phases in an Fe-Ni Superalloy," in *Superalloys*, AvE4EvA, 2021, pp. 111-139.

[66] J. Yan, Y. Gu, F. Sun, Y. Xu and J. Lu, "Microstructural evolution and deformation behavior of a Fe-Ni base superalloy during aging," *Journal of Alloys and Compounds,* vol. 694, pp. 739-744, 2017.

[67] V. F. Sukhovarov, Y. V. Svitich, Y. M. Kochetkov, L. M. Verner and G. G. Lyubochko, "Ultrafine grain in Elinvar alloys," *Metal Science and Heat Treatment,* vol. 26, no. 6, pp. 456-459, 1984.

[68] M. Kikuchi, "Mechanism For Nucleation of Grain Boundary Voids In A Nickel Base Superalloy," *Scripta Materialia,* vol. 19, no. No.1, pp. 14-21, 1985.